Inorganic Chemistry and Catalysis
Debye Institute for Nanomaterials
Utrecht University

Developing Novel HTM Thin Films for Hybrid Perovskite Photovoltaics

Master Thesis Report

8th of March, 2016

Koen Bossers, BSc

Supervisors:
Iván Garcia Torregrosa, MSc
Dr. Monica Barroso Silva da Cruz

Table of Contents

Abbreviations and Symbols

AM0 & AM1.5	air mass 0 & 1.5
CB	conduction band
CV	cyclic voltammetry
ETM	electron transport material
FA	formamidinium
$FAPbI_3$	formamidinium lead triiodide
fcc	face-centered cubic
FF	fill factor
FF_0	normalized fill factor
FIB-SEM	focused ion beam – scanning electron microscopy
FTO	fluorine-doped tin oxide
HTM	hole transport material
I_{sc}	short circuit current density
MA	methylammonium
MAI	methylammonium iodide
$MAPbI_3$	methylammonium lead triiodide
MEA	monoethanolamine
PCE or η	photon-to-current efficiency
PEC	photoelectrochemistry
PL	photoluminescence
PV	photovoltaic(s)
PW	petawatt
SC	semiconductor
TAS	transient absorption spectroscopy
TCO	transparent conductive oxide
TW	terawatt
UV-Vis	ultraviolet-visible spectroscopy
VB	valence band
V_{oc}	open circuit voltage
XRD	x-ray diffraction

Abstract

With an increase of global energy consumption, utilizing sustainable energy sources such as solar energy has attracted significant research interest. Solar energy can be converted into electrical energy using photovoltaic cells. Silicon photovoltaic cells have been dominating the market. However, the production of these photovoltaic cells requires both high temperatures and high purity materials. A potentially cheaper and more efficient alternative to silicon photovoltaic cells is the thin film hybrid perovskite, $MAPbI_3$, photovoltaic cell. However, to make the $MAPbI_3$ photovoltaic cells competitive with silicon photovoltaic cells, the efficiency and long term stability have to be increased further as well as a reduction of the material costs. One approach to achieve this is to replace the expensive organic hole transport materials used in $MAPbI_3$ photovoltaic cells with transition metal oxides. Within this research, undoped and 0.1-to-10 mol% Co^{2+} doped NiO as well as undoped Co_3O_4 thin films have been prepared on both FTO and glass substrates to act as hole transport materials for $MAPbI_3$ photovoltaic cells. These metal oxide thin films were coated uniformly on FTO whereas a partial coating on glass was observed. The effect of Co^{2+} dopant was observed with an increase of the unit cell parameter of the NiO cubic crystal lattice as well as an increase in the crystallite size going from respectively 4.639 Å and 173 Å for undoped NiO to 4.668 Å and 254 Å for 10 mol% Co doped NiO. An increase on the photoluminescence quenching of $MAPbI_3$ from 14.7% for undoped NiO to 90.8% for 10 mol% Co doped NiO and 98.8% for Co_3O_4 was observed. The $MAPbI_3$ photovoltaic cells achieved low photon-to-current efficiencies of 0.25% due to rapid decomposition of $MAPbI_3$ upon sputtering of a silver cathode layer as observed with XRD.

1. Introduction

1.1 Solar Energy

It's estimated that the global energy consumption per year will increase towards roughly 25 TW in 2035 and 30 TW in 2050 compared to 17 TW in 2007 [1], [2]. In comparison the amount of solar energy in the form of photons reaching the earth per second is about 180 PW (=180.000 TW). About 36 PW of this solar energy can be converted into different types of energy such as electrical, chemical and thermal energy at the earths land mass [3], [4]. However harvesting solar energy is not as simple as it seems. For instance, at peak hours roughly 1 kW/m^2 is available. With current technology, non-concentrated photovoltaic cell efficiencies lie between 10-20% for commercial modules. Roughly 10.000 m^2 and billions of dollars will be needed to construct a single gigawatt producing, photovoltaic cell facility [3]. Still with the sun being earths most abundant energy source a lot of ongoing research is performed to optimize solar cell efficiencies, reduce production costs and increase stability to replace at least a part of the conventional non-sustainable energy sources with this abundant, sustainable energy source [3], [5].

The energy emitted by the sun comes in the form of photons with a discrete energy distribution. This distribution of photons with a specified energy that reach the earth is called the power density solar spectrum. In figure 1 this power density solar spectrum is shown for air mass values of 0 and 1.5 corresponding to the power density solar spectrum in vacuum and at earths land mass, respectively. A significant portion of the power density lies in the visible light range between 380 and 780 nm [4].

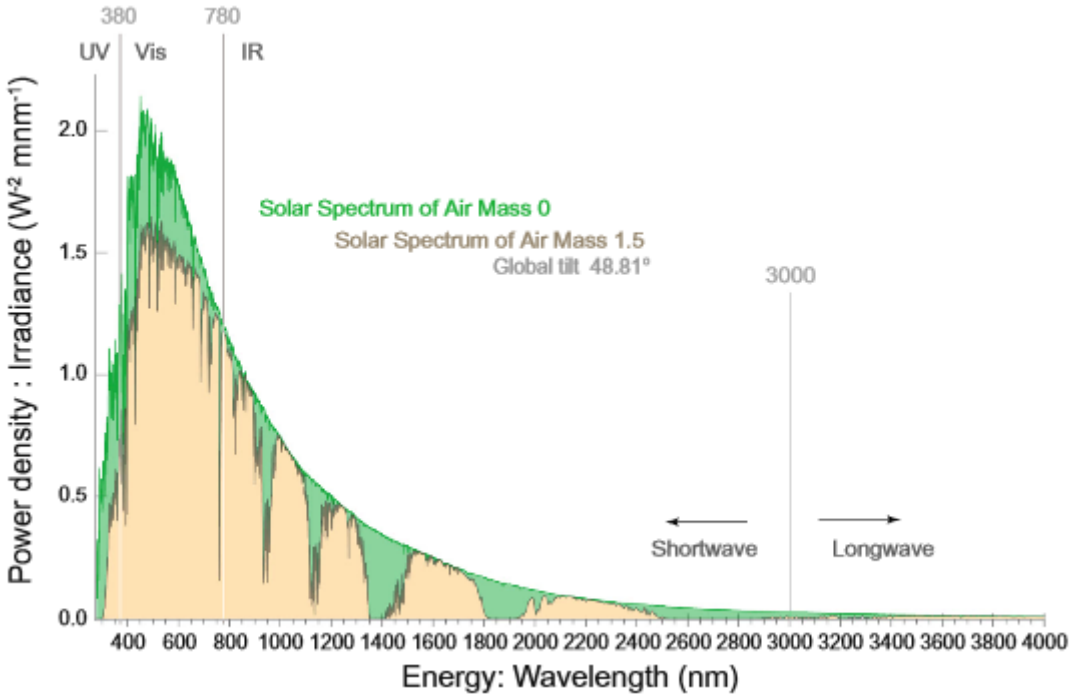

Figure 1 Solar energy spectrum at air mass 0 and 1.5. This spectrum shows the power density distribution of wavelengths emitted by the sun between the UV-Vis-IR region at different air mass values [4].

1.2 Converting Solar Energy with Photovoltaic Cells

By using a photovoltaic (PV), the solar energy can be converted into electrical energy. These PV cells are based on semiconductors (SC) that absorb photons with energy larger than the band gap of the material. About 90% of the PV market is covered by crystalline silicon PV, where silicon has a band gap close to 1.1 eV at room temperature. These PV consist of either monocrystalline or polycrystalline silicon which have an average photon-to-current efficiency (PCE) of 18.5% and 16.5% for large area, commercialized PV, respectively [6]. Monocrystalline silicon PV is more efficient than the polycrystalline PV but also more expensive to produce. Both of these PV technologies use thick silicon layers of typically a few hundred μm. Thin film PV technology is rapidly emerging as a cheaper alternative since the thin films are typically about a few tens to a few hundred nm thick, thus significantly reducing material costs [4], [7]. Examples of commercially available thin film PV are amorphous silicon, CdTe and CIGS [6], [7] (typically copper indium gallium selenide). These thin film PV have a low market share mostly due to the low PCE achieved so far [6]. Recently, hybrid perovskites have emerged as candidates for thin film PV achieving PCE values up to 20.1% for small area cells [8]–[10]. Whereas silicon is an indirect band gap material, hybrid perovskites have a direct band gap [8], [9]. This feature allows the use of thin films of hybrid perovskites. The typical band gap of ~1.55 eV of iodide based hybrid perovskites allows these materials to reach a theoretical maximum PCE value of 31%, which is close to the Schockley-Queisser limit of 33% for a single junction PV [11]. The low temperature deposition method to produce hybrid perovskite thin films as well as the inexpensive starting materials, typically PbI_2 and CH_3NH_3I, further add to the rivalry with silicon PV [8], [9], [12]–[14]. However, fabrication of highly efficient large scale PV as well as long term stability has prevented the commercialization of hybrid perovskite PV technology to date.

1.3 The Working Principles of a Photovoltaic Cell

In this section a compact description of semiconductor physics and the photovoltaic effect is provided with respect to p-i-n thin film technology. This section is largely based on the book of "The Physics of Solar Cells", edition 2003, by Jenny Nelson [5] complemented by other literature which will be specifically referred to.

1.3.1 Semiconductor Physics

At 0 K the VB of any undoped SC is filled with bound electrons and the CB is completely empty of charge carriers. The VB and CB are separated by a band gap which is devoid of electronic states. With the input of energy, an electron can be excited from the full VB to the empty CB leaving behind a positively charged hole in the VB. Initially the hole in the VB and electron in the CB remain in close proximity of each other due to Coulombic interactions and are called an exciton. The input of energy is either an absorbed photon when the photon energy is equal to or larger than the band gap, as seen in figure 2 or thermal energy at T > 0 K. The smaller the band gap of a SC, the more electrons are thermally excited to the CB at a certain temperature. For any intrinsic SC such as pure silicon, the number of thermally excited free charge carriers at room temperature, called the intrinsic carrier concentration, n_i, is on the order of 10^{10} cm^{-3}. For comparison, 10^{21} atoms occupy the crystal lattice of silicon. Thus only a tiny fraction of electrons is excited due to thermal energy [15]. The binding energy of the exciton quasi-particle determines how easily the exciton can disassociate into the free charge carriers. For inorganic SC this value is often around the thermal energy, k_bT, and thus room temperature is sufficient to separate the exciton into free charge carriers, whereas for organic SC such as polymers these values are often significantly higher than k_bT, up to values of 0.5 eV (k_bT ~ 0.024 eV at 300 K) and electric-field generating junctions are needed to separate the exciton [16].

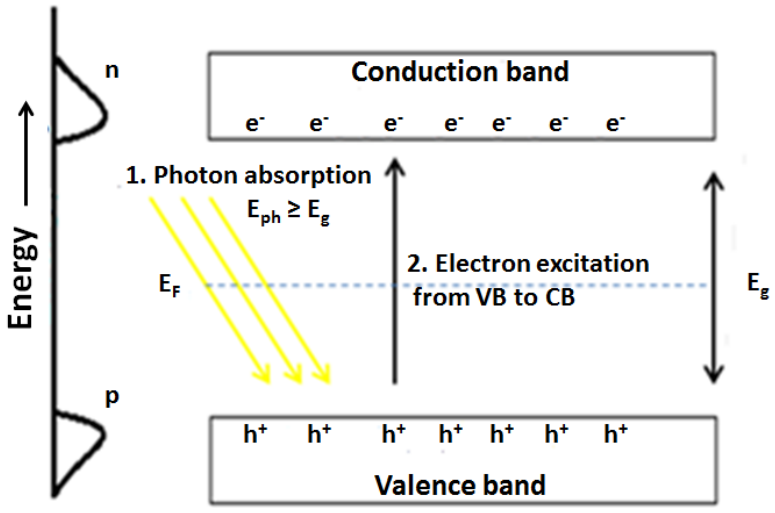

Figure 2 SC band diagram. Photons with an energy larger than the band gap, E_g, can excite an electron from the VB to the CB creating the hole and electron charge carrier species. The Fermi level E_F is positioned in the middle of the band and corresponds to the energy at which states are occupied.

Much higher values of free charge carrier concentrations can be obtained by doping an intrinsic SC with different elements, called the dopants. If the dopant has less valence electrons than the host SC it can accept an electron, leaving a hole behind in the VB of the host SC. Conversely, a dopant with more valence electrons can donate an electron in the CB. These dopants are called acceptors and donors. The effect of doping on the band diagram of the host SC is shown in figure 3. Examples of acceptor and donor elements for tetravalent silicon are, respectively, trivalent boron and pentavalent phosphorus. In the case of an acceptor the term p-type doping is used, since the host SC contains more positive than negative free charge carriers. When the dopant is a donor, the term n-type doping is used, since more negative charge carriers are present in the SC compared to positive charge carriers. The majority charge carriers in a n-type doped SC are therefore electrons and the minority charge carriers are the holes. The opposite is the case for a p-type doped SC. The number of free charge carriers in a doped SC ranges from around 10^{16} to $10^{19\text{-}20}$ cm^{-3} for light to heavy doping.

Doping has important effects on the properties of the host SC. Doping increases conductivity according to equation 1 where q is the elementary charge, $\mu_{n,p}$ the electron and hole mobility and n, p are the electron and hole concentrations respectively. However, doping also induces crystal defects and lattice strain. The crystal defects can act as trap sites and recombination centers for free charge carriers. Furthermore, doping leads to a shift of the Fermi energy level closer towards the doped band which is of importance for the formation of junctions. Very heavy doping can lead to semiconductors behaving like metals in terms of conductivity. A specific class of these materials is the transparent conductive oxide (TCO) which is a wide band gap (>3 eV) SC with metal-like conductivity, thus combining high optical transmission with high conductivity.

$$\sigma = q\mu_n n + q\mu_p p \tag{1}$$

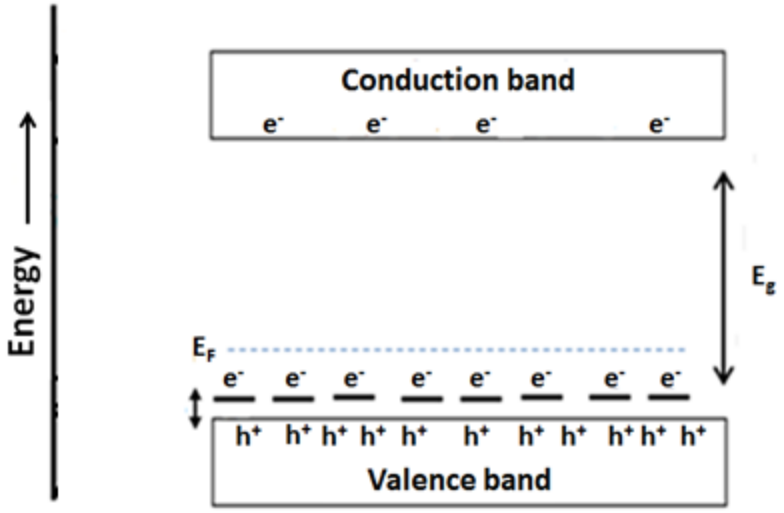

Figure 3 Effect of p-type doping on a SC. The acceptor dopant effectively injects a hole into the VB of the SC. The number of holes in the VB is now larger than the number of electrons in the CB thereby making the material p-type. The Fermi level is effectively shifted towards the VB.

1.3.2 Semiconductor and Metal Junctions

For SC and metals the work function, Φ_x, is defined as the energy difference between the energy of a free electron in vacuum, E_{vac}, and the Fermi energy level, E_F. The Fermi energy level as already seen in figures 2 and 3 is defined as the energy up to which states are occupied. It lies in the middle of the band gap for an intrinsic SC because the number of states occupied in the CB equals the number of states unoccupied in the VB. For a p-type material it lies closer to the VB whereas for a n-type material it lies closer to the CB. When oppositely doped SC layers or SC and metal layers are interfaced with each other and have different work functions they will form a junction. The junction is the result of the different Fermi energy levels lining up to each other in thermal equilibrium and is caused by diffusion of free charge carriers towards the interface where they recombine with their oppositely charged equivalent. This diffusion of free charge carriers leaves oppositely charged immobile species behind in the doped SC layers near the layer interfaces. The space-charge region is formed at the interface of these layers due to these immobile charge species present. This net charge creates an electric field in this region called the build-in potential, qV_B. These build-in potentials will direct oppositely charged carriers into different directions and are therefore crucial to separate the photogenerated electrons and holes at SC-SC or SC-metal interfaces.

SC-metal junctions are either rectifying (Schottky-barrier), in which the flow of majority carriers across the junction is prohibited at zero or low positive bias voltage, or non-rectifying (ohmic contact) in which the majority carriers can travel freely across the interface under a very low resistive contact. In PV cells the rectifying SC-metal junction is similar to SC-SC junctions but generates a weaker qV_B and is thus unwanted in modern PV designs. In figure 4, the band diagram of the non-rectifying junction is shown for a p-type SC and a metal. Whether the rectifying or non-rectifying contact is made, depends on the work function difference, $\Phi M - \Phi_{SC}$. In PV devices ohmic contacts are required at both terminal for charge carrier collection. At least one of the two ohmic contacts is a TCO such as F:SnO_2 or In_2O_3/SnO_2 because a (semi-)transparent window is necessary for the photons to reach the active SC layer.

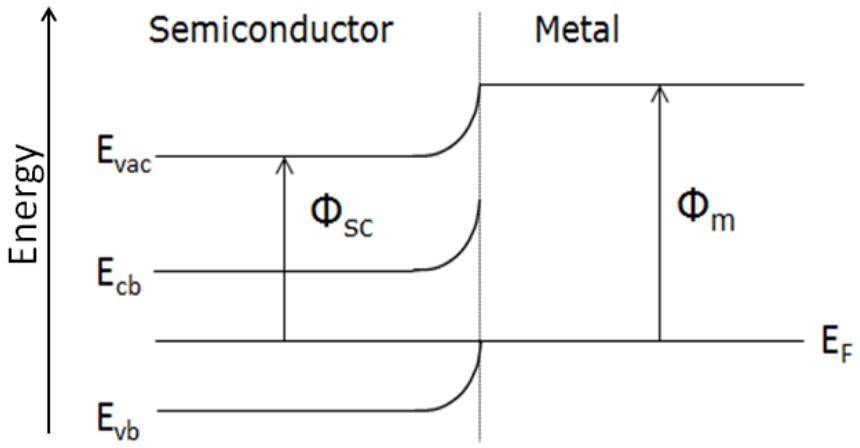

Figure 4 Band diagrams of a p-type SC – Metal interface forming an ohmic contact. The ohmic contact allows the holes from the SC to flow into the metal under very low resistive conditions whereas the electrons in the CB are prohibited from crossing the interface.

For SC-SC interfaces multiple junctions are possible, such as p-n, p-i-n, bulk heterojunction, bilayer, heterojunctions, and the already discussed ohmic contact. In this research the thin film p-i-n junction is utilized and therefore will be explained.

In the p-i-n junction a thin intrinsic SC film is sandwiched between both p- and n-type doped thin SC films. The intrinsic SC film is responsible for the generation of free charge carriers upon photon absorption. The p-and-n-type doped layers are therefore often considerably thinner to minimize photon absorption events from these layers. The build-in potential field extends through the entire intrinsic SC layer and allows for efficient free charge carrier separation since the oppositely charged free carriers are directed towards the p- and n-type doped SC interfaces. The holes can then be injected into the p-type layer where they become the majority carriers and the opposite holds true for the electrons. In figure 5 the p-i-n junction is shown. These photogenerated charge carriers are transported through the doped SC layers towards the ohmic contacts.

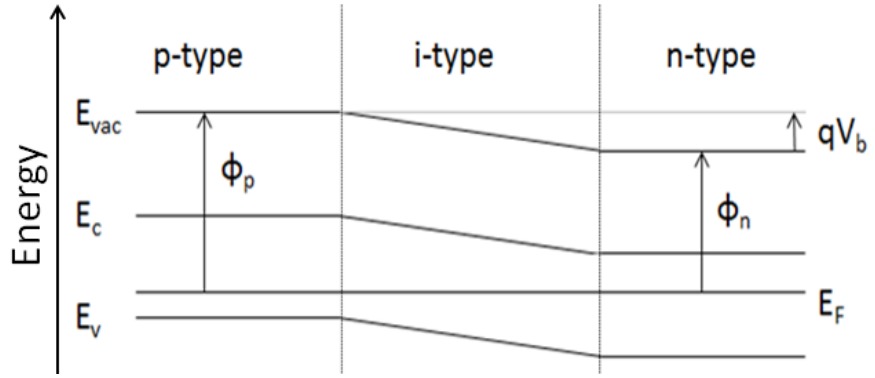

Figure 5 Band diagram of the thin film p-i-n junction. The build-in potential, qV_b , extends through the entire intrinsic layer as visualized by the gradient of the bands when it becomes interfaced with the p- and n-type layers.

An important quantity for SC materials is the free charge carrier diffusion length, L_n for electrons and L_p for holes. It is defined as the average distance the respective free charge carrier can travel through a specified SC material before it recombines with an oppositely charged carrier, be it mobile or immobile species. Equation 2 shows the diffusion length $L_{n/p}$, the charge carrier life time $\tau_{n/p}$ and the diffusion coefficient $D_{n/p.}$ The electron and hole diffusion lengths do not necessarily have the same value within the same layer, even for intrinsic layers. The build-in potential field and the diffusion length determine the maximum thickness the intrinsic SC layer should have in a p-i-n junction. For effective free charge carrier separation the qV_B should extent through the entire intrinsic SC layer. Furthermore, the diffusion length should exceed the layer thickness so that recombination effects within the intrinsic SC are minimized. For the intrinsic SC in the thin film p-i-n junction the diffusion lengths have to be on the order of a few hundred nm to a µm whereas for thick film p-n junctions higher values are necessary. In the case of doped monocrystalline silicon, for p-n junctions, values up to ~500 µm have been reported whereas for the hybrid perovskite $MAPbI_3$, which acts as the intrinsic SC in a p-i-n junction, L_n and L_p are on the order of 1 µm [17], [18].

$$L_n = \sqrt{\tau_n D_n}, \quad Lp = \sqrt{\tau_n D_n} \tag{2}$$

1.3.3 Photocurrent, Voltage and the Power Conversion Efficiency

The relevant semiconductor physics for the p-i-n junction and p-i-n junction based PV have been discussed in section 1.3.1 and 1.3.2. However, to better understand the working principles of a PV cell, the current density, voltage and power conversion efficiency characteristics are briefly discussed.

First the p-i-n junction PV cell under illumination and without an applied bias voltage will be discussed. The photogenerated charge carriers in the intrinsic layer will be directed towards the p- or n-type layer and become separated due to selective injection. These charge carriers travel through the doped layers towards the ohmic contacts where they are extracted into the external electrical circuit. This current density at zero bias voltage under illumination is the short-circuit current density, J_{sc}, with conventional units of either A/m^2 or mA/cm^2. This short circuit current density is the same as the photogenerated current density, J_{ph}, under normal conditions because without an applied bias voltage there is no so called dark current density, J_{dark}. The short-circuit current density is the maximum current density a PV device can generate because the total current density $J(V)$ is the sum of J_{ph} and J_{dark} as shown in equation 3 where J_{dark} is opposite in sign of J_{ph} and equals zero at zero bias voltage.

$$J(V) = J_{ph} - J_{dark}(V) \tag{3a}$$

$$J_{dark}(V) = J_0\left(e^{\frac{qV}{nk_bT}} - 1\right) \tag{3b}$$

However PV devices cannot perform electrical work at zero voltage as electrical work or power density is the product of current density and voltage. Therefore one has to consider the effects of operating under a forward bias voltage. A forward bias voltage means the p-type side is connected to the positive terminal and the n-type side to the negative terminal. This forward bias directs the dark current density towards the intrinsic layer and thus in opposite direction of the photocurrent density. However the build-in potential spanning the entire intrinsic region is opposite of sign to the forward bias voltage. This means that especially at low forward bias voltage the dark current density cannot travel across the p-i-n junction due to an energy barrier. Therefore at low forward bias voltage the dark current density is very small for ideal p-i-n junctions. However as the dark current charge carriers keep flooding towards the intrinsic layer, the space-charge region becomes smaller due to increased recombination of the immobile charged species with the oppositely charged dark current charge carriers. This leads to a decrease in the potential energy barrier. Therefore the dark current density increases at higher forward biases and the total current density decreases in value. At some point J_{ph} equals J_{dark} and the total current density equals zero. This point is called the open-circuit voltage, V_{oc}.

If the PV device would behave like an ideal diode without illumination, then J_{dark} would be close to zero until V_{oc} is reached. At this point the applied forward bias overcomes the build-in potential and majority carriers are free to flow across the junction. However even for ideal diodes J_{dark} will be slightly larger than zero under forward bias meaning that at any operating voltage the total current density is less than J_{ph} . The consequence of this is that the maximum power density of the device, P_{max}, which is the operating power of a PV cell, occurs at $J_{max} < J_{sc}$ and $V_{max} < V_{oc}$. The fill factor, FF, from equation 4a probes how "square" the J-V curve behaves from figure 6 between the points of J_{sc} and $V_{oc.}$ Note that even in the ideal case, $0 < FF < 1$ due to J_{dark}. The normalized fill factor, FF_0, describes the maximum value a PV cell can reach and is shown in equation 4b where v_{oc} is the normalized V_{oc} from equation 4c. V_{oc} is normalized over the Boltzmann constant, k_b, the temperature, T, the elementary charge, q, and an ideality factor which is 1 for ideal-behaving PV cells or a higher integer number for poor cells. For a PV cell such as monocrystalline silicon or the hybrid perovskite $MAPbI_3$ with a V_{oc} of ~1 V the FF_0 value is 0.88 (88%). PV devices with a V_{oc} of 1 V but $FF < FF_0$ suffer from series and/or parallel resistance within the cell and are thus subject to further optimization allthough reaching FF_0 is not easily achieved especially for polycrystalline materials that possess many crystal boundaries which are defect rich at the interface and thus offer a great density of trap and recombination sites.

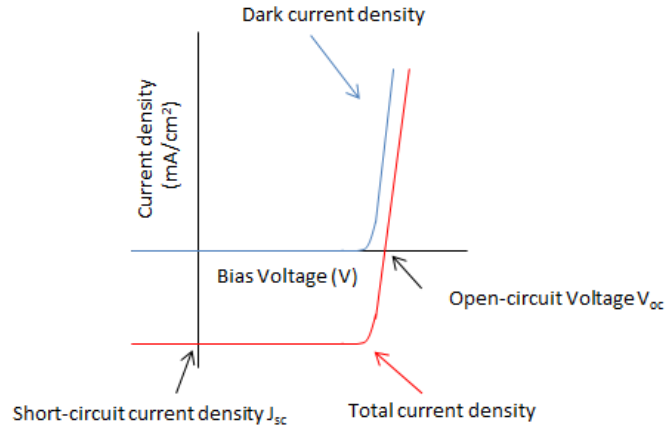

Figure 6 Example of an ideal J-V curve with the total current density in red and the dark current density in blue. The "square-like" behaviour of the total current density is characteristic of a high FF value.

$$FF = \frac{P_{max}}{J_{sc}\,x\,V_{oc}} = \frac{J_{max}\,x\,V_{max}}{J_{sc}\,x\,V_{oc}} \quad (4a)$$

$$FF_0 = \frac{v_{oc} - \ln(v_{oc} + 0.72)}{v_{oc} + 1} \quad (4b)$$

$$v_{oc} = \frac{q}{nk_bT} V_{oc} \quad (4c)$$

The efficiency of photon-to-current efficiency, PCE or η, can now be defined as the power extracted from the system in the form of electricity, P_{max}, divided by the power supplied to the system in the form of photons, P_{in}. Using equation 5 one can describe the efficiency in terms of J_{sc}, V_{oc} and FF which can easily be deduced from J-V curves such as the one in figure 6 above obtained from cyclic voltammetry.

$$\eta = \frac{P_{max}}{P_{in}} = \frac{J_{max}\,x\,V_{max}}{P_{in}} = \frac{J_{sc}\,x\,V_{oc}\,x\,FF}{P_{in}} \quad (5)$$

The PCE dependence of the incoming photon energy provides valuable information on the PV cells performance. Internal photon-to-current efficiency (IPCE), also known as internal quantum efficiency (IQE), and external photon-to-current efficiency (EPCE), also known as external quantum efficiency (EQE), from equations 6a and 6b can provide this information. EPCE tells us how many of all the incoming photons of a particular energy are converted into extracted current density whereas IPCE only takes into account the conversion of actual absorbed photons of a particular energy into current density. PV devices with low EPCE values might need thicker layers for instance so that more photons ($>E_g$) will be absorbed whereas devices with low IPCE values most likely suffer from severe recombination effects and thus resistance values.

$$IPCE = \frac{electrons/s}{photons/s} \tag{6a}$$

$$EPCE = \frac{electrons/s}{absorbed\ photons/s} \tag{6b}$$

1.4 The Perovskite Family

Perovskites are materials with the same crystal structure and general formula as the original perovskite, $CaTiO_3$. The general formula ABX_3 consists of a large cation A, in a 12-coordinated cuboctahedral position (AX_{12}), a smaller B cation that is in a 6-coordinated octahedral position (BX_6), and the X anion, which is also 6-coordinated. In figure 7 the octahedral BX_6 and cuboctahedral AX_{12} unit cells are sketched [8], [9], [19].

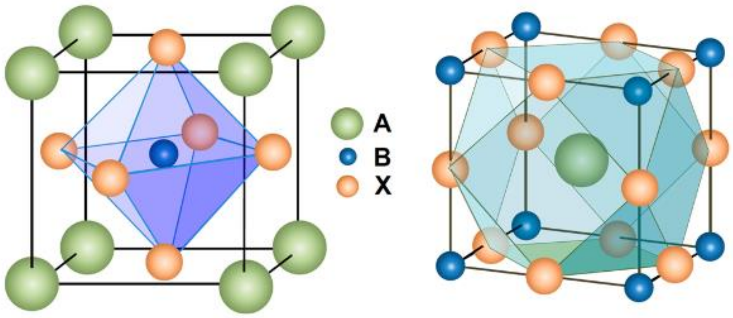

Figure 7 General Perovskite ABX_3 crystal structure. Left**)** Octahedral configuration of small cation B. Right**)** Cuboctahedral configuration of large cation A [8].

An ideal perovskite has the cubic structure, however, for most perovskites, either pseudo-cubic or distorted cubic structures can also be observed, due to BX_6 tetragonal distortions, as well as tetragonal and orthorhombic phases [19]. For the formation of perovskites, the Goldschmidt tolerance factor (*t*) is often considered [8]. This factor, as shown in equation 7a, describes the ratio of crystal radii of A, B and X respectively r_a, r_b and r_x. Perovskites are arguably stable when *t* is in the range of 0.813 to 1.107. However this tolerance factor isn't always correct in predicting stability and therefore a second factor, the octahedral ratio (μ) is used based on equation 7b which describes the ratio of the crystal radii of the small cation b, r_b and the anion x, r_x. *t*-μ mapping shows that possible perovskite structures should additionally to the *t* values fall within a μ range of 0.442-0.895. However, even the combination of these two rules still has exceptions [8].

$$t = \frac{r_a + r_x}{r_b + r_x} \frac{1}{\sqrt{2}} \tag{7a}$$

$$\mu = \frac{r_b}{r_x} \tag{7b}$$

The most common perovskites have divalent oxygen as the anion, a divalent alkaline or rare-earth metal as the larger cation and tetravalent transition metals as the smaller cation. However, hybrid organic-inorganic perovskite formation is also possible. These hybrid organic-inorganic perovskites, simply called hybrid perovskites, have both an organic and inorganic cation and a halide anion. The larger cation is monovalent and organic and the smaller, inorganic cation is divalent. These hybrid perovskites have proofed to possess impressive optoeletric properties [8], [9], [19] making them interesting for photovoltaic cells. Some examples of the cations and anions found in hybrid perovskites are the organic $CH_3NH_3^+$ (MA) and $[CH_3(NH_2)_2]^+$ (FA) species, post-transition metal cations Pb^{2+} and Sn^{2+} and the halide anions Cl^-, Br^- and I^- [8], [9], [19]. The hybrid perovskite of interest in this research is $MAPbI_3$ which has proved to be one of the most efficient hybrid perovskite so far [8], [9], [19].

1.4.1 The Hybrid Perovskite: $MAPbI_3$

As mentioned above, the hybrid perovskite $MAPbI_3$ is one of the most efficient hybrid perovskites reported for p-i-n junction PV cells due to the materials favorable properties for PV. One of these favorable properties is the direct band gap of $MAPbI_3$ 1.57 eV [8], [9], [19]. This direct band gap allows the utilization of $MAPbI_3$ as a thin film due to the high absorption coefficients associated with direct band gap. Theoretical analysis on the relationship between band gap and maximum achievable PCE shows the 1.57 eV band gap of $MAPbI_3$ can achieve a higher maximum efficiency than monocrystalline silicon with an indirect band gap of 1.11 eV [20]. The free charge carrier conductivity of $MAPbI_3$ exceeds that of the often used n-type TiO_2 which in turn lowers the recombination rate of the free charge carriers within the hybrid perovskite layer and therefore increase the PCE [9]. Furthermore, depending on the deposition method, free charge carrier diffusion lengths up to 1.2 µm have been reported [18]. Finally, the photogenerated particles do not exist in the form of a bound exciton at room temperature within the hybrid perovskite crystal structure but as free charge carriers which is a necessity to successfully extract the charge carriers to perform work in an external load [16].

However, there are also two major drawbacks to the utilization of this hybrid perovskite in commercial modules. The first one is the instability of $MAPbI_3$ in water and moist air. It is hypothesized that the MA cation and one iodide anion leave the perovskite structure and a PbI_2 film stays behinds [21], [22]. For the perovskite decomposition under moist air, the proposal was made that H_2O molecules are catalyzing the $MAPbI_3$ decomposition into HI, CH_3NH_2 and PbI_2 as shown in figure 8 [23]. Therefore, sufficient sealing of the hybrid perovskite layer is necessary to ensure the stability of $MAPbI_3$ based PV operating temperatures (~90 °C) to prevent H_2O diffusion.

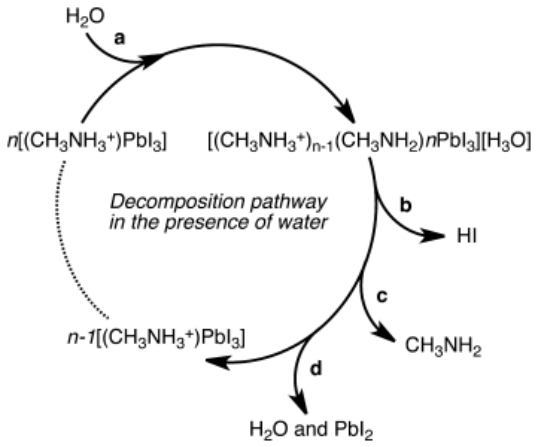

Figure 8 Proposed decomposition of $MAPbI_3$ in the presence of H_2O. A) H_2O initiates $MAPbI_3$ decomposition by complexing. B-C) HI and CH_3NH_2 are soluble in H_2O and volatile at room temperature and readily leave the crystal structure. D) H_2O leaves the crystal structure and a PbI_2 residual structure stays behind. Reproduced from Frost, *et al.* [23]

Besides the instability of MAPbI3 due to moisture, the presence of Pb^{2+} is also seen as a problem for large scale production. Pb^{2+} is very toxic for the environment, especially the aqueous. Research is being conducted to replace the Pb^{2+} cation with for instance the less toxic Sn^{2+}. However devices based on Sn^{2+} such as $MASnI_3$ perform considerably worse than the lead counterpart where highest achieved PCE lies as 4.18% for a mixed Pb/Sn hybrid perovskite [24].

1.4.2 Hybrid Perovskite PV Layout

Hybrid perovskite PV imitate the p-i-n junction. The hybrid perovskite can be thought of as the intrinsic layer which absorbs and converts photons with an energy larger than its band gap into free charge carriers that make up the photocurrent density. Within both organic PV and hybrid perovskite PV the terminology for the p-i-n junction layers is somewhat different. Instead of the p-type and n-type layer terminology, these layers are called respectively the hole transport material (HTM) and electron transport material (ETM). Within the scope of this research the definition of the HTM and ETM is the same as that of the p-type and n-type layers in the p-i-n junction.

A brief history on the development of the hybrid perovskite PV will be given here along with the different hybrid perovskite p-i-n junction layouts developed. The initial cell layout by Miyaska *et al.*, was an adaptation from the original liquid electrolyte dye-sensitized solar cell (DSSC) [25]. This layout is shown in figure 9A where the brown hybrid perovskite sensitizers are shown as the brown dots. The liquid electrolyte, I^-/I^{3-}, redox couple that fills the pores acts as the HTM. Miyaska *et al.*, were the first ones to investigate hybrid perovskite based PV and initially used the following two hybrid perovskites: $MAPbI_3$ and $MAPbBr_3$. The triiodide has a band gap of about 1.57 eV and the tribromide of 2.2 eV. These PV cells based on the hybrid perovskite sensitizers achieved PCE values of respectively 3.8% and 3.1% for the iodide and bromide variants [9], [25]. However these PV cells were highly unstable because the liquid electrolyte would quickly decompose the hybrid perovskite sensitizers. By placing a thin insulating layer of Al_2O_3 over the hybrid perovskite sensitizers the PCE increased to 6.0% and stability was improved because the electrolyte and hybrid perovskite did not come into direct contact [26].

The second layout is shown in figure 9B and is called the mesostructured hybrid perovskite PV cell. Four large differences exist between this layout and the DSSC layout. First, a solid-state HTM is used instead of the liquid-electrolyte which increases the inherent stability of the PV cell. Secondly instead of partially filling the mesoporous scaffold, it is now completely filled to increase the amount of light absorbed and thus the current density generated. The third difference is the introduction of a very thin blocking layer between the mesoporous scaffold and the ohmic contact such as fluoride doped tin oxide (FTO). This dense, nonporous blocking layer principally acts the same as either the HTM or ETM in the sense that only one of the two free charge carriers can cross the layer interface and therefore travel to the ohmic contact. This blocking layer is often only a few tens of nm thick and decreases recombination events within the PV cell and therefore increases the PCE efficiency [27]–[29]. $MAPbI_3$ PV based on this layout with TiO_2 as the mesoporous scaffold have achieved a wide range of PCE values from about 9% to 12.3% and going up to 16% [27]–[29]. PCE values of 16,1% and 15.76% have been achieved by Mahmood *et al.*, and Ko, *et al.*, using ZnO rods as the both the ETM and mesoporous scaffold material [30], [31]. The fourth difference is that the mesoporous scaffold in this layout does not have to be of a conductive nature and thus act as

the ETM or HTM which is required in the DSSC setup [32]. Due to the complete pore filling of this network, the scaffold can be an insulation material such as Al_2O_3 in which $MAPbI_3$ itself acts as the ETM layer towards the blocking layer interface. Using the insulation Al_2O_3 scaffold instead of the TiO_2 has proved to increase both stability and efficiency with a PCE value of 10.9% [32]. In both the DSSC sensitized and the mesostructured $MAPbI_3$ PV, the mesoporous scaffold is a few microns thick [9], [25]–[29], [32].

The third and fourth cell layouts from figures 9C and 9D are the most simple designs for $MAPbI_3$ and are respectively called the normal and inverted planar heterojunctions. The entire mesoporous scaffold is removed to make way for planar layers. In the normal structure the blocking layer is the ETM, mostly TiO_2, whereas in the inverted structure the blocking layer is the HTM. Whereas the $MAPbI_3$ infiltrated mesoporous scaffold in layout one and two is a few µm thick in general these planar structures have a hybrid perovskite layer thickness in the range of 100-1000 nm [33]. Even though $MAPbI_3$ have reported electron conductivities exceeding that of the mesoporous scaffold, TiO_2, there are some modifications necessary for a successful planar heterojunction. The reason is that for $MAPbI_3$ deposited from a single precursor solution the diffusing length, L_D, is on the order of 200 nm for both holes and electrons [18]. Thus for a planar hybrid perovskite layer thicker than 200 nm recombination effects become significant and hinder the cell efficiency. This is solved by improving the crystallization of the hybrid perovskite layer which can be achieved either by chloride doping to get the $MAPbI_{3-x}Cl_x$ structure where Cl is found in very low quantities or by using more controlled deposition methods such as a two-step or sequential deposition (section 2.3.2) which lead to reported L_D values up to 1200 nm [18]. The main difference between planar heterojunction layouts C and D is the order in which the p-i-n layers are deposited from a bottom-up manner. Most research has been done on the normal structure where the HTM is an expensive organic molecule or polymer such as Spiro-OMeTAD. Not only are these organic HTM's expensive, they are often also not stable due to O_2 and moisture degradation [21]. However, considering the intrinsic instability of the hybrid perovskites at high temperatures p-type metal oxides in general could not be investigated with the normal planar heterojunction. The inverse planar heterojunction therefore allowed the use of HTM layers that require high-temperature deposition methods with conventional solution processed techniques such as spin coating. For the normal planar heterojunction efficiencies of 19.3% have been reported through the interface engineering and the use of an anti-reflective coating based. For the inverted planar heterojunction values up to 15.4% have been reported with a Cu doped NiO as the HTM blocking layer [34].

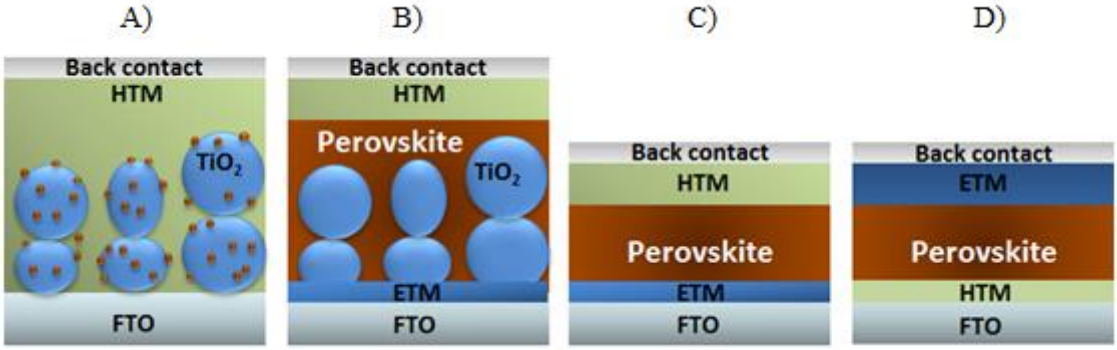

Figure 9 Four different geometries for perovskite solar cells. A) The dye sensitized setup with perovskite nanoparticles covering the porous TiO_2 surface. B) The porous metal oxide infiltrated by a perovskite layer. C-D) the normal and inverted planar heterojunction of a pure perovskite layer.

1.4.3 Band Edge Positions and Aligning

The four general layouts of hybrid perovskite PV were discussed in the previous section together with a few utilized ETM and HTM materials such as TiO_2, ZnO, Spiro-OMeTAD and NiO. However, besides the perquisite that the ETM is an n-type material and the HTM a p-type material, the alignment of the ETM/HTM VB and CB with that of the VB and CB of $MAPbI_3$ is very important. The band edges have to be positioned in such a way that it is thermodynamically favorable to inject these charges. The CB edge of the ETM has to be positioned lower than that of the CB edge of $MAPbI_3$ so that the free electron can lower its potential energy by entering the HTM CB. For a hole in the VB the opposite holds true and it is thermodynamically favorable to be transferred to a VB with a higher edge energy value. This principle of band alignment and electron/hole injection is visualized in figure 10.

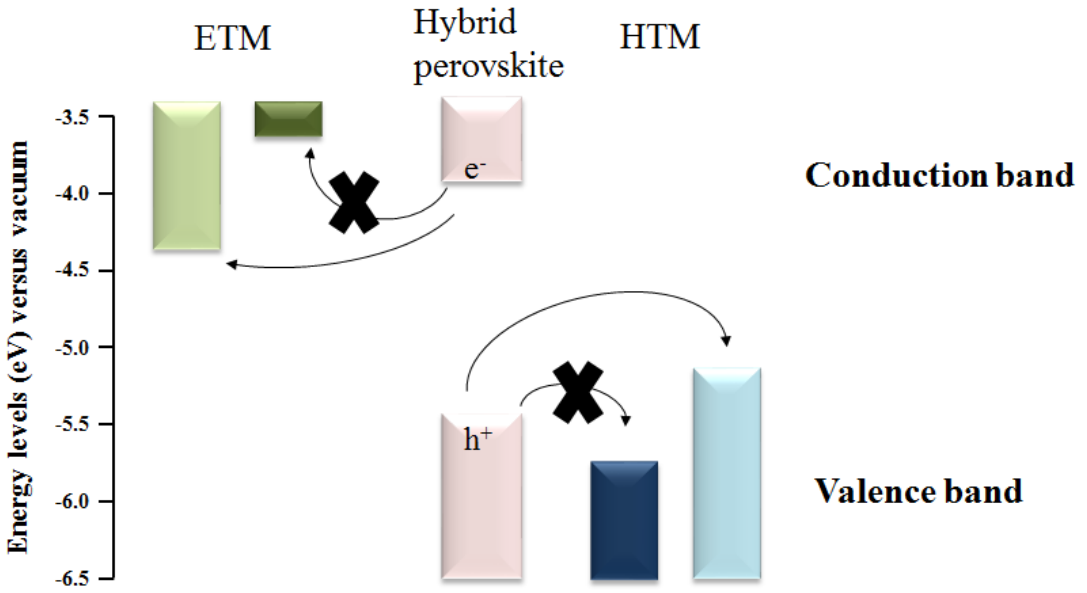

Figure 10 Schematic representation of the band edge alignment of ETM and HTM with respect to a hybrid perovskite layers. Electrons in the CB can only be injected into ETM materials whose CB edge energy value is more negative than that of the hybrid perovskite. As drawn, electron injection into the light green CB is energetically favourable whereas injection in the dark green CB is unfavourable. Same holds for the hole injection but in opposite manners, the VB edge of the HTM should lie higher in energy than that of the hybrid perovskite. The energy levels are given with respect to a free electron in vacuum.

In figure 11, band edge positions are given for a range of insulator materials, ETM, HTM and $MAPbI_3$. Two interesting HTM are the p-type semiconductors NiO and Co_3O_4 metal oxides. These inorganic oxides can easily be deposited with a variety of deposition methods in the presence of air or oxidizing compounds such as CVD,ALD, PVD, electrodeposition, spray-pyrolysis and spin coating from inexpensive metal salts such as the respective metal acetates, nitrates and chlorides [35]–[40]. Furthermore the VB edge alignments of these materials are good with respect to $MAPbI_3$ where the miss alignment between $MAPbI_3$ and NiO is only 0.2 eV and for Co_3O_4 only 0.03 eV meaning that the photogenerated holes can easily be injected without losing much of their potential energy in the process.

NiO has an optical band gap between 3.4 and 4.0 eV [35], [41]–[45] making it a wide band gap semiconductor. This wide band gap makes it very appealing as the blocking layer at the bottom side of the PV cell since NiO will barely attenuate the incoming visible light due to absorption processes. However, being a wide band gap semiconductor the hole conductivity of this material is low based on equation 1. The conductivity is however a function of the deposition method and the annealing temperature due to the level of Ni^{2+} vacancies in the crystal lattice which make NiO a p-type semiconductor [41]. Furthermore, a dopant can be introduced to increase the p-type conductivity. Copper has already been investigated as a dopant for a NiO HTM in a hybrid perovskite inverse planar heterojunction PV with a reported PCE value of 15.4% whereas for the undoped NiO HTM the PCE was considerably lower at 9.51% [34], [46]. Another interesting dopant to improve the conductivity of NiO would be divalent cobalt. Ni^{2+} and Co^{2+} have similar ionic radii of 0.69 and 0.72 Å meaning that Co^{2+} can be incorporated into the crystal lattice without inducing too much strain [41]. Furthermore, Co^{2+} has a $3d^7$ configuration and Ni^{2+} a $3d^8$ configuration. Substituting a Ni^{2+} ion in the crystal lattice by a Co^{2+} ion has therefore been reported to increase the p-type conductivity [37], [41].

Co_3O_4 has two optical band gaps within the visible light region of 1.5 eV and 2.2 eV [47]–[49]. These lower band gaps make it less interesting at first when compared to that of NiO. However, Co_3O_4 has been reported to have high hole conductivities making it an efficient HTM candidate and doping might not be necessarily [47] . Furthermore, the band alignment with the hybrid perovskite suffers only of a 0.03 eV mismatch. The use of a Co_3O_4 HTM has not been reported yet for $MAPbI_3$ PV to the knowledge of the author.

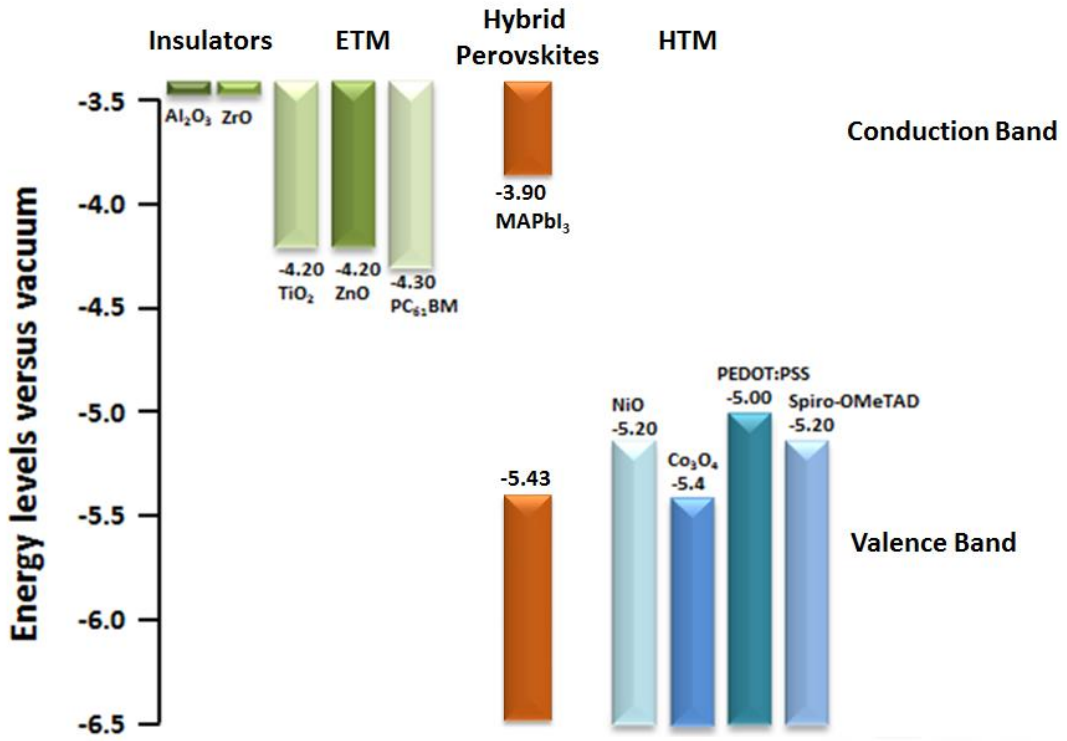

Figure 11 Band edge values for various insulators, ETM, the hybrid perovskite, $MAPbI_3$, and HTM species. Both organic and inorganic ETM and HTM layers are portrayed. Image is an adaptation from the original by Gao, et al.,[9].

1.4.4 State of the Art Hybrid Perovskite PV

The most investigated $MAPbI_3$ PV layouts are the mesostructured and normal planar heterojunction with TiO_2 as the ETM blocking and mesoporous layer and Spiro-OMeTAD as the HTM top layer. The efficiency of these PV increased from 9.7% to 15.0% as of 2014 [27], [50], [51] varying mostly on the deposition method used for the $MAPbI_3$ layer. However, in the attempt to further increase the PCE more complex systems have been developed. For instance, by mixing TiO_2 nanoparticles with liquid-phase exfoliated graphene sheets, a TiO_2/Graphene ETM blocking layer was deposited requiring annealing at only 150 °C compared to the 500 °C necessary for conventional TiO_2 blocking layers achieving a PCE value of 15.6% [12]. Recently $FAPbI_3$ as the hybrid perovskite in a PV cell achieved PCE values >19% with a champion device of 20.1% [52]. Also hole-conductor free hybrid perovskite PV have been investigated. Mei *et al.*, [53] used sequentially deposited mesoporous layers of TiO_2, ZrO_2 and carbon black which were infiltrated with $MAPbI_3$. TiO_2 acts as the ETM, and carbon black as the anode material. ZrO_2 acts as the inert scaffold to prevent TiO_2 and carbon black from coming into contact which would short-circuit the PV cell. A PCE value of 12.8% was reported for such PV cells with over 1,000 hours of stable performance under illumination. The investigation into creating multi junction devices with hybrid perovskites has also been looked into. Multi junctions have the possibility to achieve higher theoretical maximum PCE values than single junctions. Multi junction devices have been prepared by bridging $MAPbI_3$ with both crystalline and amorphous silicon PV leading to PCE values of respectively 13.7 and 12.8% which are still lower than the single junction $MAPbI_3$ PV though [54], [55]. Beside the development of the $MAPbI_3$ PV itself, Luo *et al.* [22] looked at the possibility of combining $MAPbI_3$ PV devices with electrolysers for the water splitting reaction. In their setup they connected tandem $MAPbI_3$ PV cells via external wiring to electrodes functionalized with nickel iron layered double hydroxides on nickel foam. They report a PCE of 15.7% for the tandem PV device and a Solar-to-Hydrogen efficiency (STH) of 12.3% which is close to the record efficiency of a PEC tandem cell of 14% [22], [56]. The PV driven electrolysis offers the benefit that the $MAPbI_3$ cell itself does not have to be in contact with water for the water splitting reaction to take place with comparison to a hypothetical $MAPbI_3$ PEC cell.

For hybrid perovskite PV to become commercially attractive with respect to the "grandfather" of PV, monocrystalline silicon, a few conditions have to be met in the future. One of these already mentioned earlier is the stability of these hybrid perovskite PV cells. With the hybrid perovskites themselves generally being unstable in moisture, the stability of these devices should be considered as important as the solar energy conversion efficiency. However, research groups have managed to reach stable PCE values >10% for 500 to more than 1000 hours [34], [53], [57], for instance by covering the hybrid perovskite with a thick hydrophobic porous carbon anode. Besides the importance of testing and improving the stability towards years of operating surface (>10,000 hours) for commercial applications, the active layer deposited area should also be taken into account. In general, the smaller the area illuminated, the higher the cells PCE value. All of the reported hybrid perovskite PV mentioned in this report so far have deposited areas <1 cm^2 whereas laboratory prepared silicon waver modules of 155.1 cm^2 have achieved a PCE value of 24.2% for the champion device [58]. Larger area hybrid perovskite PV cells have been reported such as by Chern, *et al.*, [59] with a PCE of 10.2% for 64 cm^2 devices. Finally and perhaps the most important condition is to exceed the efficiency achieved by large scale silicon PV which will drive the cost per Watt down.

1.5 Research Aim

The aim of this research is to investigate the deposition and application of undoped and Co^{2+} doped NiO and undoped Co_3O_4 thin film in hybrid perovskite PVs. The aim will be divided into four parts.

Part I: The fabrication of HTM thin films of NiO, Co^{2+} doped NiO and Co_3O_4 on both conductive FTO and non-conductive glass slide substrates.

Part II: Deposition of the hybrid perovskite material $MAPbI_3$ on a number of substrates such as FTO, glass slides and on the nickel and cobalt oxides

Part III: The hole injection and charge carrier transient absorption will be probed at the interface of $MAPbI_3$ with the HTM layers. Hole injection will be investigated with photoluminescence (PL) and with transient absorption spectroscopy (TAS) the charge carrier dynamics are probed.

Part IV: Attempts will be made towards the fabrication of complete hybrid perovskite PV cells to investigate the photon-to-current efficiency under illumination.

2. Methodology

2.1 Chemicals

Nickel acetate tetrahydrate was purchased from Acros Organics, 99% purity. Cobalt acetate tetrahydrate was purchased from Acros Organics, 97% purity. Lead (II) iodide was purchased from Sigma-Aldrich, 99% purity. Methylammonium iodide was purchased from Sigma-Aldrich, 98% purity. N,N-Dimethylformamide, extra pure, was purchased from Acros Organics. Both Anhydrous isopropanol, 99.5% purity, (synthesis) and technical grade isopropanol (cleaning) obtained from Sigma-Aldrich were used. [6,6]-Phenyl C61 butyric acid methyl ester, PCBM, was purchased from Solenne, 99% purity. Chlorobenzene was purchased from Acros Organics, 99+% purity. Silver sputtering target was purchased from Hauner Metallische Werkstoffe, 99.99% purity. Zinc powder was purchased from Sigma-Aldrich, >95,0% purity. Soda-lime Microscopic glass slides ~1 mm thickness, Menzel-Gläser, supplied by Thermo Scientific were used. Fluoride doped tin oxide (FTO) TEC 15 2.2 mm thickness with a sheet resistivity of 12-14 ohm/sq was used. All chemicals and the sputtering target were used as is without further purification. Microscopic glass and FTO substrates were cleaned thoroughly before used as discussed in the next section.

2.2 Substrate Cleaning and FTO Etching

FTO and glass substrates of roughly 6 x 3 cm (Length x Width) were superficially cut at every 1.5 cm for easy breaking into single substrates after cleaning. To get a uniform coating of the substrates with any technique it is important to remove any dust particulates and organic residuals on the substrate surface. The substrates were first washed with soapy water to remove large particles and organic residuals. Afterwards the substrates were put in a beaker filled with DI water, ethanol and acetone in a 1:1:1 volumetric ratio. The beaker was then placed in an ultrasonication bath for 15 minutes. Afterwards the substrates were washed with DI water in the beaker for four times. The substrates were then taken out and dried by a nitrogen gas line and put into a beaker filled with technical grade isopropanol. The beaker was placed into the ultrasonication bath for 15 minutes again. The substrates were then blown dry with a nitrogen gas line and put in a UV-Ozone cleaner. The UV-Ozone step cleans the surface of any leftover organic particles via a paired carbon-carbon bond activation and ozone formation using deep UV radiation. The UV-Ozone cleaning step took 20 minutes and besides further removing organic residuals also creates –OH group terminals on the surface of the substrates making them more hydrophilic.

The FTO substrates that were coated with the HTM, $MAPbI_3$, ETM and cathode layers for complete $MAPbI_3$ PV cells were partially etched. This etching removes the FTO layer in a certain pattern. The etching step was done before the cleaning step by mixing metallic zinc powder with DI water to give a slurry mixture and applying it on the non-protected surface of the substrates. 3M HCl was then added dropwise to the zinc slurry. The metallic zinc reduced the FTO layer. The substrates reacted with the zinc HCl slurry for about 15 minutes before being washed first with DI water then with 1M HNO_3 to remove metallic Sn and finally again with DI water. After etching the FTO, the substrates were cleaned as described above. Defining the etching area was done by masking the parts of the FTO to be left intact with Kapton tape.

2.3 The Spin Coating Technique

Spin coating is a sol-gel technique which allows the deposition of thin films on a substrate [60]. The substrate is placed on a sample holder, the chuck, which holds the substrate in place during spinning via either vacuum or a depth profile (recessed). A precursor solution is then injected on the substrate either before spinning called static dispense or during spinning called dynamic dispense. As the chuck is spinning at a certain speed, the majority of the solvent is ejected of the substrate in a radial pattern. During this step the entire substrate surface is covered assuming that the solvent properly wets the substrate surface. As the solution is spreading on the substrate, the solvent is evaporating to leave behind a film with a high concentration of the dissolved species, a gel-like film [60]. There are a number of variables which influence the final film morphology in spin coating such as spin coating speed, the number of steps, the time per step, the acceleration and deceleration towards each step, the local humidity, static or dynamic dispense, the volume of liquid injected for surface coverage, the hydrophilic/hydrophobic nature of the substrate surface that governs wetting properties but also substrate temperature and solution temperature at the moment of injecting [60]. All these factors will determine the obtained thin film thickness and morphology. These variables will be described below specifically for each different method.

A Photo Resist Spinner Model 4000 from Electronic Micro systems is used for spin coating thin films. The substrate area was about 1.5 x 3 cm^2. The substrates were placed in a recessed chuck. Injection of any precursor solution or dispersion was done with a Finn pipet. For the 1.5 x 3 cm^2 substrates 50 µL of the relevant precursor solutions were injected onto the substrate surface under dynamic dispense conditions. All spin coating steps were performed outside a glove box in a fume hood where. The local relative humidity within the spin coater was kept under 20% by flowing dry air at 1 bar in the coating bowl using a gas line connected to one inlet and an outlet was present for the evacuation of fumes. The uncontrolled relative humidity in the room was between 20 and 55%.

2.3.1 HTM Thin Film Spin Coating: NiO, Co^{2+} doped NiO and Co_3O_4

The method used here to fabricate NiO, Co^{2+} doped NiO and Co_3O_4 thin films is an adaptation of a method developed by Jlassi, *et al.*, [44] where the choice of solvent in this research was ethanol instead of 2-methoxyethanol. In table 1 a summary is given for the concentration of nickel and cobalt precursors in a combined ethanol and monoethanolamine (MEA) solution. For solutions A and G respectively 0.3 M and 0.1 M MEA was first dissolved in 10 mL dry ethanol for about one hour under magnetic stirring. Then the amount of nickel or cobalt acetate tetrahydrate was added in a 1:1 ratio with MEA to the solution under stirring. After adding the hydrated metal salts the solutions were sealed with Parafilm and covered with aluminium foil or placed in a dark cabinet and stirred for about 16 hours at 400 rpm before use. Additional information about the preparation of solutions B-F is given in table 2. First a specified concentration of 1:1 nickel acetate tetrahydrate and monoethanolamine in ethanol is prepared in a certain volume according to columns two and three, table 2, in the same manner that solution A was prepared. Then from solution G a certain volume was added to those of solutions B-F according to the fourth column to create the final mixed metal salt precursors. These solutions were also sealed with Parafilm and stirred for approximately 16 hours at 400 rpm in the absence of light.

Table 1 The solutions A-G which contain different concentrations of the nickel and cobalt precursors in a 1:1 ratio with MEA in dry ethanol. The total volume of all the solutions is kept at 10 mL in glass vials.

Solution name	$Ni(CH_3CO_2)_2 * 4H_2O$ (M)	$Co(CH_3CO_2)_2 * 4H_2O$		Monoethanolamine (M)
		Molarity	Mol%	
A	0.3	0	0	0.3
B	0.2997	0.0003	0.1	0.3
C	0.2985	0.0015	0.5	0.3
D	0.297	0.003	1	0.3
E	0.285	0.015	5	0.3
F	0.27	0.03	10	0.3
G	0	0.1	100	0.1

Table 2 Solutions B-F showing the concentration of the nickel precursor and the volume of the cobalt precursor solution added. A certain volume of the cobalt precursor solution, G, was added to solutions B-F as specified in the fourth column to create a final 10 mL solution with the mol% cobalt precursor from table 1 column four.

Solution name	$Ni(CH_3CO_2)_2 * 4H_2O$ (M)	Volume ethanol before adding solution H in mL	Added volume solution H in mL
B	0.2997	9.97	0.03
C	0.2985	9.85	0.15
D	0.297	9.7	0.3
E	0.285	8.5	1.5
F	0.27	7	3

All metal oxide thin films were coated on the substrates by spin coating. The substrates were spun at 2000 rpm for 30 seconds. As soon as the final speed was achieved the relevant precursor solution was injected at once onto the substrate. After each spin coating step the substrate is first allowed to evaporate slowly at room temperature in air for 10 minutes. They are then transferred to a hotplate at 100 °C for 10 minutes to further evaporate ethanol after which the temperature is increased to 300 °C for 30 minutes to partially decompose the metal salt and solidify the thin film. After 30 minutes the films are cooled down after which the spin coating cycle can be repeated to create thicker films. Finally, the substrates are transferred to an oven where the precursors are fully decomposed at 500 °C for 3 hours with a ramp of ~8 °C/min, and the metal oxides are formed.

In table 3 a summary is given of the different metal oxide thin films prepared on both glass and FTO substrates and the number of spin coating cycles they underwent with respect to the characterization technique performed. In principles Co_3O_4 layers underwent three times more spin coating cycles compared to NiO or Co doped NiO layers due to the three times lower molarity of the precursor solution used for Co_3O_4. Thicker layers were prepared of most samples for XRD measurements to get a sufficient signal. The sample names of 0.1-10% Co refer to the relative concentration of Co^{2+} in the precursor solution rather than the actual amount of Co^{2+} doping in the NiO crystal structure.

Table 3 Summary of the metal oxide films prepared on different substrates. The characterization techniques applied to these specifically coated substrates is given with the number of spin coating cycles those characterized samples underwent. Different spin coating cycles are applied because of the sensitivity of each characterization technique and to study thickness effects on coating profiles.

Sample Name	Substrates	Characterization Technique (spin coating cycles)
NiO	Glass	XRD (4) FIB-SEM (4) UV-Vis (2)
NiO	FTO	FIB-SEM (1) UV-Vis (2)
0.1% Co	Glass	XRD (4) UV-Vis (2)
0.5% Co	Glass	XRD (4) UV-Vis (2)
1% Co	Glass	XRD (4) UV-Vis (2)
5% Co	Glass	XRD (4) UV-Vis (2)
10% Co	Glass	XRD (4) UV-Vis (2)
Co_3O_4	Glass	XRD (4) UV-Vis (6)
Co_3O_4	FTO	FIB-SEM (3) UV-Vis (6)

2.3.2 Hybrid Perovskite Thin Film Fabrication

Three general methods have been developed for the fabrication of thin hybrid perovskite films with a spin coater. They are called one-step deposition, sequential deposition and two-step deposition [31], [50], [61]–[66]. As discussed in section 1.4.2 the crystallization plays a key role in efficient hybrid perovskite PV cells due to an increase in the diffusion length of both holes and electrons with an improvement of crystallinity by reducing grain boundaries, defects and pinholes. The first method, the one-step deposition is the simplest synthesis method where the precursors, PbI_2 and MAI, are dissolved together in DMF and the hybrid perovskite layer is spin coated in a single step. This method leads to such rapid crystallization effects that the hybrid perovskite layers often are of worse quality due to pinholes and defects compared to the other two methods [61], [64], [67]. The sequential deposition method improved the layer formation by first spin coating a solution of PbI_2 in DMF to form a PbI_2 thin film and then immersing this film in a chemical bath of MAI dissolved in isopropanol for a few tens of seconds [50], [62], [63]. Finally, by heating the substrate the hybrid perovskite will be formed. However the sequential deposition method has been reported to be less effective for creating thicker hybrid perovskite films due to diffusion limitations. The last method has been reported to get rid of this partial conversion for thicker hybrid perovskites. First a thin film of PbI_2 is spin coated in the two-step deposition method [31], [66], [68]. In the next step the MAI in isopropanol is spin coated on top of the PbI_2 film. Upon contact the two layers already react to give a partial hybrid perovskite phase. Applying a thermal treatment then fully converts the two layers in a single hybrid perovskite layer. These three deposition methods are visualized in figure 12.

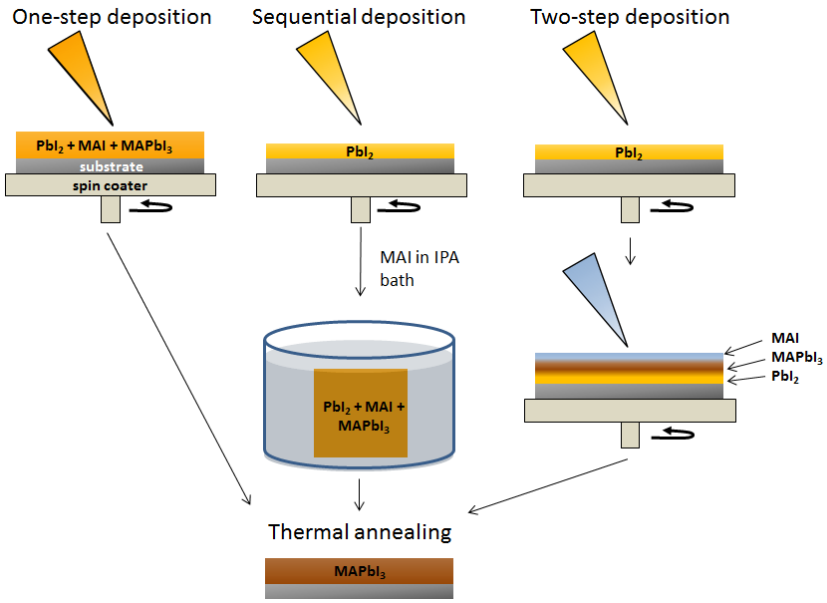

Figure 12 Schematic representation of the three different deposition methods. The one-step deposition is the most facile method but the sequential and two-step deposition methods lead to higher performing films. In all cases a final annealing step is required to obtain a fully converted crystalline hybrid perovskite. To simplify the situation, all the different type of substrates are visualized in the same manner

In table 4, the different hybrid perovskite precursor solutions are shown corresponding to the deposition methods. All PbI_2 containing solutions were stirred and kept at 70° C for a minimum of three hours to ensure complete dissolution. Furthermore these solution were stirred either in dark or covered with aluminium foil. The MAI bath or spin coating solution were prepared by dissolving the MAI salt under stirring in IPA, sealed of the glass vials with Parafilm and stirred overnight in dark. Regardless of the spin coating method, all $MAPbI_3$ films were coated via a single cycle since the precursor solvents would dissolve the previously coated $MAPbI_3$ film if multiple cycles were done. For the one-step deposition adapted from [64], the substrates were kept at 100 °C on a hotplate and transferred to the spin coater. As soon as the spin coater was at 3000 rpm, the precursor solution kept at 70 °C was injected. The duration of the spinning was 30 seconds. Initially after spinning the obtained films looked scattering and bright yellow. After the spinning step, the substrates were placed on a hotplate at 100 °C and annealed for 45 minutes to form the final hybrid perovskite layer which was scattering and dark black. For the two-step deposition, adapted from [68], first the PbI_2 layer was coated on a substrate kept at 75 °C on the hotplate. The PbI_2 precursor kept at 70 °C was injected on the substrate while it was spinning at 6400 rpm. After injection the substrate kept spinning for 30 seconds. After spinning, the substrates were dried at 75 °C for 15 minutes. The second precursor, MAI, was spin coated on top of the PbI_2 layer. The substrate was again kept at 75 °C and the spin speed and duration were 6400 rpm and 30 seconds. The MAI precursor solution was kept at room temperature. As soon as MAI was injected on top of the PbI_2 film an orange/brownish film was obtained. After the thermal treatment at 100 °C for 45 minutes a semi-transparent dark brown film was obtained. Finally, for the sequential deposition method based on [50], the PbI_2 film was coated the exact same way as for the two-step deposition except that the PbI_2 molarity was 1M instead of 0.7M.

After this coating, the PbI_2 layer was immersed fully into the MAI in IPA chemical bath for 60 seconds at room temperature. During this time the yellow substrates turned brown. The substrates were then taken out and immersed a few times in a beaker with IPA to wash off any excess MAI. Finally the substrates were placed back on the hotplate at 75 °C for 30 minutes to obtain a scattering, non-transparent black film. A comparison of XRD, UV-Vis and FIB-SEM data obtained from the three deposition methods is shown in appendix C which led to the choice of the two-step deposition method for the fabrication of $MAPbI_3$ thin films within this research.

Table 4 Combination of precursor solutions used to prepare the PbI_2 and MAI precursor layers and finally the $MAPbI_3$ hybrid perovskite. The three different methods described above and visualized in figure 12 were utilized.

Method	Pb^{2+} source solution	MAI solution
one-step dep.	0.88 M PbI_2 & 2.64M MAI mixed in DMF	
two-step dep.	0.7 M PbI_2 in DMF	0.31 M MAI in IPA
sequential dep.	1 M PbI_2 in DMF	0.05 M MAI in IPA

Table 5 below lists the prepared $MAPbI_3$ samples. For $MAPbI_3$ coated on the metal oxide thin films which act as HTM, the number of spin coating cycles these HTM underwent is two. This is done to minimize photon absorption of these HTM layers for the optical characterization techniques: UV-Vis, PL and TAS measurements.

Table 5 The samples names of different substrates namely glass, FTO and HTM coated glass from table 3 coated with $MAPbI_3$. The characterization techniques used for these samples are given. Furthermore, all metal oxide HTM layers were coated on the glass substrates from two spin coating cycles before being coated with $MAPbI_3$.

Sample name	Substrate	Characterization Technique	HTM substrate spin coated cycles
$MAPbI_3$ on glass	glass	XRD, UV-VIS, PL, TAS	-
$MAPbI_3$ on FTO	FTO	XRD, FIB-SEM, UV-VIS	-
NiO	glass	XRD, UV-VIS, PL, TAS	2
0.1% Co	glass	XRD, UV-VIS, PL, TAS	2
0.5% Co	glass	XRD, UV-VIS, PL, TAS	2
1% Co	glass	XRD, UV-VIS, PL, TAS	2
5% Co	glass	XRD, UV-VIS, PL, TAS	2
10% Co	glass	XRD, UV-VIS, PL, TAS	2
Co_3O_4	glass	XRD, UV-VIS, PL, TAS	2

2.3.3 ETM Thin Films: PC61BM

The organic fullerene-derivative $PC_{61}BM$ was spin coated on top of the FTO-NiO-$MAPbI_3$ layers to form the p-i-n heterojunction for full PV devices. 20 mg/ml $PC_{61}BM$ was dissolved in typically 2 mL chlorobenzene under stirring. The vial was then sealed with Parafilm and stirred further overnight. Before use the $PC_{61}BM$ precursor solution was sonicated for five minutes and filtered with a 0.45 µm filter to remove any large aggregates. A thin layer of $PC_{61}BM$ layer was spin coated at 1,000 rpm for 20 seconds followed by solvent evaporation at 85 °C for five minutes on a hotplate. After this the substrates were transported in closed glass vials filled with argon to the sputter coater to deposit a thin silver cathode layer.

2.3.4 Sputtering Silver Cathode Layer

The last step is the deposition of a thin silver cathode layer on top of the $PC_{61}BM$ layer using a sputter coater to complete the hybrid perovskite PV cells. Approximately a 80 nm thick silver layer is sputtered using an argon plasma at low pressure and a 99.99% silver sputtering target. The deposition rate was roughly 0.05 nm/sec in a 250 mm high chamber at 0.01 mbar and 40 mA current. A home-made cathode mask was used to selectively coat a pattern on top of the $PC_{61}BM$ layer leaving other parts uncoated as shown in figure 13 below. The cathode sputtering mask was in contact with the substrate during deposition to achieve a well-defined area of deposition.

The final obtained PV cells had the following layout: FTO-NiO-$MAPbI_3$-$PC_{61}BM$-Ag and are simply referred to as complete $MAPbI_3$ PV cells further on.

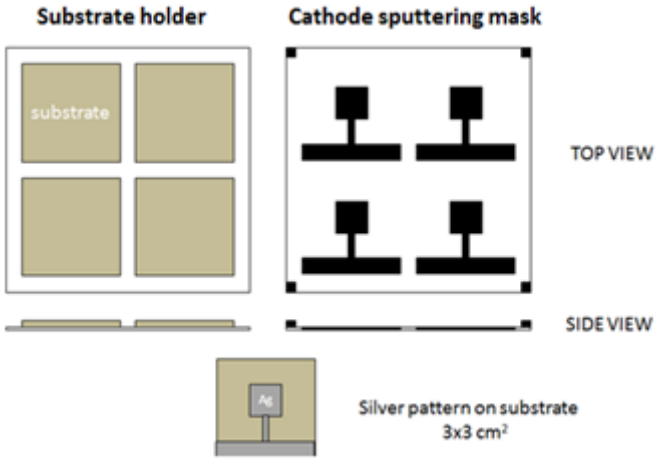

Figure 13 The design for the home-made cathode sputtering mask. Both the holder and mask were cut out of a ~1mm thick aluminium plate. The dark contours in the mask design show empty voids which depict the deposition area on the substrate. The substrate and mask were in close-contact during deposition to avoid significant shadowing.

2.4 Characterization Methods

2.4.1 X-ray Diffraction

To probe the crystal structure of the fabricated thin films, XRD can be used. The collective constructive scattering of the incoming x-ray beam at the planes of the crystal lattices separated by the interplanar distance, *d*, give rise to reflections that obey Bragg's law from equation 8a [69]. Bragg's law is composed of the interplanar distance, *d*, the angle of diffraction, θ, an integer, *n*, and the wavelength of the x-ray beam, λ in Å. In equation 8b, θ is the angle of diffraction, λ is the wavelength of the x-ray Kα source in Å, *h,k,l* are the Miller indices and *a,b,c* are the unit cell dimensions which in the case of a cubic crystal lattice $a=b=c=a_0$. In equation 8c, *D* is the crystallite size in Å, *K* an instrumental broadening factor which is defined as 0.89 in this research, λ the wavelength of the x-ray Kα source in Å, β is the full width at half maximum (FWHM) and θ the diffraction angle. In this research, x-ray diffraction is used to confirm the presence or absence of metal oxides, the hybrid perovskite $MAPbI_3$ and its precursors: PbI_2 and MAI, calculate the crystal unit parameters to probe the effect of doping Co^{2+} into the NiO crystal lattice and to calculate the crystallite size of these films using equations 8b-c.

$$2d\sin\theta = n\lambda \tag{8a}$$

$$sin^2(\theta) = \frac{\lambda^2}{4}\left(\frac{h^2}{a^2}+\frac{k^2}{b^2}+\frac{l^2}{c^2}\right) \tag{8b}$$

$$D = \frac{K\lambda}{\beta\cos\theta} \tag{8c}$$

A Bruker D2 Phaser designed for powder diffraction was used. Both the beam source and detector were moving from low to high angles as the x-ray diffraction of the thin films was being measured. The result was that both the bulk substrate and the thin films were probed instead of only the surface which requires grazing incidence XRD at low constant beam angles. For the hybrid perovskites measurements were done between 5 – 65° 2 θ at an increment of 0.01° with a copper Kα x-ray source. For the metal oxide thin films the 2 θ range was 30-80° with an increment of 0.04° and both copper and cobalt Kα x-ray sources were used. For the metal oxides deposited on a glass substrate, the glass substrate back ground was subtracted.

2.4.2 UV-Vis Spectroscopy

UV-Vis spectroscopy was utilized in transmission mode to confirm material composition via material specific features. The spectra were converted into absorbance units using equation 9 which relates transmission, %T, to absorbance. No correction for reflectance and scattering could be made, thus the reported absorbance values are the sum of reflectance, scattering and absorption. For thin films, reflectance plays a potentially large role due to the interference of visible light with thin films in the order of tens of nm to a few µm. This interference leads to constructive and destructive patterns of photons of certain wavelengths within the material and appear as interference fringes in a UV-VIS spectra. Especially when multiple thin films are interfaced such as NiO on FTO the interference fringes can take on complicated patterns.

$$\text{Absorbance} = -\log\left(\frac{\%T}{100}\right) \tag{9}$$

A Varian Cary® 50 UV-VIS Spectrophotometer with a dual beam, full spectrum xenon pulse lamp and dual Si diode detectors was used for the measurements. The thin film substrates were placed against the opening of the detector for the measurements at a 90 ° incident angle with the incoming beam. A substrate subtraction was performed by measuring first the uncoated substrate and subtracting this spectra from that of the coated substrates.

2.4.3 Focused Ion Beam - Scanning Electron Microscopy

FIB analysis was performed with a FEI Nova Nanolab 600 [70]. FIB-SEM allows both the investigation of the surface morphology with resolutions <10 nm for state of the art devices as well as the preparation of a cross-section of the samples with the FIB attachment [70], [71]. The working principles are based on focusing an accelerated electron beam onto the sample and looking at the back-scattered electrons with detectors. By the sputtering a thin conductive metallic film on top of the sample and focusing an ion beam, a cross-section can be prepared. By looking at this cross-section with a tilted angle the layer thickness can be determined due to the reference deposited metallic layer who's thickness is known from the deposition rate [71].

2.4.4 Photoluminescence

With photoluminescence the radiative recombination of excited species is probed and can be used to investigate how efficient a material luminesces or more precisely how much of the recombination events occurs radiative after excitation [72]. When the hybrid perovskite material is excited with a light source, electrons are generated in the CB and holes in the VB. These excited species can recombine radiatively, thus emitting photons that have an energy corresponding to the band gap of the hybrid perovskite which are collected by a detector. For $MAPbI_3$ PV devices steady-state photoluminescence measurements are used to investigate the quenching of the $MAPbI_3$ radiative recombination pathway due to interlayer charge separation. For a PV device to be efficient, the photogenerated free charge carriers have to be separated successfully from each other over large dimensions due to hole and electron injection into respectively the HTM and ETM layers. More precisely, the lower the rate of recombination of the photogenerated free charge carriers, the higher the efficiency will be of a PV device. Therefore, the photoluminescence quenching of the radiative recombination of the hybrid perovskite is investigated when interfaced with a HTM layer. In this research photoluminescence is used to investigate how successfully hole injection from the $MAPbI_3$ layer into the NiO, Co^{2+} doped NiO and Co_3O_4 HTM layers is. A higher quenching efficiency refers to a better hole injection thus to better free charge carrier separation between the MAPbI3 and HTM $_{layers}$. These quenching values can be used as a crude indication for suitable HTM metal oxides $MAPbI_3$ PV. Generally, quenching efficiency values lay between 98% and 99+% for efficient HTM quenching layers [18], [46], [73]. In figure 14 the photoluminescence quenching of the $MAPbI_3$ radiative recombination is sketched due to the interface with the hole accepting layers.

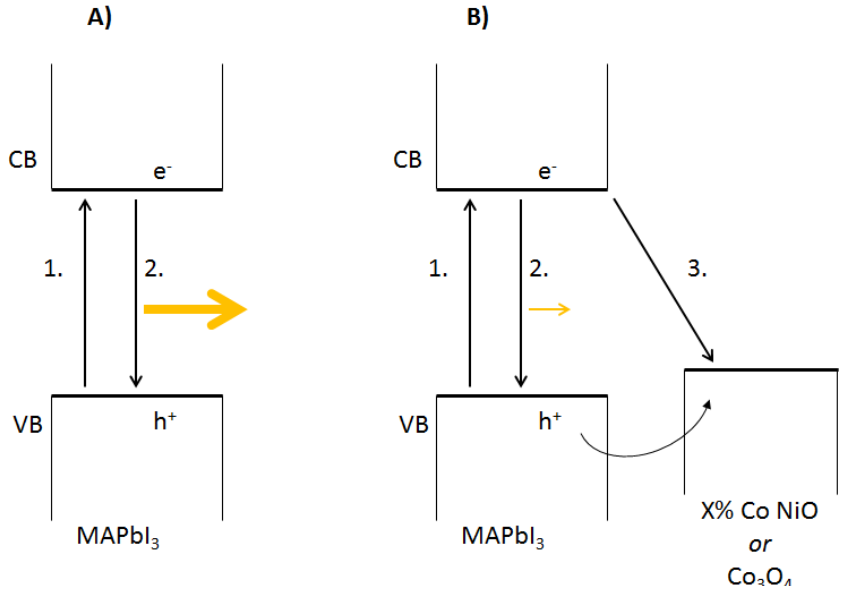

Figure 14 Quenching of the photoluminescent signal of the hybrid perovskite $MAPbI_3$ due to effective free charge carrier separation over large distance due to hole injection into the metal oxide HTM layer. Situation A) is the reference cell where the hybrid perovskite on SiO_2 has photoluminescence intensity I_0. Arrow 1. indicates hybrid perovskite excitation to generate free charge carriers in the CB and VB. Arrow 2. refers to the radiative recombination of the electron in the CB and the hole in the VB of the hybrid perovskite. In situation B, hole injection into the metal oxide HTM layers lowers the probability of radiative recombination of the free electron and hole within the hybrid perovskite and therefore quench the photoluminescent signal. A new possible pathway of recombination is shown in arrow 3 which can be both radiative and non-radiative recombination at the interface of the two layers.

Steady-state photoluminescence experiments are done with an Edinburgh Instruments Spectrometer with a 450 W xenon arc lamp and a RED PMT detector for the visible light region. Sample excitation is done at 550 nm from the back side as shown in figure 14. Back side excitation was necessary with this setup to get a photoluminescence signal without significant signal artefacts. Appendix D shows the resulting spectra when the sample was illuminated from the front side. A disadvantage of back side illumination is that the part of the incoming beam can be attenuated by the glass substrate and metal oxide layers due to reflection and absorption processes and therefore influence the final photoluminescence signal. The quenching of the reference $MAPbI_3$ photoluminescence signal was calculated by integrating the area of the photoluminescence peak around 780 nm which corresponds to the $MAPbI_3$ band gap for each sample. Then according to equation 10 the quenching efficiency was calculated where $Area_{HTM}$ refers to the area under the photoluminescence peak from the $MAPbI_3$ layer deposited on the HTM metal oxides and $Area_{ref}$ refers to that of the $MAPbI_3$ layer on glass. However no integrating sphere is used within this setup and therefore any quenching efficiencies given, should only be used as indications.

$$\text{Quenching Efficiency (\%)} = 100\% - \left(\frac{Area_{HTM}}{Area_{ref}}\right) * 100\% \quad (10)$$

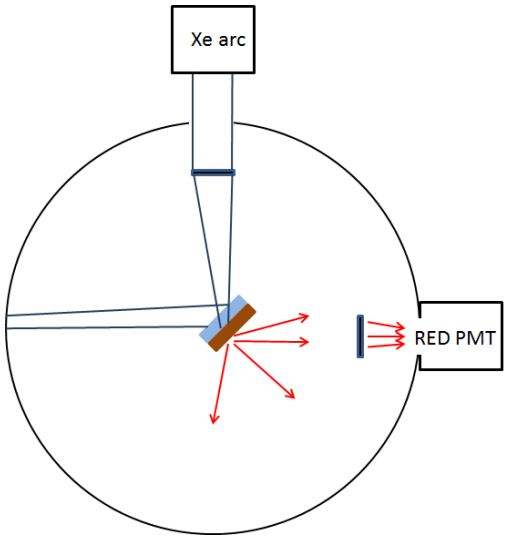

Figure 15 Schematic overview of the steady-state PL setup used. An incoming beam at a wavelength of 550 nm was focused on the sample with a lens. The sample was illuminated from the back side meaning through the microscopic glass side. The incoming beam is partially reflected this way into the surrounding black box instead of the detector. The top side of the sample with the hybrid perovskite is facing the detector at a rough 45 ° angle as shown in the figure. The emitted light from radiative recombination happening in the hybrid perovskite layer is that way still largely going to the detector. No integrating sphere is used.

2.4.5 Transient Absorption Spectroscopy

With TAS the change of absorption, ΔA, is measured of a sample using a pump and probe pulse which arrive at a pulse delay, Δt. Therefore the change of absorption is the difference in the absorption of the ground-state of the sample measured before the pump laser excitation and the absorption of the excited state of the sample. The principle of TAS is shown in Figure 16 [74].

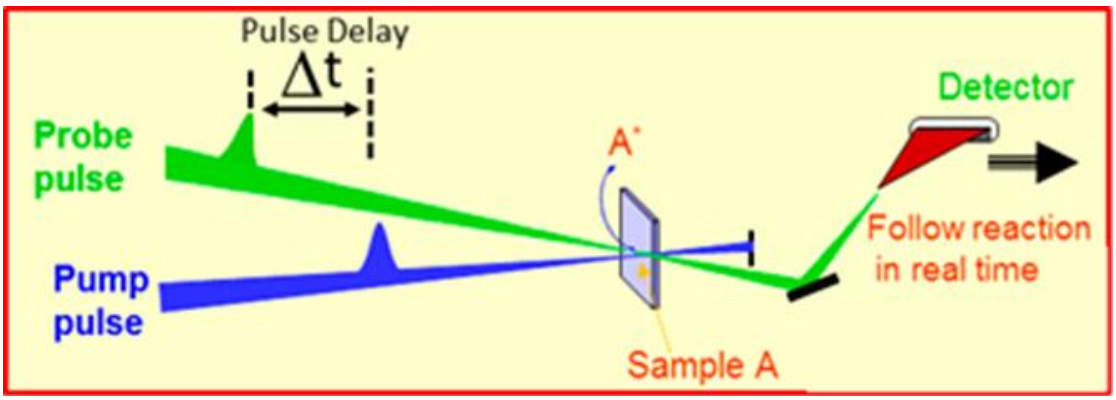

Figure 16 Transient absorption spectroscopy working principles. A pump pulse excites sample A. A probe pulse arrives at a delay time Δt and measures the change of absorption between ground-state absorption and excited-state absorption leading to a transient absorption signal of ΔA [74].

The time window in which processes are investigated depends on the pulse duration and frequency of the pump and probe. Laser pulse durations as low as 5 fs are possible and sub 50 fs processes can be investigated. However, even though lower pulse durations imply higher time resolution, the time-bandwidth product relation describes that for very short pulse durations the spectral bandwidth can be as high as 100 nm for a 800 nm laser. Thus a trade-off has to be made often between time and spectral resolution. Furthermore, the frequency determines how many pulses will arrive at the sample each second and thus what the longest timescale is that can be investigated. With a 100 kHz pulse, every ten nanoseconds a new pulse arrives and thus timescales longer than ten nanoseconds cannot be investigated [74]–[78].

Besides the time window, the energy of the pulse is also of great importance. The more energy a pulse contains, the more species will be excited in a sample. This can range between 0.1% to ~20% of the species being excited. At high percentages of excited species, the interactions between excited species becomes more and more prominent which may have an influence on the process of investigation as well as certain recombination processes may dominate such as the non-radiative Auger recombination [76].

Generally speaking, ΔA can originate from one of the four following phenomena. In the first case, a certain amount of the ground-state species has been excited by the pump. Therefore the ground-state has been partially depleted of electrons and the probability of excitation of the ground-state due to the probe pulse arriving Δt after the pump is lower. This lower probability translates in a lower absorption for the probe pulse arriving after the pump pulse compared to the reference spectra and thus a negative ΔA is measured. This situation is called the ground-state bleach. For $MAPbI_3$ the ground-state bleach corresponds to electrons from the VB being depleted upon excitation from the pump pulse. Holes are formed in the VB and

electrons in the CB. The ground-state bleach signal is therefore expected to be close to the band gap of 1.6 eV or 780 nm. The second case is that of stimulated emission. For optically allowed transition, when a photon from the incoming probe light has the same energy as an excited species, the excited species radiative recombination can occur where a photon with an energy close to the band gap energy is emitted. Therefore more photons are being detected and a negative ΔA signal is observed. Stimulated emission is stoke-shifted compared to the ground-state bleach meaning it happens at lower energy however the two peaks remain close enough that in practice a convolution of the two process is observed. The probe light is however of weak intensity to avoid multi-absorption processes and stimulated emission is therefore not expected to be significantly more intense than the ground-state bleach. The third process describes further absorption of photons from the probe light by excited species which are then excited to higher states as long as the transition is optically allowed. This transient absorption of excited species is detected as a positive ΔA signal. The fourth and last common process is called product absorption. After initial excitation of the sample with the pump pulse, further energy provided by the probe light might induce specific processes within the sample such as charge transfer and triplet state excitation. This process is just like the transient absorption in the third process measured as a positive ΔA [74]–[78].

The advantage of a technique such as TAS is that ultrafast processes such as charge injection between $MAPbI_3$ and the HTM layers could be investigated which occur on sub ns timescales [46], [77]. Furthermore, compared to PL the non-emissive and dark states can also be investigated with TAS because absorption features are observed of excited states instead of emission features [75].

An EOS Sub Nanosecond Transient Absorption Spectrometer with a Nd:YAG crystal pump laser was used for the TAS measurements. The Nd:YAG crystal pump laser generates a pulse with a wavelength of 1064 nm which is then split into the shorter wavelengths of 266 nm, 355 nm and 532 nm using a harmonic generator. The 355 nm generated laser pulse was used to excite the hybrid perovskite layer. A repetition rate of 1 kHz was used for the pump pulses with the pulse duration shorter than 1.8 ns. A neutral density filter allowed the control of the pump pulse energy. For most experiments the pump pulse energy was ~0.8 mW/cm^2. For the reference $MAPbI_3$ layer on glass a measurement was also performed at ~1.3 mW/cm^2. With an estimation of the spot size being 1 mm^2 and the repetition rate of 1 kHz a pump fluence of either 80 $\mu J/cm^2$ or 130 $\mu J/cm^2$ was realized. A LEUKOS super continuum light source was used for the probe pulse. A spectral window between 350 and 950 nm with a resolution of 2 nm could be investigated in combination with a visible light detector. The probe light frequency was 2 kHz and the pulse duration below 1.2 ns. The pulse duration therefore allows a time window between roughly 1 ns and 400 µs. A beam splitter is used to split the probe light pulses in which one half is transmitted to the sample and the other is directly send to a second visible light detector to serve as a reference spectrum for the monitoring of beam intensity fluctuations. The EOS Sub Nanosecond Transient Absorption Spectrometer setup is shown in figure 17. Analysis of the kinetic profiles is done by fitting the data with the double exponential function with x-offset shown in equation 11 below. Two lifetimes, namely τ_1 and τ_2 are calculated from the fitting. A_1 and A_2 are weighting factors of the exponential functions. X_0 and y_0 are the offset values at the minimum of the ground-state bleach signal.

$$y = y_0 + A_1 e^{-(x-x_0)/t_1} + A_2 e^{-(x-x_0)/t_2} \quad (11)$$

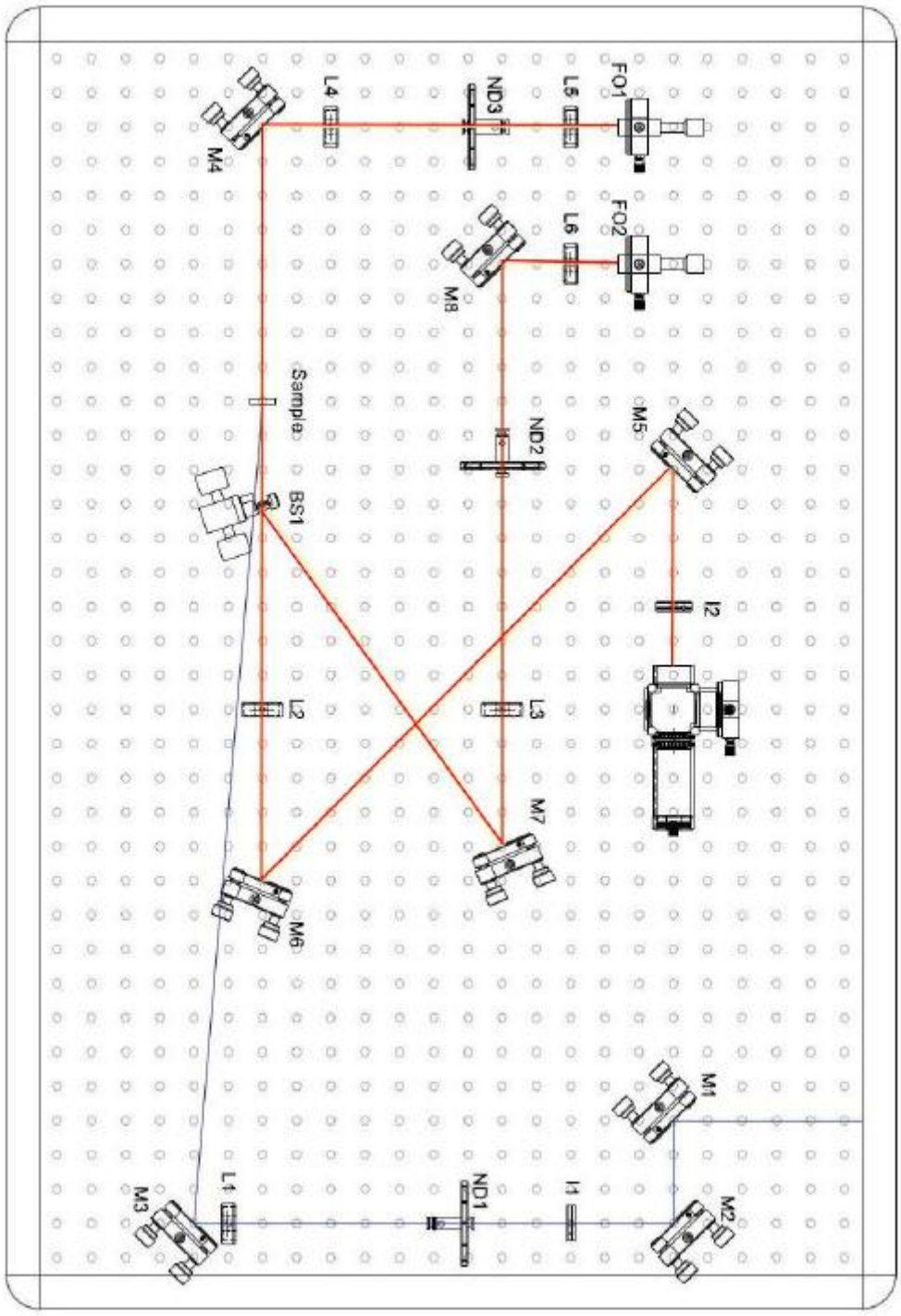

Figure 17 Layout of the EOS Sub Nanosecond Transient Absorption Spectrometer. The black line is the pump laser and the red line is the probe laser. M = mirror, ND= neutral density filter, L = Lens, BS= beam splitter and FO = fibre optics. The fibre optics are connected to the two visible light detectors.

2.4.6 Cyclic Voltammetry

CV measurements were performed using a PowerArc 75W xenon source lamp. The power density of the focused beam at the substrate position was measured with a silicon photodiode and found to be 59.9 mW/cm^2. UV and IR filters were used to filter out high energy photons. A scan rate of 10 mV/s was used and complete hybrid perovskite PV cells were investigated under forward bias. A 0.22 cm^2 mask was used to define the active area of the PV cells. The devices were not sealed and thus in contact with air/moisture during measurements. Poor electrical contacts were made with crocodile clips.

2.4.7 Different Cell Layouts Depending on Characterization Techniques

Two different cell coating profiles were used depending on the characterization techniques. For techniques such as UV-VIS, XRD, TAS, FIB-SEM and PL the entire substrate surface was coated with the relevant layers. For the fabrication of complete cells to be characterized with CV it was essential to partially etch the FTO substrate and apply a different coating pattern for each subsequent layer to prevent short-circuiting conditions.

There are mainly two reasons why this etching and partial coating is important. First of all, the anode (FTO) and cathode (Ag) layers have to be connected with wiring to an external circuit to probe the cells I-V characteristics. Therefore part of the FTO anode and Ag cathode layers have to be uncoated or uncovered in protective epoxy resin. In case of etching, often the first layer of FTO or any other TCO material is etched away at the position where the Ag cathode is connected to the external circuit. The main reason for this is to minimize the area at which the two ohmic contacts are present because of possible short-circuiting events. With short-circuiting it is meant that a very low resistive pathway is found for the dark current density to travel through the cell at low bias voltage. As mentioned before, in an ideal p-i-n junction cell the dark current density experiences a high resistance through the p-i-n junction until V_{oc} is reached but with short-circuiting an alternative pathway opens up. In figure 18 the layout of the complete $MAPbI_3$ PV cell is shown. The first light-blue layer is the glass substrate with the white-silver colored FTO layer partially etched on top. In dark blue the HTM layer is deposited. This HTM layer is coated in such a manner that part of the FTO is uncovered so that a connection to the external circuit can be made and part of the FTO etched part is covered to prevent the next layers from coming into contact with FTO. This same coating procedure is then repeated for $MAPbI_3$ in brown and the ETM $PC_{61}BM$ in green and Ag in grey so that none of these layers comes into contact with FTO or any other underlying layers except the previously coated one.

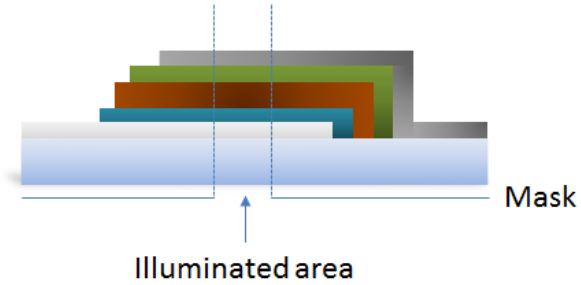

Figure 18 Cross-section layout of the individual coating pattern of each layer in a complete hybrid perovskite PV. From the bottom-up: glass, FTO, HTM, $MAPbI_3$, ETM, Ag.

3. Results and Discussion

3.1 Part I: Fabrication and Characterization of Metal Oxide Thin Films

In this chapter first the fabrication of undoped NiO and Co_3O_4 films will be discussed on both FTO and glass substrates in subsection 3.1.1 followed by the fabrication of Co doped NiO films on glass substrates in subsection 3.1.2.

3.1.1 Depositing Undoped NiO and Co_3O_4 Thin Films on Different Substrates

X-ray diffraction can confirm the presence of the desired crystal phase of a material as well as crystalline impurities which could arise from the precursor materials for example. As mentioned in section 2.4.1, the XRD setup used in this research does not allow grazing incidence analysis which increases substrate noise for thin films. Therefore, the XRD results for NiO and Co_3O_4 thin films shown in figure 19 are based on the coating of an amorphous glass substrate instead of the highly crystalline FTO substrate. By doing this, only the reflections of respectively the face-centered cubic (fcc) rock salt NiO and spinel Co_3O_4 structures are expected. Indeed, figure 18 shows that NiO and Co_3O_4 are the only crystalline phases found on the substrate. Considering that the precursor solution of Co_3O_4 is 0.1 M and NiO 0.3 M this translates in a probably three times thinner Co_3O_4 film compared to NiO. This could explain why the Co_3O_4 diffractogram is noisier after the background subtraction.

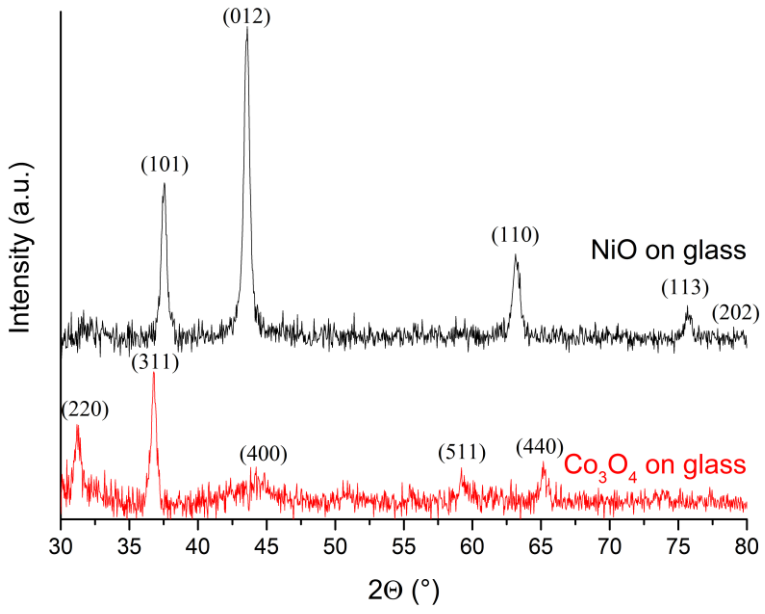

Figure 19 XRD results of both the NiO and Co_3O_4 films coated on a glass substrate. Both samples were prepared from four spin coating cycles. Measurements are done with a Cu Kα x-ray source.

Besides crystallinity of the metal oxide films, another important factor for the determination of a suitable HTM layer is how uniform the substrate is coated and if a dense or porous film is formed after the drying and annealing steps. In principle, a dense non-porous HTM layer is preferred on top of FTO to prevent the subsequently deposited $MAPbI_3$ film from coming into direct contact with FTO which would increase recombination effects and thus lower cell efficiency. In figure 20 FIB-SEM images are shown for NiO (A-B) and Co_3O_4 (C-D) deposited on FTO from respectively a single and triple spin coating cycle. Unfortunately, only for NiO a cross-section image is available which shows a layer thickness of 30 nm. Based on the relationship between concentration differences of 0.3 M for NiO and 0.1 M for Co_3O_4 and, respectively, the single and triple coating steps a similar thickness for Co_3O_4 is estimated. There are some clear differences however concerning the surface morphology of these layers. For the single coated NiO layer a clear porous surface is observed. The porosity is observed both in the cross-section and topview images. For Co_3O_4 such porosity is however not directly observed even though it still might be present beyond the spatial resolution of the utilized FIB-SEM machine. This difference could be of course due to a different interaction that the metal precursors have with the FTO substrate during the coating or the drying and annealing steps. However, it is also possible to be due to the different number of spin coating steps used. In a single spin coating step on the rough FTO surface, it seems to be the case that a dense layer cannot be formed. By employing multiple spin coating steps these porous channels of the metal oxide layer could be partially infiltrated and covered by the metal precursor to create an overall more dense film or at least surface. Based on this assumption it seems important to employ multiple coating steps of the metal oxide layers to be employed as HTM. Another option would be to switch to layer by layer growth deposition techniques such as CVD and PVD which are however more time consuming compared to spin coating.

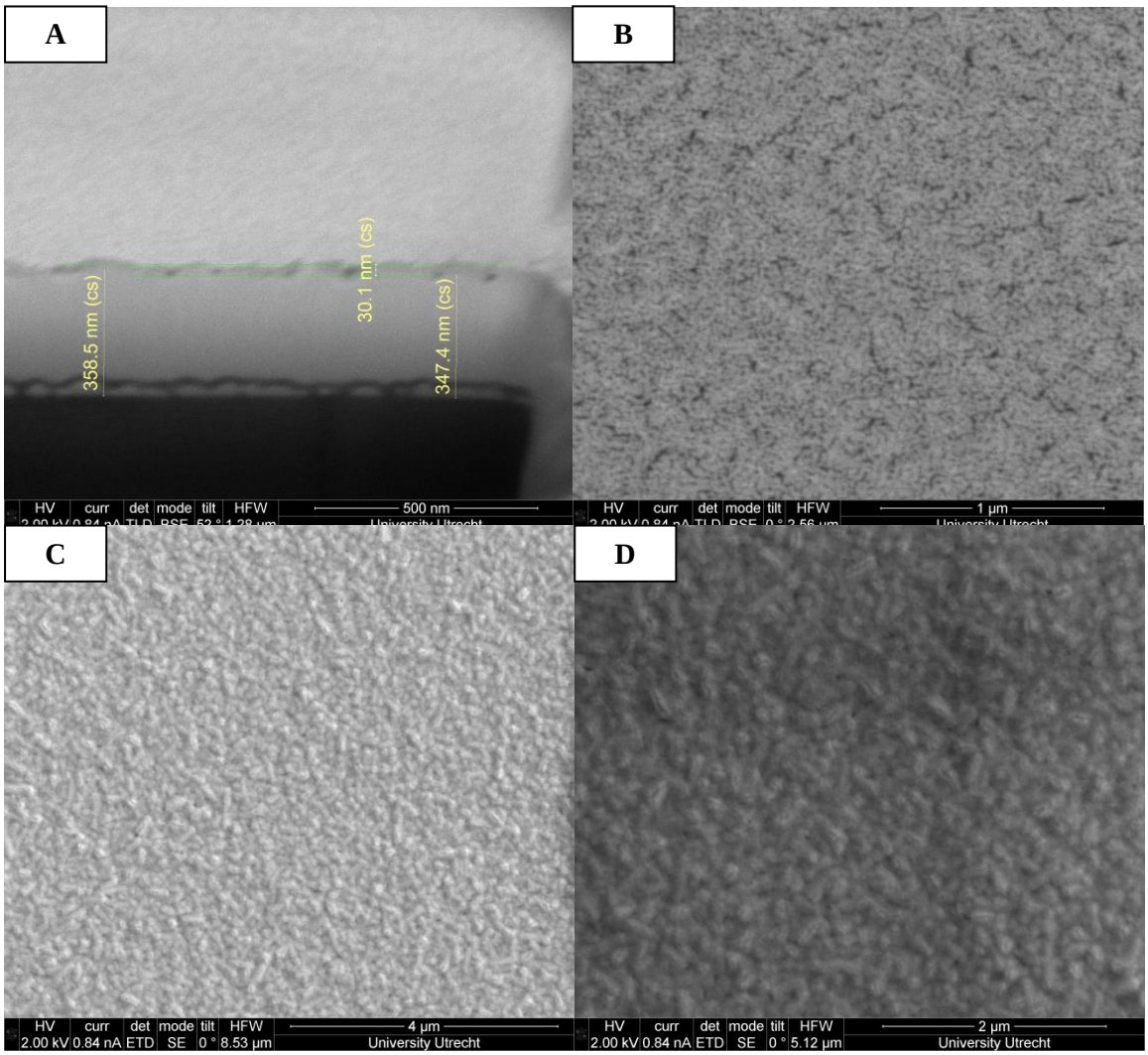

Figure 20 A-D) FIB-SEM images of NiO and Co_3O_4 on FTO. A-B) Cross-section and top view images of a single cycle coated NiO film. C-D) Top view images of a triple cycle coated Co_3O_4 film from which the thickness is assumed to be similair to that of NiO.

In figure 21, FIB-SEM images are shown for the same NiO sample on a glass substrate as used for the XRD analysis of figure 19. Cross-section image (A) shows that again porosity is present within the layer. The thickness of the layer is 104 nm which would suggest a layer growth of about 26 nm per cycle as compared to the 30 nm per cycle on the FTO substrate. Interestingly though, the porous cavities seem to be located near the glass substrate interface. This seems to support the statement made earlier where it was expected that multiple layer coating would partially cover the cavities. Unfortunately though, as is observed in both images (B) and (C) the NiO layer doesn't fully cover the substrate surface. (B) shows many sub-micron to micrometer sized particulates on the surface and in (C) partial coating of the surface is observed with large tens of micrometer sized voids. Interestingly, in the case of (B) a shadowing effect behind these particulates is observed in which the shadows all point in the same direction. This indicates that as the solution is injected on the substrate during spinning and the solution is spreading radially over the surface that narrow stripes behind such particulates are not covered by the solution and thus uncoated. The origin of such particulates could be due to either particles or crystallites present in the injected solution or surface contaminations. The first case is highly unlikely since a 0.45 µm filter is used before solution

injection and thus does not explain the presence of such large particulates. In the second case, it is also unlikely that so many particulate contaminations are due to dust deposition since both rigorous cleaning steps were employed as well as substrate covering with petri dishes before and after deposition and drying. However, a rigorous cleaning step was utilized as stated above with two prolonged ultrasonication steps. Considering that these glass substrates are very thin, 0.8 mm, and were precut with a glass cutter but not broken before sonication it is possible that these particulates originate from these precuts. In combination with the locally generated extreme pressures and temperatures during sonication, such particulates could travel over the substrate and become reannealed. To confirm this speculation, AFM measurements were performed on uncoated glass substrates which will be discussed shortly. Besides the presence of highly unwanted large particulates on the surface another problem was observed in image (C). This second problem is the partial coating of the glass substrate with the NiO layer. The most straightforward reason is due to the hydrophobicity of the glass surface and therefore the contact angle that a droplet of the precursor solution will exhibit. High contact angles indicate bad solvent spreading over the surface which would be associated with bad coating. Unfortunately, no contact angle measurements could be performed. However, 20 minute UV-Ozone treatments were performed to increase the hydrophilicity of the surface but might not have been sufficient. This partial coating is highly unwanted and options to improve the coating would be to either use a different deposition technique, preferably not based on sol-gel methodology such as the before mentioned PVD and CVD sputtering techniques or to increase the surface hydrophilicity. No FIB-SEM images for Co_3O_4 samples on the glass substrate are available and thus no conclusive remarks can be made on the morphology and coating quality of such a film. However, based on the intrinsic irregular roughness of the glass substrate surface due to the particulates it is reasonable to assume that the Co_3O_4 film suffers from similar partial coating profiles on the glass substrate.

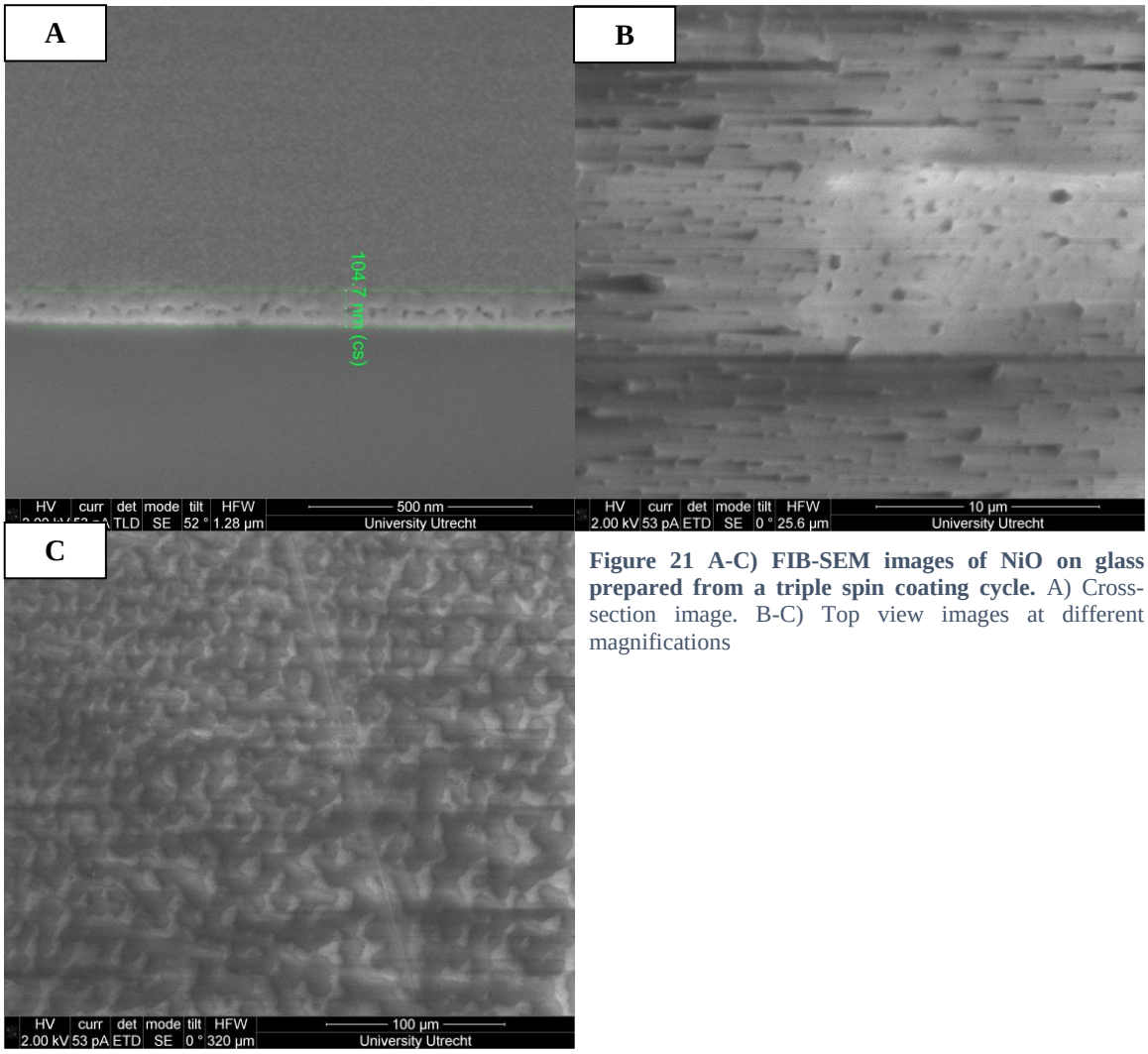

Figure 21 A-C) FIB-SEM images of NiO on glass prepared from a triple spin coating cycle. A) Cross-section image. B-C) Top view images at different magnifications

In figure 22 the AFM pictures are presented for an uncoated and cleaned glass substrate before (A) and after (C) the same thermal treatment that the HTM coated glass substrates experience at 500 °C with the corresponding height profiles of certain regions on the surface in (B) and (D). For both substrates a 100µm x 100µm area is profiled. For both samples a lot of particulates are present on the cleaned surfaces that are on the order of 100 nm in height and a couple of µm in radius. For the oven annealed sample one very large particulate was observed which was so high and broad that it distorted the tapping mode of the AFM probe in the near region. The AFM images seem to confirm that the microscopic glass slides used as substrates within this research are unsuitable for thin film deposition where clean surfaces are highly important for the coating quality.

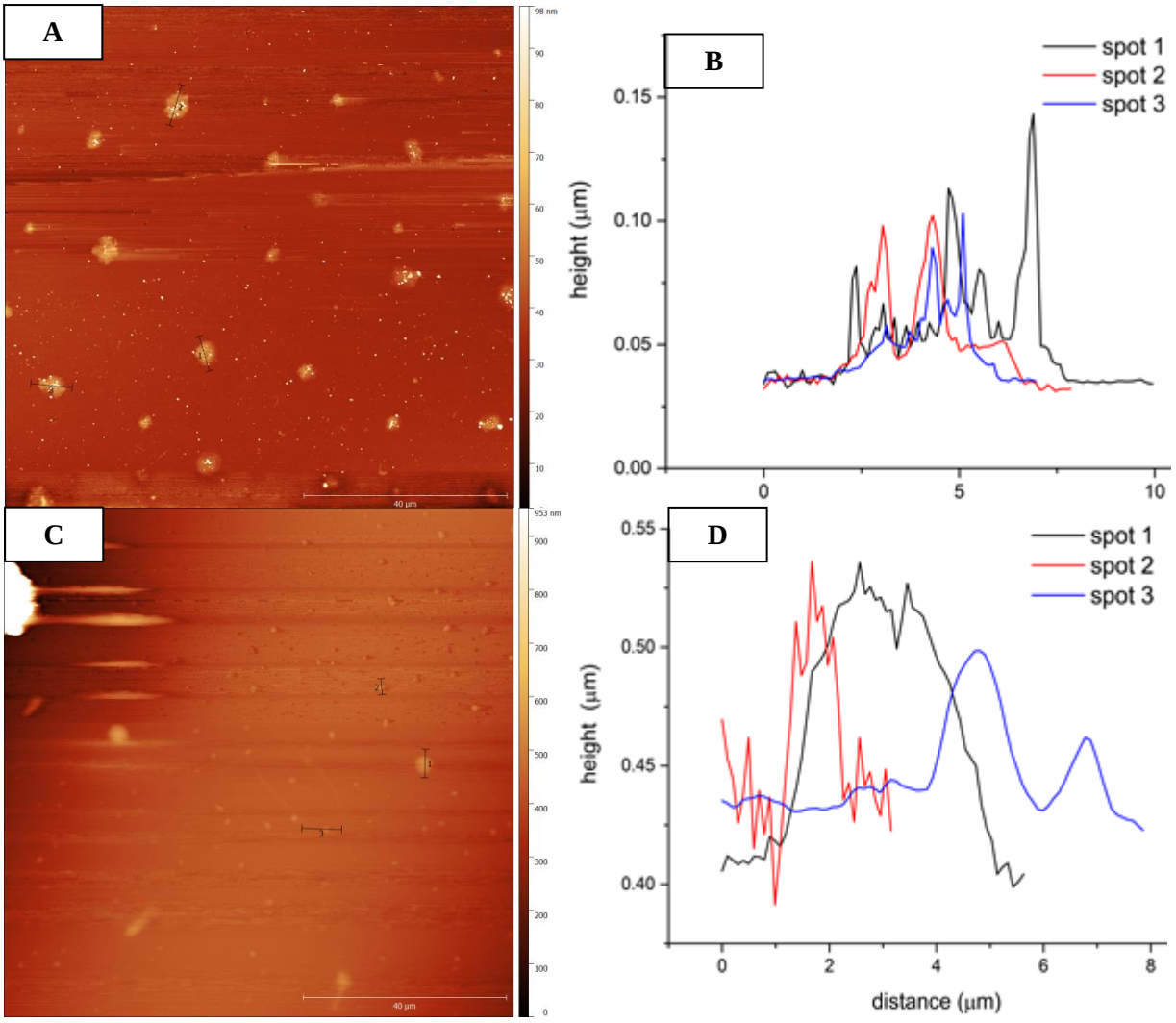

Figure 22 A-D) AFM images and the corresponding height profiles of uncoated glass substrates. A) AFM image of a glass slide after the cleaning procedure. The height profiles of the three black lines drawn through the particulates are shown in B). In C) the AFM image of a glass slide is shown which underwent both the cleaning steps and the thermal annealing at 500 °C for 3 hours. The height profiles of the three black lines drawn through the particulates are shown in D).

So far the crystallinity of the NiO and Co_3O_4 layers have been investigated as well as the surface morphology under different conditions such as number of spin coating cycles and substrate material. To complement the XRD and FIB-SEM results, UV-Vis is used to confirm the optical absorbance characteristics of NiO and Co_3O_4 thin films. As mentioned in section 2.4.2, the analysis of thin film UV-Vis spectra is often complicated due to so called interference fringes. These interference fringes are due to constructive and deconstructive combination of photons of a certain wavelength at a specified angle between the interfaces of one or more thin films and bulk layers such as air and glass with a change of refractive index at the interfaces.

In figure 23 a comparison is made between NiO samples coated on FTO and glass with the ethanol based solvent. Both NiO samples underwent two spin coating cycles from which the thickness is estimated to be 60 nm for NiO on FTO and 52 nm for NiO on glass based on the FIB-SEM results discussed earlier. The reason to use two spin coating cycles is to keep the HTM layer as thin as possible while still aiming to create a non-porous interface (cavities will remain within the film as observed with FIB-SEM). The two lines, blue for the NiO on FTO sample and red for the NiO on glass sample, show a few major differences in the absorbance. These major differences are visualized in the nearly linear region between 360-1000 nm for NiO on glass and the wave-like pattern observed for the blue line. Since FTO itself is also a thin film in the range of 200-400 nm thickness it complicates the interference pattern due to multiple thin film interfaces at which the constructive/destructive interference of light can occur. A theoretical calculation on the reflectance of a thin film on both a SiO_2 and FTO substrate is shown in appendix A based on the thin film reflective calculator from Filmetrics© [79]. For NiO a wide range of optical band gaps from approximately 3.5 to 4.0 eV have been reported for thin films [80],[81] which correspond to a range of respectively 354 nm to 310 nm at which the offset of absorption starts. For both NiO on glass and FTO the main increase of absorbance starts around 360 nm which is about 3.44 eV and corresponds to the optical band gap absorption processes. In the case of the FTO sample a shoulder around 340 nm is present, which is most likely due to interference fringes. However, it is also possible that the both the sharp and broad peaks observed between 340-1000 nm for both NiO films is due to the formation of a nickel silicate interface for NiO on glass and nickel doping in FTO. For the optical band gap values of NiO reported are based on Tauc plots. In the present case, the absorption coefficient would have to be calculated from the sum of absorption and reflection since no correction for reflection can be made here. Therefore the optical band gap calculated from the Tauc plot itself for these UV-Vis spectra might not correspond to the true optical band gap due to the presence of the reflection in the data. A discussion on the relevance of Tauc plots within experimental conditions of this research is given in appendix B.

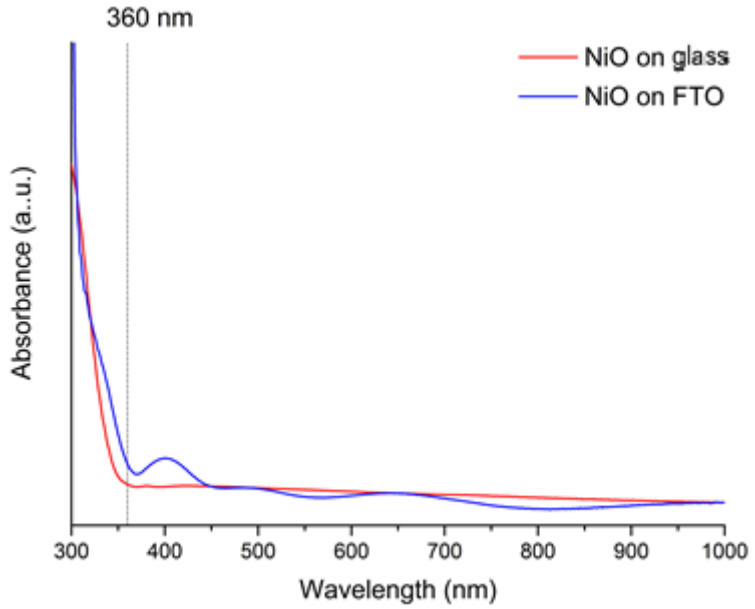

Figure 23 UV-Vis Absorbance spectra of NiO films on a glass and FTO substrate. Both films were prepared from a double spin coating cycle and are assumed to have a similair thickness.

In figure 24 the same comparison is made for Co_3O_4 coated on glass and FTO substrates from six spin coating cycles to achieve a similar expected thickness as for the NiO samples. The first interesting feature to note is that for the Co_3O_4 layer on FTO, nearly identical positions for the non-band gap peaks are observed as for the NiO layer on FTO in figure 23. This also seems to support that these observed peaks are most likely interference fringes instead of actual optical transitions due to Ni^{2+} or Co^{2+} doping of FTO. In the vertical lines the in literature reported values are given for the absorption offset of the two optical band gaps of Co_3O_4 at respectively 560 nm or 2.2 eV and 830 nm or 1.5 eV [47]–[49]. These values seem to correspond well to what is observed for both Co_3O_4 samples in the figure 24. The steep absorbance increase observed for both samples around 300-350 nm with emphasis on the FTO sample is most likely due to insufficient back ground correction of the uncoated glass and FTO substrates due to a change of refractive index interfaces thus changing also reflective properties.

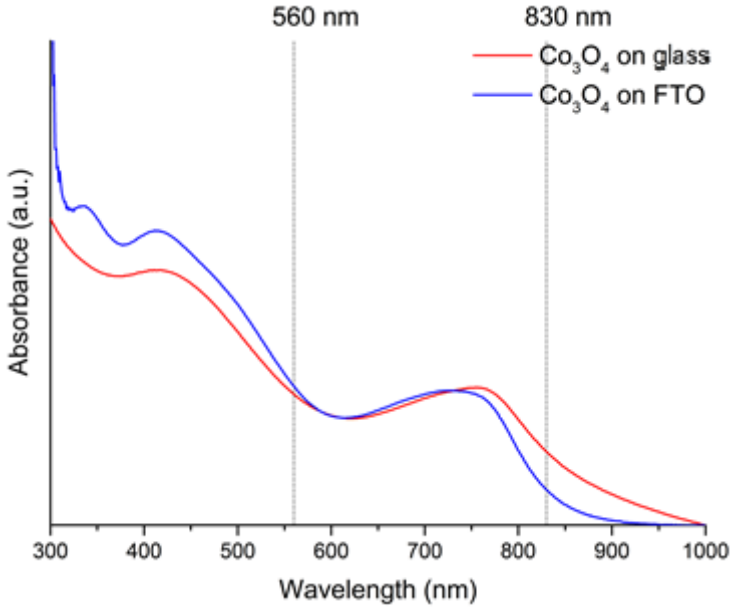

Figure 24 UV-Vis Absorbance spectra of Co_3O_4 films on a glass and FTO substrate. Both films were prepared from a double spin coating cycle and are assumed to have a similair thickness.

3.1.2 Fabrication of Co^{2+} Doped NiO Thin Films on Glass Substrate

Crystalline undoped NiO and Co_3O_4 films have been deposited on both FTO and glass substrates. However, undoped NiO suffers from a low charge carrier conductivity due to its wide band gap which limits its use for highly efficient PV devices [41]. Therefore in the current section, the fabrication of the Co^{2+} doped NiO films will be discussed on the glass substrate and compared with the undoped NiO and Co_3O_4. The choice for glass as the deposition substrate is to improve the Co^{2+} doped NiO signal obtained with XRD and UV-Vis and therefore remove the troublesome FTO background signal. Furthermore, the glass coated metal oxide substrates will be coated with $MAPbI_3$ further one and probed with PL and TAS.

In figure 25 x-ray diffractograms of samples NiO, 1%, 5%, 10% Co and Co_3O_4 are shown as measured with a Cu Kα source and in figure 26 those of 0.1% Co and 0.5% Co as measured with a Co Kα source. It is clear that for these three highly doped Co samples the NiO crystal structure is preserved. No reflections belonging to the crystalline Co_3O_4 are present in any of the diffractograms. Caution should be used as to the sensitivity of the XRD setup. Since these films are prepared from four spin coating cycles they are only 104 nm thick by approximation. The presence of a separate crystalline Co_3O_4 phase, be it in the form of isolated islands/particles or a thin layer, could be too small in terms of vol.% to be detected above the noise signal of the glass substrate. Grazing incidence XRD would significantly increase the signal from the surface and would therefore give a better indication of the absence or presence of Co_3O_4, CoO or any other crystalline phase beside NiO in the Co doped NiO.

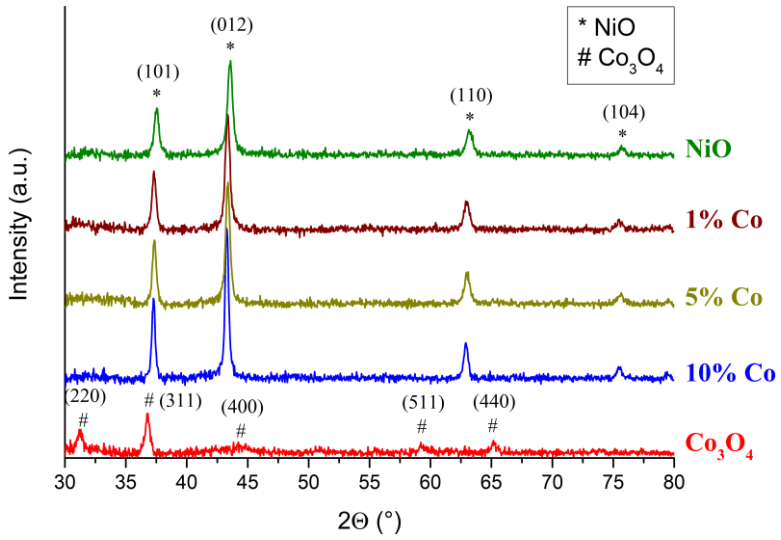

Figure 25 XRD of samples NiO, 1%, 5%, 10% Co and Co_3O_4 measured with a Cu Kα source.
The NiO and Co_3O_4 reflections are given with respectively the * and # symbols.

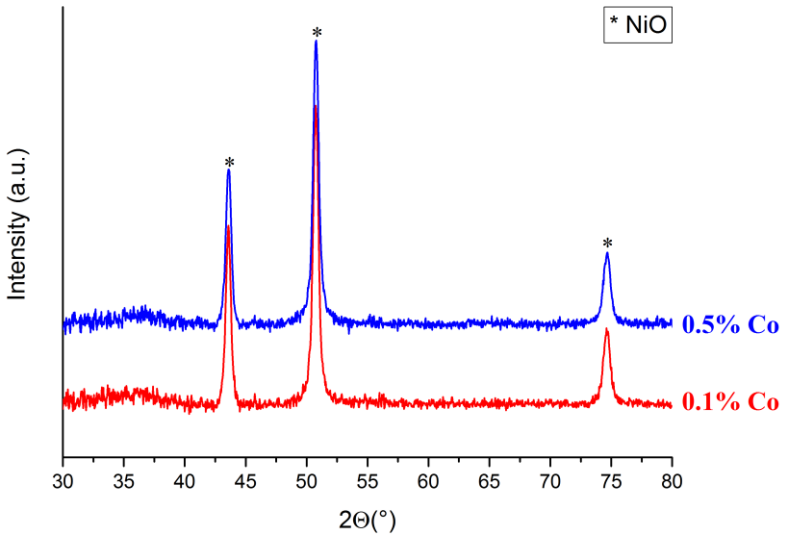

Figure 26 XRD of samples 0.1% Co and 0.5% Co measured with a Co Kα source. The reflections of NiO are given with the * symbol.

The crystal structure of NiO follows the fcc cubic rock salt structure. Therefore changes in the unit cell parameters and crystallite size can easily be accessed using equations 8b,c which are based on Bragg's law [41], [82] upon introduction of Co^{2+}. The shift of the (012) reflection of cubic NiO, crystallite sizes and the corresponding change in unit cell parameter a_0 are shown in figures 27 and 28 and table 6. It is evident that upon introduction of the Co^{2+} dopant the (012) reflection shifts to lower diffraction angles and thus to larger unit cell parameter values. Sharma *et al.*, reported that this increase might be due to the larger ionic radii of Co^{2+}, 0.72 Å, versus that of Ni^{2+} of 0.69 Å [41]. They observed a maximum increase in unit cell parameters for 0.1% Co doping and then a slight decrease as higher doping values up to 15% were claimed. In the present case figure 29 also shows the maximum increase for 0.1% doping and then a decrease towards 5% with a sudden jump again to 10% Co in the precursor solution. The experimental conditions of the two situations are completely different however. Whereas these films are produced with a spin coating technique, metal acetate precursors and a final thermal treatment at 500 °C, Sharma used spray-pyrolysis, metal chloride precursors and annealed the films at 300 °C. These different experimental conditions can have significant effect on the film morphology, crystallinity and actual amount of Co doping into the crystal lattice of NiO. The unit cell parameter, a_0, increases from 4.639 Å to a maximum of 4.668 Å for 0.1% Co then decreases a bit and finally goes back up to 4.668 Å for 10% Co. Furthermore, the crystallite size of NiO increases from 173 Å up to a maximum of 254 Å for 10% Co which is an increase of 47%. There seems to be a correlation between the change of the unit cell parameters and the change of the crystallite size. It has been proposed that at low amounts of Co doping (<1%) the Co^{2+} ions will replace Ni^{2+} ions in the crystal lattice and as mentioned earlier with the larger ionic radius of Co^{2+} this leads to an increase of the unit cell parameter [41]. At higher amounts of Co dopant, Co^{2+} might also occupy the vacant octahedral holes which are present due to Ni^{2+} vacancies. By occupying these vacant sites, the crystallinity should be improved and lead to more compact unit cells. Interesting to note is the increase of crystallite size upon doping. Larger crystallite sizes mean lower amount of crystallite boundaries. Crystallite boundaries are known for having many defects due to kinks, step sites, terraces, etc. which can act as trap states and recombination centres for free charge carriers and thus reducing PCE efficiency. Therefore the increase of crystallite size upon doping with Co^{2+} is a beneficial attribute.

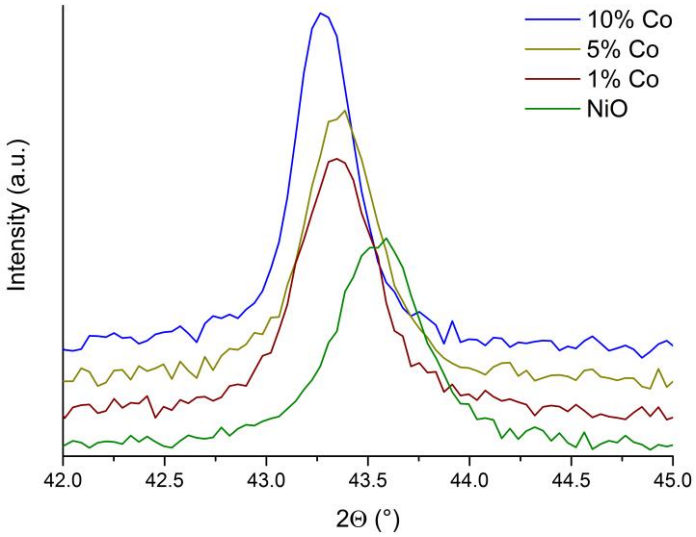

Figure 27 The shift of the (012) reflection towards lower angles upon Co^{2+} doping of the NiO cubic crystal structure. The (012) reflection of the samples 1%, 5%, 10% Co from figure 24 are shown.

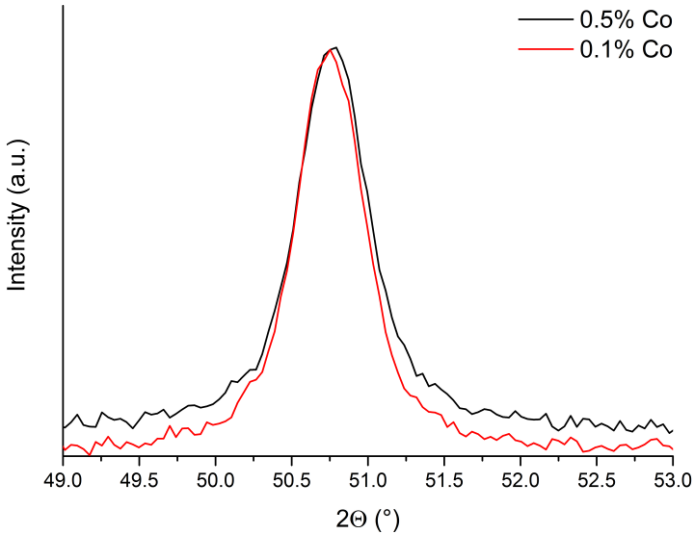

Figure 28 The shift of the (012) reflection towards lower angles upon Co^{2+} doping of the NiO cubic crystal structure. The (012) reflection of the samples 0.1% Co and 0.5% Co from figure 25 are shown.

Table 6 Summary of the change of the unit cell parameter for the NiO cubic crystal structure and crystallite size upon doping with Co^{2+}. Calculated from the shift of the (012) reflection in figures 27 and 28 using equations 8b and 8c

Sample name	(012) reflection 2θ (°)	Unit cell parameter (Å)	Crystallite size (Å)
NiO	43.57	4.639	173
0.1% Co	50.74*	4.668	215
0.5% Co	50.75*	4.667	200
1% Co	43.33	4.664	188
5% Co	43.38	4.659	205
10% Co	43.29	4.668	254

** Co Kα x-ray source*

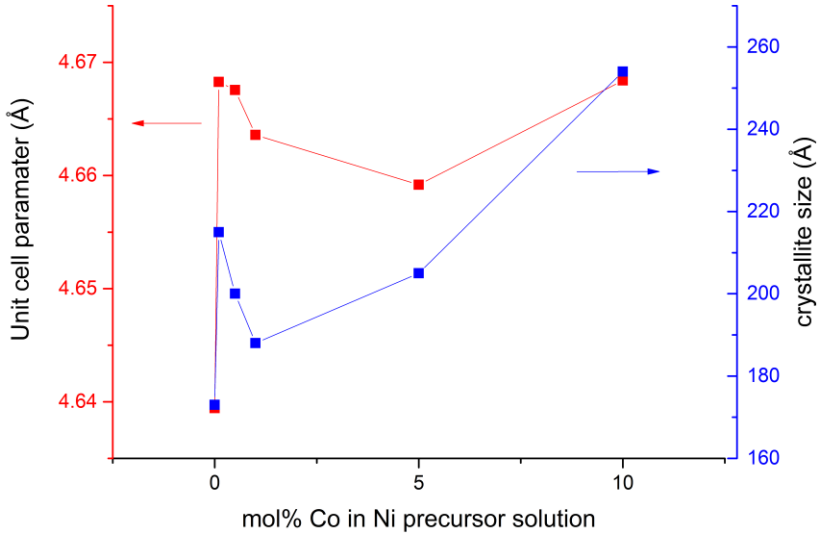

Figure 29 The unit cell parameter and crystallite size values from table 6 for the undoped and Co^{2+} doped NiO films. The unit cell parameter values are shown in red belonging to the left y-axis and the crystallite sizes in blue from the right x-axis.

In the case of surface morphology studies, no FIB-SEM or AFM images are available for the % Co doped NiO layers on the glass slide substrates. The only FIB-SEM images available are of undoped NiO on a glass slide substrate as shown in figure 21 above. Therefore it is unknown whether the same non-uniform layers are obtained for % Co doped NiO and Co_3O_4 deposition on the glass substrates.

Besides the investigation on the crystal structure changes of NiO upon doping with Co^{2+}, the changes in absorbance features with UV-Vis spectroscopy can provide additional information about new optical transitions to the Co^{2+} dopant. Figure 30 shows the UV-Vis absorbance spectra for the NiO and Co_3O_4 samples as already shown before in figures 22 and 23 and the x% Co samples. The vertical lines indicate the optical band gap values of NiO and Co_3O_4 thin films as mentioned earlier from literature converted to wavelength units (nm). In the case of the low mol% Co samples 0.1 – 1% Co no apparent changes are visible from this UV-Vis spectra. For 5 and 10% Co however major differences occur in the absorbance from 360 nm to about 700-800 nm. At such high concentrations of Co^{2+} a considerable amount of Co^{2+} ions could be incorporated into the NiO structure or form separate phases such as Co_3O_4 or CoO which bring about optical transitions at different energies. In the case of the spinel Co_3O_4 the

two optical band gaps around 830 nm and 560 nm correspond respectively to a $t_{2g}(Co^{3+}) \rightarrow t_2(Co^{2+})$ charge transfer transition and the $p(O^{2-}) \rightarrow t_2(Co^{2+})$ charge transfer transition [83]. Therefore, this new absorbance feature observed for the % Co samples from 360 nm to longer wavelengths could be a p-d charge transfer transition between O^{2-} 2p and Co^{2+} 3d states. Co^{2+} is in a tetrahedral coordination within Co_3O_4 however in the NiO fcc cubic system it would be in an octahedral position. Therefore the energy values of the transition might shift and the charge transfer transition is now $p(O^{2-}) \rightarrow e_g(Co^{2+})$. To take a better look at these changes, the undoped NiO UV-Vis spectra is subtracted from the % Co doped NiO samples so that only changes due to the presence of the Co^{2+} dopant are made visible.

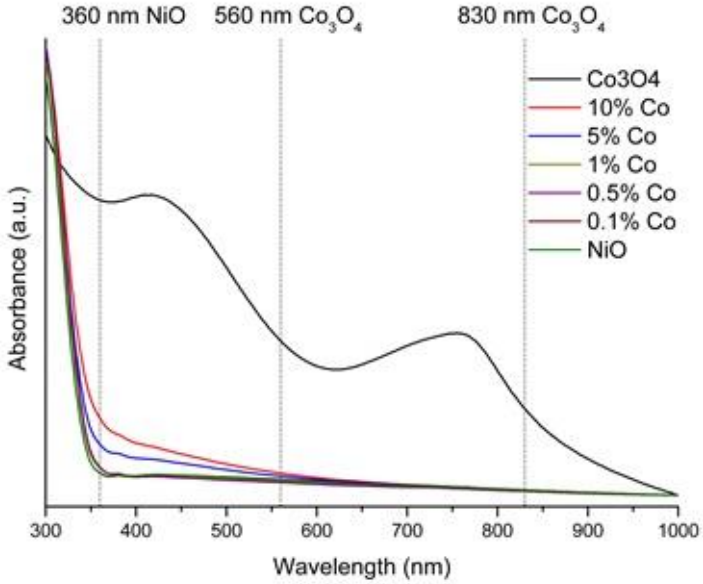

Figure 30 UV-Vis Absorbance spectra of the NiO, Co_3O_4 and the x% Co films on glass substrates. The reported band gap values of NiO and Co_3O_4 are shown in the vertical dashed lines corresponding to respectively 3.4 eV, 2.2 eV and 1.5 eV for 360 nm, 560 nm and 830 nm.

This subtraction of the NiO UV-Vis absorbance is shown in figure 31. The horizontal dashed line indicates where the absorbance equals 0. For the 0.1% Co sample, the change of absorbance is almost nonexistent. Considering the low amount of Co^{2+} in the precursor solution and therefore perhaps an even lower amount of Co^{2+} in the NiO lattice this is not very surprising. The profiles from 0.5% Co and 1% Co are interesting. Before the band gap offset of NiO itself around 360 nm they observe a negative absorbance with respect to undoped NiO. This could indicate that these films are less scattering and therefore might have a less rough surface which might be correlated to the increase of crystallite size. This effect seems to be stronger for 0.5% Co but care has to be taken because in this same region also the optical charge transfer transitions lie for $p(O^{2-}) \rightarrow e_g(Co^{2+})$ meaning that especially for 1% Co the negative absorbance of a less scattering surface and absorption of the optical transition overlap. For 5% and 10% Co there is a major increase of absorbance before the NiO band gap offset at 360 nm. This most likely is due to the $p(O^{2-}) \rightarrow e_g (Co^{2+})$ charge transfer assuming that Co^{2+} is at an octahedral position in the NiO lattice. It might also indicate the presence of a $Co^{3+} \rightarrow Co^{2+}$ charge transfer transition be it in the form of Co_3O_4 or partial oxidation of the Co^{2+} dopant to Co^{3+} in the NiO crystal lattice at such high doping levels. Interesting to note is the additional absorbance peak around 340 nm. It could indicate an increase of the extinction coefficient of the NiO film upon doping. That implies that these films could be thicker than the undoped NiO film. However for the Co^{2+} doped samples the same number of spin coating

steps are used and the concentration of the Ni^{2+} precursor in the solution is less than that of the undoped NiO layer. Another situation could be better coating of the substrate surface and that therefore effectively more NiO material is present within the probed area without changing film thickness since for undoped NiO a partial coating on glass was observed. A third explanation would be an increase of the crystalline nature of the NiO films. As mentioned earlier, Co^{2+} dopants could occupy the vacant octahedral positions which could lead to a more crystalline film. Without knowledge on the surface morphology and coating of these films on the glass substrate it is not possible though to conclude the origin of this increase. Finally, the changes observed are marginal and might as well just fall within the uncertainty of the experiment.

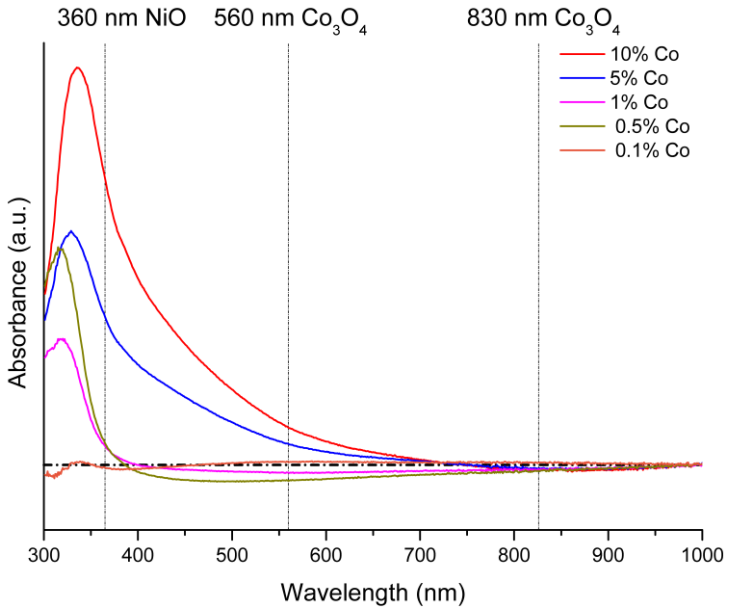

Figure 31 UV-Vis Absorbance spectra based on the subtraction of the undoped NiO absorbance from the x% Co samples to visualize the effect of Co^{2+} dopant. The reported band gap values of NiO and Co_3O_4 are shown in the vertical dashed lines corresponding to respectively 3.4 eV, 2.2 eV and 1.5 eV for 360 nm, 560 nm and 830 nm.

The 0.1-10% Co^{2+} doped NiO films on glass slides have been characterized with XRD and UV-Vis and compared to the undoped NiO and Co_3O_4 films. For the 0.1-10% % Co samples the NiO crystalline cubic phase is retained even upon high concentrations of Co^{2+} present in the precursor solution and no presence of any other crystalline phase is detected. Using the Scherrer equation and an adaption of Bragg's law, the crystallite size and change in unit cell parameter were determined. Both quantities increase for the % Co doped samples compared to the undoped NiO which indicate that Co^{2+} has successfully been doped into the crystal structure. UV-Vis analysis showed indeed that for the highly doped 5 and 10% Co samples charge transfer transitions between O^{2-} and Co^{2+} appear. For the samples 0.5-10% Co an interesting increase of absorbance after the band gap offset of NiO is observed which might indicate a thicker film, better substrate coating or increased film crystallinity.

3.2 Part II: Thin Film Fabrication of MAPbI3

In this section part II of the aim will be discussed. Thin films of the hybrid perovskite $MAPbI_3$ have been spin coated on a variety of substrates namely FTO, glass and x% Co doped NiO / Co_3O_4 coated glass. In section 2.3.2 three different deposition methods of $MAPbI_3$ involving spin coating were discussed. For this research, the two-step deposition method is utilized and the motivation for this deposition method is explained in appendix C.

3.2.2 Two-step Deposition of $MAPbI_3$ on Different Substrates

To confirm that the two-step deposition method could be used to successfully fabricate the hybrid perovskite, $MAPbI_3$, XRD analysis was performed. For the fabrication of highly efficient $MAPbI_3$ PV it is important that both MAI and PbI_2 have fully reacted towards a highly crystalline $MAPbI_3$ film. The XRD results of identically coated $MAPbI_3$ films on glass and FTO substrates are shown in figure 32 together with reference MAI powder XRD and PbI_2 thin film on glass. First of all, for both $MAPbI_3$ films no evidence of the presence of crystalline MAI is present. In the case of PbI_2 it is not that simple though. The (002), (003) and (004) reflections of cubic PbI_2 are absent for both $MAPbI_3$ films, however around 14.9 ° for both films a small peak appears that overlaps with the (001) of PbI_2. After careful analysis this peak seems to be the Kβ reflection of the (110),(002) doublet of the orthorhombic $MAPbI_3$ structure at roughly 16.4 °. The presence of this Kβ reflection is emphasized by the presence of Kβ reflections for both the PbI_2 film and MAI powder as marked in the diffractograms. Furthermore, theoretical calculations on the position of the Kβ reflection were done using Bragg's equation 8a and are presented in table 7 together with the experimentally found reflection positions. The exact position of the maximum of each reflection was calculated with an asymmetric, double sigmoidal, single peak fitting function.

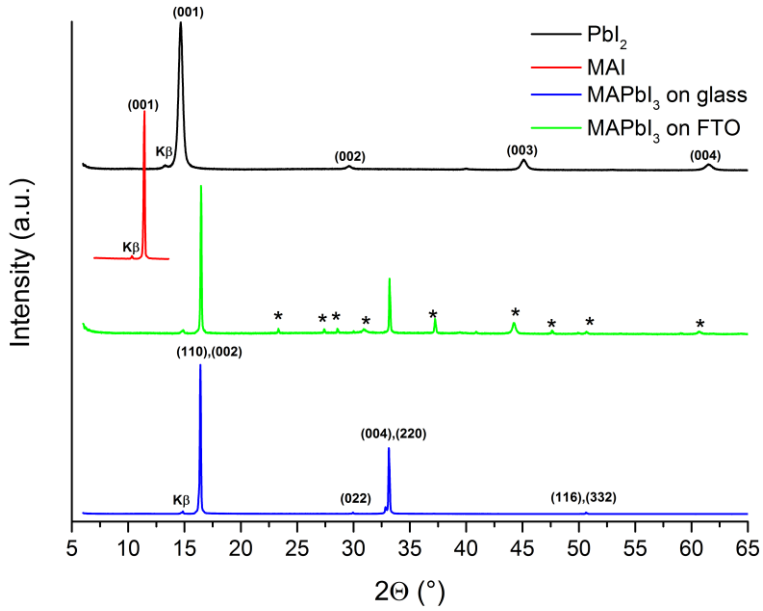

Figure 32 XRD results of thin films of PbI_2 (black) and $MAPbI_3$ on glass (blue), a thin film of $MAPbI_3$ on FTO (green) and a powder sample of MAI (red). The * symbol indicates the position of visible FTO substrate reflections.

Table 7 Summary of the Kα and both calculated and experimantlly obtained Kβ (110),(002) doublet reflections. Peak positions were found using an asymmetric double sigmoidal single peak fitting function.

Sample name	2θ Kα position (°)	Calculated 2θ Kβ position (°)	Experimental 2θ Kβ position (°)
PbI_2	14.65	13.26	13.12
MAI	11.43	10.35	10.36
$MAPbI_3$ on glass	16.36	14.81	14.88
$MAPbI_3$ on FTO	16.42	14.86	14.85

In figure 33 the FIB-SEM images of the $MAPbI_3$ on FTO are shown. As can be seen in both images (A) and (B) the surface of the $MAPbI_3$ film seems to be very smooth and pinhole free. Especially the pinhole free nature of the film is very important. Furthermore, the grain sizes observed are very large on the order of hundreds of nm towards a µm which is also very beneficial. The lower the amount of grain boundaries, the lower the density of surface defects due to step and kink sites is, which will lower the chance of recombination events at the surface due to charge carrier trapping. Unfortunately, no SEM images of the $MAPbI_3$ are available on a glass substrate. In appendix C the attempt of making a cross-section on a $MAPbI_3$ coating with the FIB apparatus is shown.

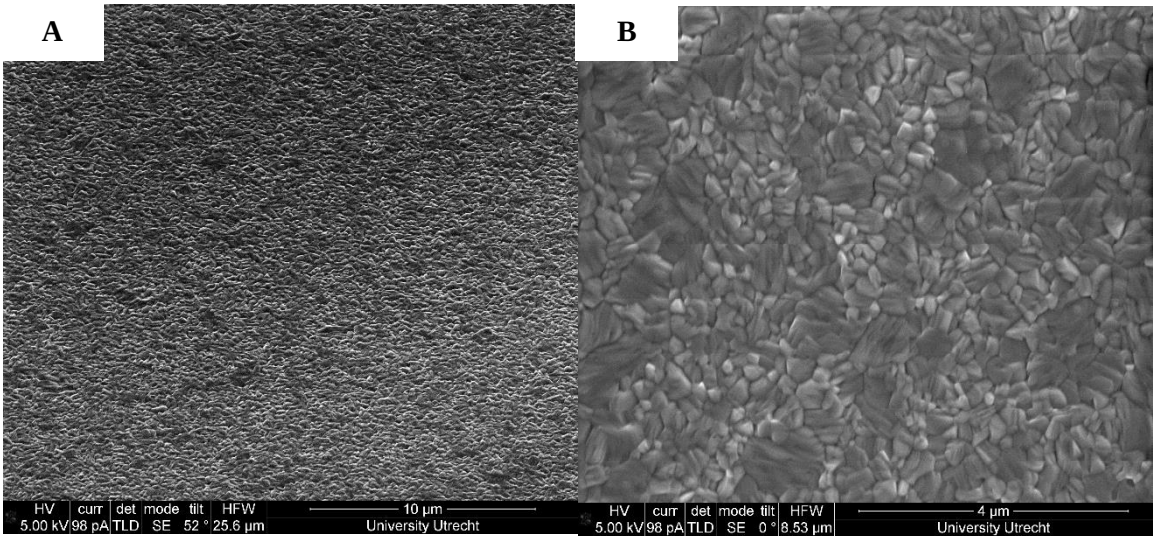

Figure 33 A-B) Top view FIB-SEM images of a $MAPbI_3$ film deposited on FTO using the two-step deposition method at two different magnifications.

As mentioned above no FIB-SEM images of the $MAPbI_3$ on the glass substrate are available. From the FIB-SEM images of NiO on glass the partial coating was observed. This partial coating is expected to be partially due to the presence of large particulates on the surface of the glass substrate before coating and due to the likely bad wetting of the surface with the precursor solution. For the two-step coating of $MAPbI_3$ first a layer of PbI_2 is coated from a polar DMF solution. Therefore, purely based on substrate hydrophilicity the polar DMF solvent is expected to also show bad wetting properties. To visualize the differences of the $MAPbI_3$ film on the different substrates, photographic images are shown in figure 34 for both $MAPbI_3$ on FTO (A) and $MAPbI_3$ on glass (B). The $MAPbI_3$ on FTO seems to be highly

uniform and very reflective which corresponds to the smooth film seen with the SEM. For the $MAPbI_3$ film on glass a more turbulent and hence scattering surface is observed. This scattering could be due to a rougher surface or a partial coating with void dimensions close to the wavelength of light. Therefore, FIB-SEM would be necessary to confirm the type of coating that $MAPbI_3$ exhibits on the glass substrate.

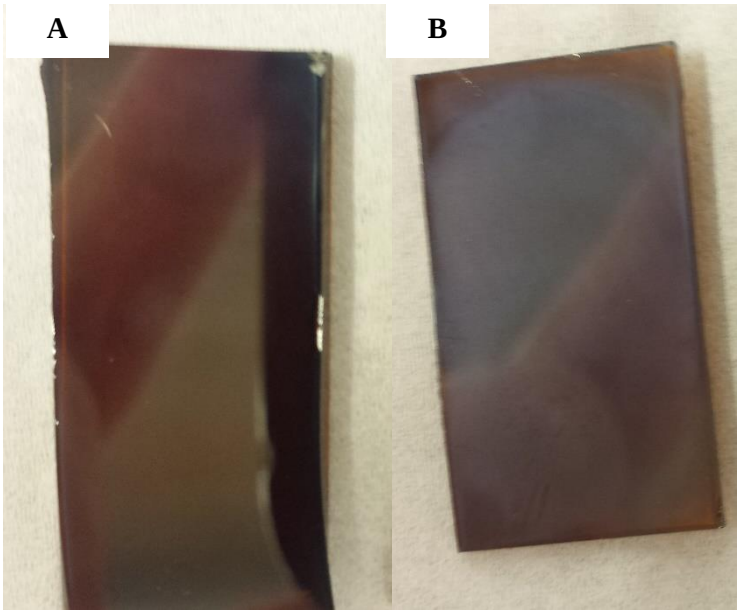

Figure 34 A-B) Photographic images of the $MAPbI_3$ film on different substrates. A) The highly reflective and semi-transparent coating of $MAPbI_3$ on FTO. B) The scattering coating of $MAPbI_3$ on glass

Both to probe the origin of the scattering $MAPbI_3$ film on glass and to confirm the $MAPbI_3$ optical characteristics, UV-Vis spectra are presented in figure 35. The samples $MAPbI_3$ on FTO and glass substrates are shown. Unexpectedly, the two spectra are very similar; between 500-780 nm there are practically no differences. Below 500 nm a second $MAPbI_3$ band gap reportedly originates from a deeper lying valence band (VB2) with an electronic transition to the same CB as that of the 1.57 eV reported band gap of $MAPbI_3$ [84]. The absorbance near the band gap seems to be slightly higher which would indicate a higher probability of absorption in this region. This could mean a higher degree of crystallinity, so better band forming, or thicker films. However, no change of absorbance at the main band gap of 1.57 eV is observed between the two samples so the origin is not yet understood. Also, from the photographic images a difference in the reflectivity of the surface was observed yet again no difference in band gap absorption is observed or clear scattering events. For the scattering $MAPbI_3$ film on glass either lower intensity of the band gap absorption is expected due to less material present within the probed volume or a higher degree of scattering in the visible region. The first situation is unlikely considering that the absorption intensity around 780 nm is identical. Scattering of the film could be the reason if the $MAPbI_3$ film is rougher on the glass substrate compared to FTO. However, no SEM images are available for the $MAPbI_3$ film on glass to support this statement.

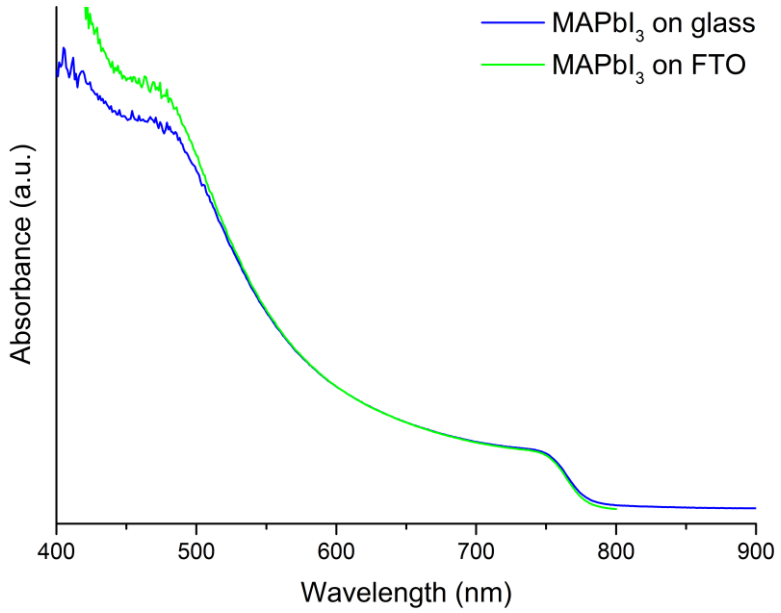

Figure 35 UV-Vis Absorbance spectra of the $MAPbI_3$ films coated on FTO and glass substrates. The samples shown here are the same as those shown in the photographic images in figure 34.

Only UV-Vis absorbance data is available for the coating of $MAPbI_3$ on the HTM films. In figure 36, the UV-Vis absorbance spectra are shown for the $MAPbI_3$ films coated on either glass substrate or the x% Co NiO and Co_3O_4 layers on glass. A first observation is made on the absorbance around 780 nm which is the band gap offset of $MAPbI_3$. For the $MAPbI_3$ layer on glass and the 0.1-10% Co layers the shape is identical. This seems to confirm that the morphology and/or the thickness of $MAPbI_3$ on both glass and these Co^{2+} doped NiO layers is nearly identical. For $MAPbI_3$ coated on Co_3O_4 a higher absorbance is to be expected considering that Co_3O_4 itself also has low energy band gaps such as the $t_{2g}(Co^{3+}) \rightarrow t_2(Co^{2+})$ charge transfer transition at 1.5 eV. However the shape of the band gap offset from $MAPbI_3$ on Co_3O_4 is similar to those of the Co^{2+} doped NiO samples. One sample is however considerably different in terms of the UV-Vis absorbance profile at 780 nm. The $MAPbI_3$ layer on NiO shows a very low increase of absorbance which might indicate for instance the formation of a very thin film of $MAPbI_3$ or a bad coating in which large areas of the substrate are not covered with $MAPbI_3$. From the FIB-SEM images it was observed that the NiO coating of the glass surface was partial. However no FIB-SEM images of the Co^{2+} doped NiO layers or Co_3O_4 layer on a glass substrate is present and therefore it is unclear if the bad $MAPbI_3$ coating on the NiO layer is due to the partial coating. Up to about 570 nm the relative absorbance profile of all samples is nearly identical until the increase of absorbance for the $MAPbI_3$ film on the metal oxide layers increases more than that for the film on glass. This effect cannot be due to the presence of PbI_2 though since the band gap and therefore the absorption offset of PbI_2 occurs at 2.4 eV or 520 nm. Perhaps this indicates better formation of the $MAPbI_3$ film either in terms of crystallization or surface coverage. Another possibility would be increased reflection due to the HTM thin film interface but for such events these are to be expected in terms of Gaussian type interference peaks. The 1.57 eV band gap offset of $MAPbI_3$ is nearly identical on all substrates except for the NiO layer which is significantly lower in the absorbance increase near the band gap offset. Thus the formation of $MAPbI_3$ seems to be nearly identical on the 0.1-10% Co and Co_3O_4 samples.

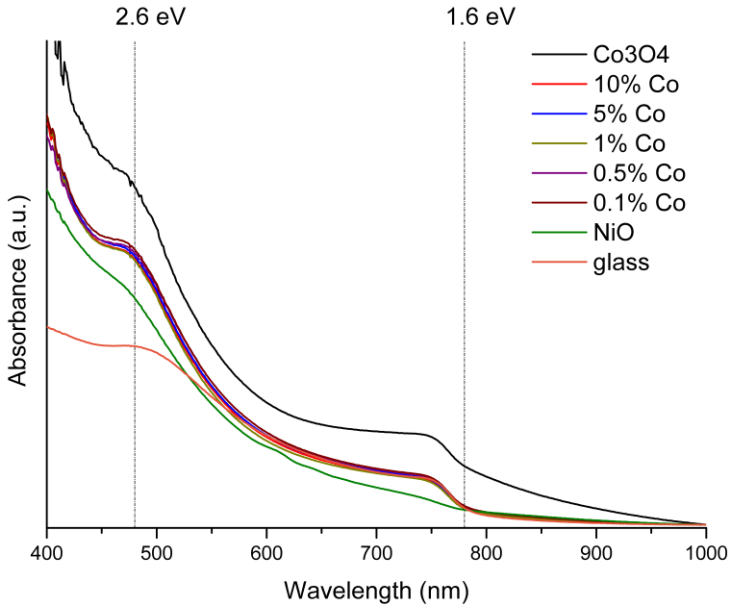

Figure 36 UV-VIS Absorbance spectra of $MAPbI_3$ coated on either one of the HTM coated glass substrates or on a glass substrate. The $MAPbI_3$ on glass sample is the same as shown in figure 35

3.3 Part III: Investigation of Photogenerated Charge Carrier Species

In this section the behavior of the photogenerated holes in the $MAPbI_3$ film and at the interface with the different HTM layers will be investigated. To do this, both steady-state PL and nanosecond TAS are utilized. With steady-state PL, the effectiveness of the hole injection from $MAPbI_3$ into the HTM layers will be probed. Time-resolved analysis of the photogenerated species is conducted with TAS.

3.3.1 Investigation of the Hole Injection from $MAPbI_3$ into the HTM

In figure 37, the PL intensity of $MAPbI_3$ on the different HTM layers and the reference glass substrate is shown. For every sample name two identical samples were prepared. A general trend in the peak maximum is visible in which the PL intensity decreases for $MAPbI_3$ going from NiO to 0.1-10% Co NiO and finally Co_3O_4 as HTM. The second major observation though is the position of the maximum of the peak. For the $MAPbI_3$ on glass sample the peak position lies at 778 nm, which is close to the reported value of 780 nm [18], [62], [73]. In the case of the glass and 0.1-10% Co NiO substrates there is a red shift in the position of the peak. The peak position for $MAPbI_3$ on glass is 778 nm and increases up to 783 nm for the $MAPbI_3$ layer on the 0.1-10% Co NiO substrates. The valence band gap difference between $MAPbI_3$ and Co_3O_4 is about 0.03 eV. If 778 nm corresponds to 1.59 eV, then the 0.03 eV shift would lead to a 1.56 eV recombination transition. The radiative recombination between the Co_3O_4 VB and $MAPbI_3$ CB would then occur at 792 nm. However, the ~ 5 nm red shift corresponds to only a 0.01 eV difference. The transition between the NiO VB and $MAPbI_3$ is about 0.2 eV lower than the intrinsic $MAPbI_3$ transition. Furthermore, radiative recombination processes from NiO VB to CB or Co_3O_4 VB to CB are expected to occur at 3+ eV and ~1.5 eV, respectively. The exact origin of the red shift is therefore hard to state and could be due to the instrumental setup itself. In the case of undoped NiO as the HTM a blue shift is observed towards 765 nm for the peak position. The blue shift could be due to the assistance of a phonon which cools the crystal lattice [85]. However, PL measurements from literature do not report such an event taking place when $MAPbI_3$ is coated on top of NiO [36], [46]. From FIB-SEM images on the NiO layer on both FTO and glass substrates it was evident that these layers were porous. Another possibility is therefore that $MAPbI_3$ during the deposition method infiltrates the porous network of NiO and that a quantum confined $MAPbI_3$ is obtained. Normally quantum confinement occurs when the de Broglie wavelength of the electron wave function is of a similar size as that of the diameter of a nanoparticle or quantum dot. For most materials this corresponds to particle sizes on the order of a few nm. The exact diameter of the porous network of these NiO thin films is hard to determine and the only indication is that of voids present in the FIB-SEM cross-section. The UV-VIS absorbance spectrum of $MAPbI_3$ coated on the NiO sample in figure 36 might correspond to this. Considering a two-step deposition method is used, PbI_2 might have infiltrated the porous NiO during the first deposition. Therefore, upon deposition of the second layer, MAI, a confined hybrid perovskite was formed. It is also possible that due to the partial coating of NiO on glass that the $MAPbI_3$ coating on the NiO substrate was partial as well. The $MAPbI_3$ could have then formed two-dimensional island or plates which undergo a quantum size effect visualized in the change of band gap.

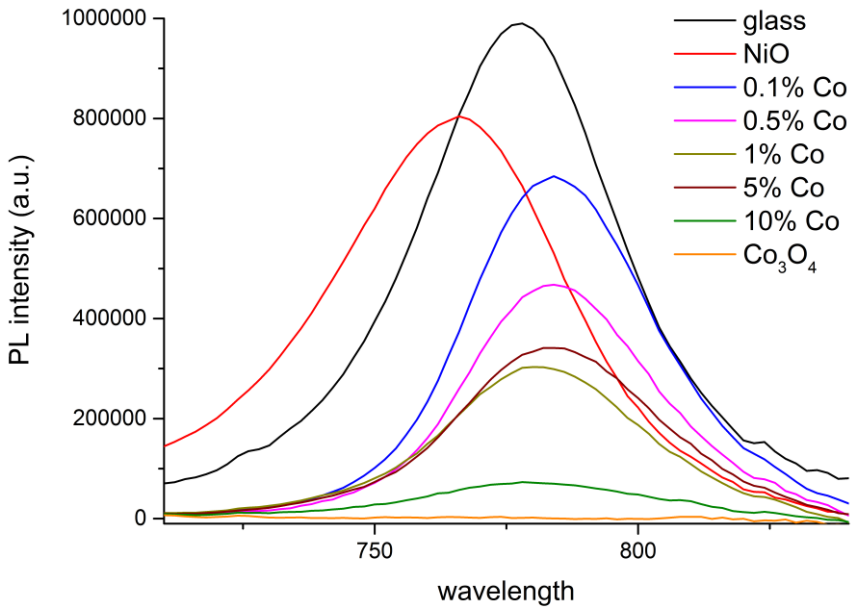

Figure 37 PL spectra of the $MAPbI_3$ coated samples from figure 35 of the different HTM and the glass substrates. The area underneath the peak is used to calculate the quenching efficiency from equation

The quenching of the PL signal from $MAPbI_3$ corresponds to the degree of hole injection into the HTM. This quenching is determined by taking the area under each peak where the beginning and end of the peak count as the background value for each sample and then using equation 10. A_{MO} is the area of the PL peak of $MAPbI_3$ coated on the nickel and cobalt metal oxides and A_{glass} is the area of the PL peak of the reference $MAPbI_3$ coated on glass substrate. The quenching efficiency results of the different HTM's on the PL signal of $MAPbI_3$ is shown in table 8. In figure 38 the QE of only the 0-10% Co^{2+} doped NiO is shown. The trend observed here follows that of figure 37 where the maximum intensity of the peak goes down from pure NiO as HTM to doped NiO and finally Co_3O_4. For the undoped NiO as HTM, QE values of 98% have already been reported by Wang, *et al.*, [46] whereas a value of 14.7% is achieved here. Even though Wang, *et al.*, also used microscopic glass substrates, they used both a thin dense layer of NiO deposited from spray-pyrolysis and a thick mesoporous NiO layer on top of that which was infiltrated with $MAPbI_3$. So not only is their surface coverage uniform, which isn't for the NiO layer on glass in this research, the thick mesoporous NiO layer allows for a significant interface area with $MAPbI_3$. Interestingly, the QE goes up as soon as the Co^{2+} dopant is introduced from 32.3% at 0.1% Co to 90.8% at 10% Co in the precursor solutions. The question arising here is whether this effect is due to actual doping effects of NiO and thereby changing the electronic structure of the layer and for instance the conductivity as well as the position of the Fermi level. Or is the coating of the surface improved by adding Co^{2+} to the precursor solution. Another possibility is due to phase segregation where Co_3O_4 is being formed since a high QE of 98.8% is found for Co_3O_4. Direct evidence for the presence of Co_3O_4 in the NiO layers was not witnessed with XRD for any of the samples and with UV-VIS. In figure 29 it was shown that indeed by adding Co^{2+} to the precursor solution, the unit cell parameter of the NiO cubic structure increases as well as crystallite size. Therefore it is plausible that at least part of the increase in QE is due to the doping of NiO with Co^{2+}. The effect of Co^{2+} on the surface morphology and coating profile of NiO is unknown since no FIB-SEM or AFM images are available only for 5% and 10% Co optical transition were clearly present between O^{2-} and Co^{2+}. However, in the end it is difficult to say which phenomena is to what extent responsible for the trend observed here and it could

be a combined effect of the possibilities presented. The QE of 98.8% for Co_3O_4 is higher than the QE of 98% reported for undoped NiO from literature. A QE value this high implies that the coating of Co_3O_4 on the glass substrate is much more uniform compared to the partial coating of NiO. However, care has to be taken with the QE value achieved here. Considering that the $MAPbI_3$ film had to be illuminated through the glass/HTM layers as discussed in the chapter 2 and that Co_3O_4 has a band gap of 1.5 eV it is possible that part of the incoming beam is attenuated and thus less $MAPbI_3$ species are excited. This in return could also lower the PL signal. But even if the incoming beam is attenuated to some degree, the high QE observed here is an indication that indeed Co_3O_4 is an interesting HTM candidate for $MAPbI_3$ PV. Finally it should be noted that the errors made are quite significant for most of the sample sets and especially for those achieving a low quenching efficiency.

Table 8 Summary of the quenching efficiency values calculated from two individual cells per sample name. The error of the QE for each sample is given as calculated from the QE of two individual cells per sample name.

Sample Name	Quenching Efficiency (%)
NiO	14.7 ± 9.4
0.1% Co	32.3 ± 15.4
0.5% Co	51.6 ± 12.3
1% Co	65.4 ± 3.3
5% Co	63.1 ± 2.1
10% Co	90.8 ± 2.8
Co3O4	98.8 ± 0.7

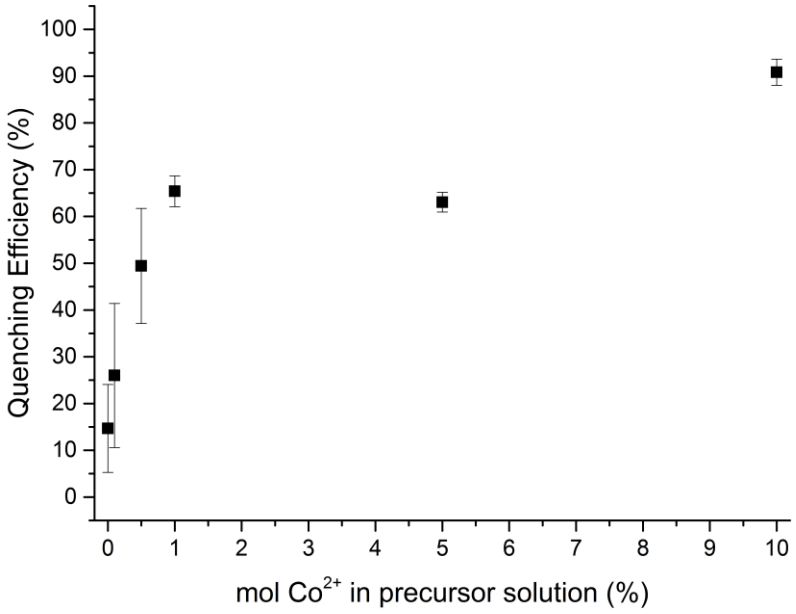

Figure 38 Graphic representation of the quenching efficiency as shown in table 8 for the x% Co^{2+} doped NiO samples. 0% mol Co^{2+} in the precursor solution refers to the NiO sample.

To investigate the attenuation of the incoming beam at 550 nm by the HTM layers, the absorbance of the HTM layers itself is plotted in figure 39 at 550 nm. The absolute values on the y-axis show that there is barely any attenuation at 550 nm by the undoped and Co doped NiO thin films. For Co_3O_4 there is indeed a higher absorbance at 550 nm due to the absorption of photons by its own band gap. However, to what extend this affects the QE value of 98.8% obtained in this research is unknown. Therefore, using a thin film dedicated PL setup in which illumination could be done directly through the $MAPbI_3$ / air interface would answer this problem. However, the information obtained solely from PL is not enough to predict how successful these metal oxides can be as HTM.

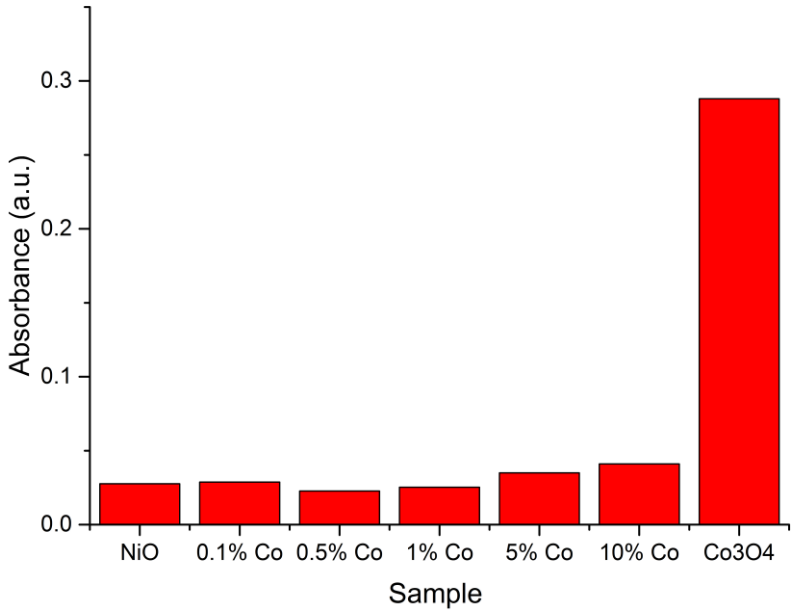

Figure 39 Absorbance values of the different HTM layers on glass substrates at the PL excitation wavelength of 550 nm based on figure 29. These values are given merely as an indication of the attenuation of the incoming beam due to absorption processes but care should be taken due to different angle of incidence compared to UV-VIS measurements.

3.3.2 Investigating the Charge Carriers in $MAPbI_3$: Influence of the HTM

Whereas PL is limited to the investigation of radiative recombination processes, in principle with transient absorption spectroscopy any type of recombination can be probed such as the non-radiative auger process. Therefore TAS can complement the information obtained from PL. For hybrid perovskite PV it has been reported that the charge injection from the hybrid perovskite into both the ETM and HTM layers can be probed due to a change in the ground-state bleach lifetime of the hybrid perovskite. However, these charge injection events take place at the sub-nanosecond timescale which is below the time resolution of the nanosecond transient absorption spectroscopy apparatus used for this research and therefore only the intrinsic ground-state bleach of the $MAPbI_3$ film can be investigated without the direct interaction with the HTM layers. TAS measurements were done on the same $MAPbI_3$ samples measured with PL.

In figure 40 the TAS spectra and kinetic plot are shown for the reference $MAPbI_3$ film coated on a glass substrate. The fundamental wavelength of the laser is 1064 nm and the second harmonics at 355 nm is used to excite the species. Signals belonging to the third harmonics at 532 nm and a degeneracy point at 710 nm are also present but omitted from the spectra for visualization. Below 500 nm the spectra becomes too noisy and is not shown. At 760 nm the ground-state bleach of $MAPbI_3$ occurs. At 0 ns the ground-state bleach starts to rise and reaches its minimum around 1 ns later. Most of the ground-state bleach intensity has already decayed within 5 ns as portrayed by the pink line. For the 50 ns and 1 µs lines no ground-state bleach intensity is left. On the right side the kinetic profile derived from the spectral data at 760 nm is plotted. This kinetic profile follows the decay of the signal over time at a single wavelength. The kinetic profile is fitted with equation 11 starting at the minimum peak height from which point onwards the decay begins. This double exponential decay fitting provides two lifetime values, τ_1 and τ_2. The fastest decay corresponding to the lowest lifetime, τ_1, is 1.8 ns with an error of 4.5% for this sample. For the second sample this value is 1.4 ns with an error of 4.0%. The second lifetime values, τ_2, are 77.6 ns for both $MAPbI_3$ on glass samples with higher errors of 10.1 and 17.4%. The function used to fit the data from equation 11 also shows two dimensionless weighting factors for the two exponential functions, A_1 and A_2. It should be noted that for all $MAPbI_3$ films on the different substrates, A_1 is on the order of -0.015 and A_2 around -0.005 which shows that the decay process of τ_1 is the prominent decay of the total signal. The negative sign for the $A_{1,2}$ values refer to the nature of the TAS peak. A negative value means it is either due to ground-state bleaching or stimulated emission processes, whereas a positive value can indicate transient absorption or product absorption processes. A lifetime in the range of a couple of nanosecond, the actual value depends on the pump fluence, has been reported in literature for $MAPbI_3$ [18], [46], [76], [84] which corresponds to τ_1. However, to the knowledge of the author a second lifetime on the order of tens of nanoseconds has not been reported. The origin of this second lifetime value is unclear. This could mean that the double exponential decay fitting function is not suitable if the second lifetime value cannot be given a physical meaning. However, it is possible that the second lifetime originates from an artificial signal. Depending on the positioning of the pump and probe lights, a sharp peak at 780 nm appears. In figure 41 the appearance of this peak is shown for a sample measured at a higher pump fluence of roughly 130 µJ/cm^2. This artificial signal falls within the ground-state bleach peak, which appears at 720-800 nm. The intensity of this peak can be tuned and is present even when the pump and probe are not overlapping on the sample. This indicates that the 780 nm signal is artificial. Furthermore, no decay of the signal is witnessed from a -125 ns to 5 µs window, as shown in the kinetic profile. The signal

is already present before the pump has even excited the $MAPbI_3$ film ($t < 0$). Therefore, the origin of this second lifetime could be due to the initial ground-state bleach decay not going back to the same ΔA value at $t < 0$. Instead ΔA decreases to the artificial background signal, which was found to be constant and < 0 until $t = 25$ µs. However, another possibility is that the second lifetime is not actually due to the artificial signal but due to a different recombination process. It is known that especially at high pump fluences, such as 80 µJ/cm^2, that non-radiative recombination processes such as Auger recombination increase [76]. Such recombination processes could be longer-lived than the τ_1 lifetime which has been reported in literature to be around a couple of ns. To determine whether the origin of this second lifetime is due to for instance the artificial background signal or a longer lived type of recombination process, a set of experiments should be performed at significantly lower pump fluences. At pump fluences in the range of 1-20 µJ/cm^2 the second-order radiative recombination process should dominate the total recombination regime and therefore only a single decay process should be present in the kinetics. If a single lifetime fitting is still not describing the decay process properly then the artificial background signal is most likely the cause. This artificial background signal could be inherent to the TAS apparatus layout with the $MAPbI_3$ coated substrates. By switching to another apparatus or changing the angle of irradiation attempts can be made to remove this artificial background signal. Finally it should be noted that for the $MAPbI_3$ films on glass no clear presence of a positive ΔA transient absorption phenomena is present at the pump fluence of 80 µJ/cm^2.

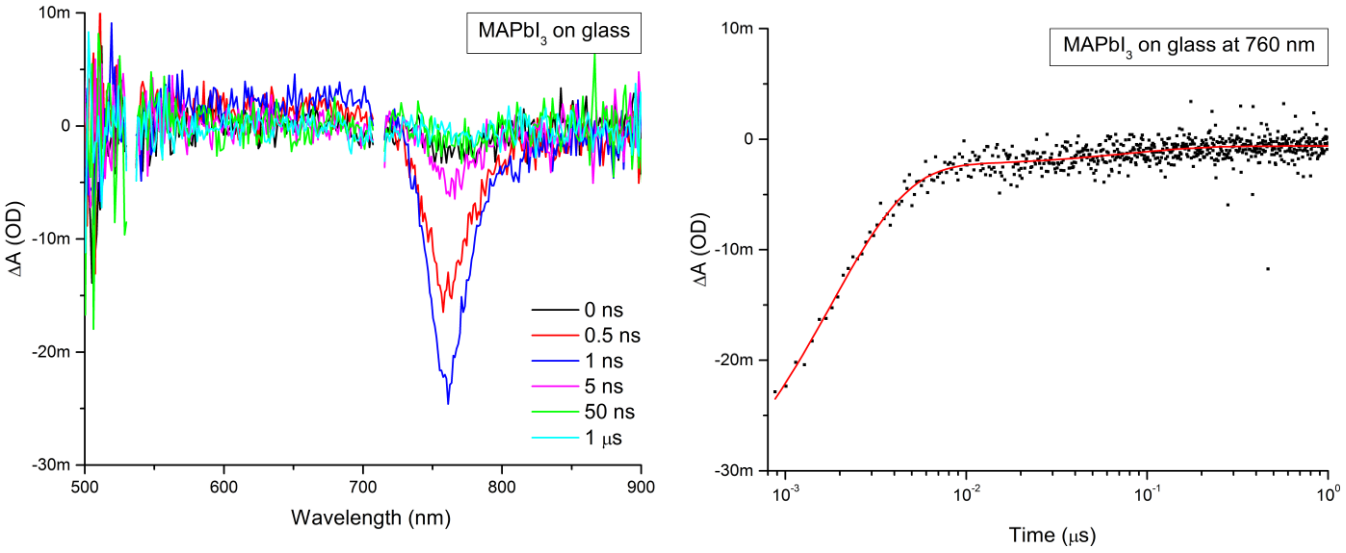

Figure 40 TAS spectral and kinetic data of $MAPbI_3$ on glass at a pump fluence of ~80 µJ/cm². Left) TAS spectra at different probe delay times. Right) Kinetic profile fitted with a double exponential function (red line) of the TAS spectra on the left at 760 nm

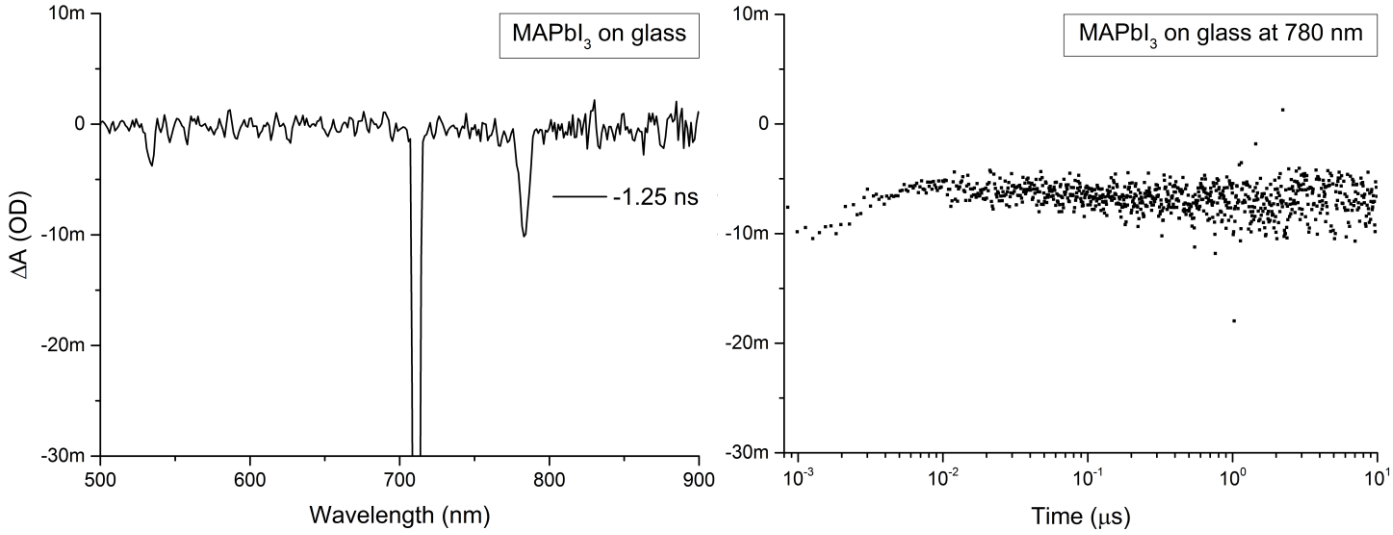

Figure 41 TAS spectral and kinetic data of $MAPbI_3$ on glass at a pump fluence of ~130 µJ/cm². Left) TAS spectra of the same $MAPbI_3$ sample in figure 39 taken before the arrival of the pump which shows the presence of the 780 nm artifact signal as well as the 710 and 532 harmonic oscillations. Right) Kinetic profile of the artifact signal at 780 nm showing the non-degrading signal upto 10 µs.

Due to the similarity in the TAS spectra of the $MAPbI_3$ thin films on different substrates, only the fitted lifetimes, τ_1 and τ_2 are shown here in table 9 and the TAS spectra and kinetics are presented in appendix F. The τ_1 lifetime increases when $MAPbI_3$ is coated on top of a HTM substrate as compared with the glass substrate where the largest increase is about 0.8 ns for the 0.5-10% Co substrates. In literature it has been reported for $MAPbI_3$ that τ_1, decreases due to the interface with Spiro-OMeTAD as HTM layer [80]. The origin of this being that charge injection from the $MAPbI_3$ VB hole into that of the HTM VB leads to accelerated regeneration of the ground-state bleach signal due to replenishing of electrons near the VB edge [18], [84]. However, as mentioned before the lifetime of the ground-state bleach of

$MAPbI_3$ is already at the limit of the time resolution of the nanosecond TAS setup. Direct charge transfer or injection phenomena which occur at sub nanosecond scale cannot be observed unfortunately with the nanosecond TAS setup. An increase in τ_1 indicates a decrease in the rate of decay through any of the possible recombination processes. This could then indicate either better film formation or increase crystallinity of the $MAPbI_3$ on nickel and cobalt oxide substrates due to better charge carrier separation within the film itself and possibly lower density of trap sites and defects. However, an opposite trend is observed for the second lifetime, τ_2. The correlation of these two lifetime trends with each other is problematic since the origin of this second lifetime is not fully understood. If it is indeed artificial then the ground-state bleach decays to a value < 0 ΔA instead of 0 ΔA since the artificial background signal itself has a negative ΔA. The trend observed could merely be due to the real and artificial signals mixing with each other differently for the different samples. This would then also imply that τ_1 itself might not be the true value for these samples as it would be partially mixed with the artificial signal. On the other hand, if τ_2 is indeed due to a real decay process it could be due to auger recombination at high pump fluence or due to defect/trap sites. If that is the case then a shorter lifetime for τ_2 would mean an increase of decay by that pathway. This would then imply either that $MAPbI_3$ on these different nickel and cobalt substrates have increased auger recombination which would be due to increased charge carrier formation and hence could mean better film formation. Another possibility though would be that these $MAPbI_3$ films possess more defects and trap states when coated on the nickel and cobalt oxide substrates since also this would increase the decay rate and thus decrease the lifetime, τ_2. No definitive answer can be given for the trend observed for the two lifetimes as well as the origin of the second longer lived lifetime. Therefore, the suggestions provided earlier to measure the TAS spectra at much lower pump fluence as well as attempting to remove the artificial back ground signal combined with coating uniform layers of both the nickel and cobalt oxides on glass and $MAPbI_3$ on those substrates and glass should simplify the analysis.

Table 9 Summary of the ground-state bleach lifetimes at 760 nm of the $MAPbI_3$ layer on different substrates. Two lifetimes are given which are obtained from the fitting of the kinetic profiles using a double exponential function with an x-offset. The standard deviation is based on the obtained lifetime values from measurements on two different samples per substrate type.

MAPbI3 substrate	GSB τ_1 (ns)	GSB τ_2 (ns)
glass	1.6 ± 0.2	77.6 ± 0.0
NiO	1.8 ± 0.1	79.0 ± 8.9
0.1% Co	2.3 ± 0.0	26.6 ± 2.3
0.5% Co	2.4 ± 0.1	33.8 ± 2.5
1% Co	2.4 ± 0.3	33.5 ± 2.1
5% Co	2.4 ± 0.3	30.7 ± 8.2
10% Co	2.4 ± 0.0	38.8 ± 2.2
Co3O4	2.2 ± 0.2	50.3 ± 31.0

3.4 Part IV: Fabrication of Complete Hybrid Perovskite PV

In figure 42 the cyclic voltammetry J-V curves are shown for the full hybrid perovskite PV cell with the following layout: FTO/NiO/$MAPbI_3$/$PC_{61}BM$/Ag. Both the first and fifth cycle of cyclic voltammetry are presented. In the left the full range from -0.4V to 1.1V bias voltage is shown whereas in the right a close-up between 0V and 0.5V is shown. It is clear that between roughly 0 V and 0.5 V the current density is close to zero whereas otherwise high current densities are achieved. This horizontal plateau shows that the PV cells generate little to no photocurrent and thereby suffer most likely from severe series and shunt resistance. However, the horizontal plateau indicates that there is no short-circuiting. If there would be short-circuiting in which the two ohmic contacts are in direct contact with each other, then a linear slope through the entire I-V plot would be expected. This means that the layout at discussed in figure 17 is at least successful in prevent a short circuit throughout the PV cell. However, as mentioned above the photocurrent extracted is very small. The values of J_{sc}, V_{oc}, FF and PCE are given in table 10. Compared to current hybrid perovskite PV devices where J_{sc} is around 20 mA/cm^2, V_{oc} ~ 1 V and FF of 0.7-0.8 giving a PCE minimum of 14% the values obtained here are very low [10], [86], [87]. The low J_{sc} and V_{oc} indicate severe series and shunt resistance values. Normally at first the series and shunt resistance only affect the FF until they become so large that also J_{sc} and V_{oc} are lowered. The slight change of J_{sc} and V_{oc} in the first five cycles could be attributed to two different effects. Light-soaking, which is simply the event of illuminating the PV for a prolonged time, is known to increase J_{sc} due to increased number of free charge carriers in the VB and CB of the layers which increase the overall conductivity as seen in equation 1. However, these devices are not sealed so that the decomposition of $MAPbI_3$ by moisture is taking place and is most likely accelerated due to the absorption of photons by the $MAPbI_3$ layer which heat up the entire PV cell which in turn decrease V_{oc} and probably also J_{sc} to some extent.

Table 10 The I-V curve characteristic parameters tabulated for the first and fifth CV cycles of a complete $MAPbI_3$ cell. The values of J_{sc}, V_{oc}, FF and PCE are obtained from figure 42 and equations 4 and 5.

Cycle	J_{sc} (mA/cm^2)	V_{oc} (V)	FF	PCE (%)
First	-1.18	0.42	0.49	0.24
Fifth	-1.36	0.35	0.52	0.25

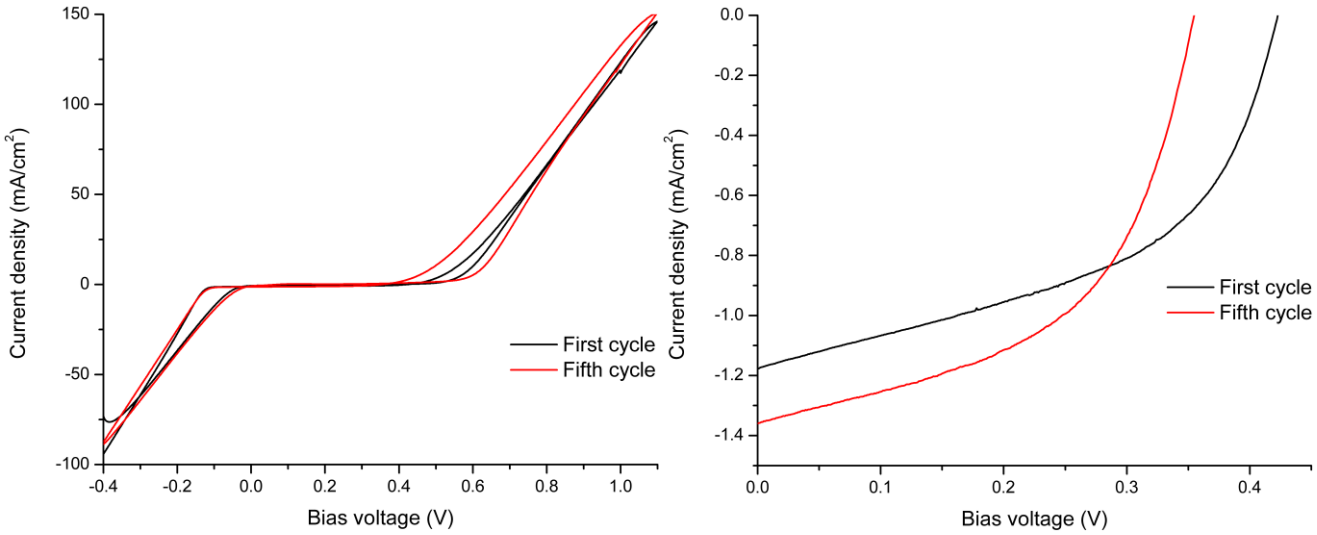

Figure 42 The I-V curve of a complete $MAPbI_3$ cell. The cyclic voltammetry data of the first and fifth cycles are shown. Left) The full range of the I-V curve. Right) Zoomed-in between 0V and 0.5V for the visualization of J_{sc} at V=0, V_{oc} at J=0 and FF from which the PCE values are obtained.

Upon close inspection of the PV cells after the cyclic voltammetry analysis an interesting observation was made. It appeared that in the region where the silver layer was deposited with the sputter coater, a yellow film was being formed instead of the dark brown which originates from the hybrid perovskite. The presence of yellow spots or a even layer is normally a clear indication of the presence of PbI_2 for $MAPbI_3$ films. In chapter 1 it was already discussed that PbI_2 is not only the precursor but also the decomposition product that stays behind when the hybrid perovskite is being degraded. In figure 43 an image is shown of the back side of these PV cells after testing them. The small square in the middle is where the PV cells were illuminated. The formation of a yellow colored phase is seen only there where a silver layer was deposited on top of the ETM layer.

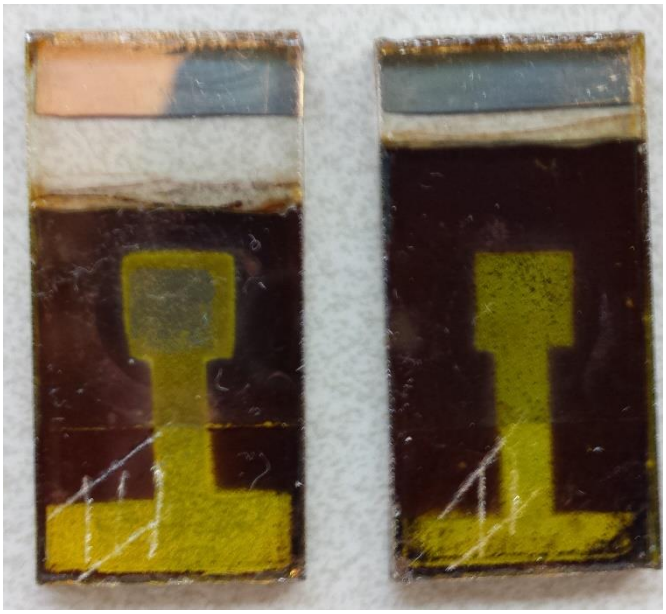

Figure 43 Photographic images of the back side of the complete $MAPbI_3$ cells. The reacction of the Ag sputtered top layer and the $MAPbI_3$ layer is visualized by the presence of the yellow film correpsonding to AgI and PbI_2. As reference, a Ag strip is deposited on the uncoated FTO which remains metallic of nature with its distinct color.

XRD analysis done on these PV cells is shown in figure 44. It indeed shows clear presence of both the PbI_2 and MAI (001) reflections. Furthermore, it shows the presence of crystalline silver, which is expected considering the deposition of the Ag cathode layer with the sputter coater but there are also reflections belonging to AgI. The (002) and (111) reflections of AgI are present at 24.4° and 38.5° 2Θ. Recently Kato, *et al.*, reported that Ag deposited as a cathode on top of organic ETM or HTM layers reacts with volatile iodide species originating from the $MAPbI_3$ layer to form AgI [21]. They proposed that the organic HTM and ETM layers are quite porous and therefore facilitate the diffusion of H_2O in the air towards the $MAPbI_3$ layer. There H_2O reacts with the hybrid perovskite to produce volatile iodide compounds such as MAI and HI which themselves then diffuse towards the Ag layer where they react with Ag and form AgI. The formation of the semiconductor AgI greatly reduces the metallic conductivity of the cathode layer and creates large resistance values within the cell. Furthermore, the decomposition of the $MAPbI_3$ layer itself leaves a PbI_2 film behind which further increase both resistance values and reduces the quantity of the active solar energy absorber $MAPbI_3$ thus decreasing the generated photocurrent. It should be noted though that their initial PCE values exceed 10% and that the decomposition of their PV cell begins only after hours of the unsealed PV cells due to moisture (not under working conditions which would accelerate decomposition). In the present case of this research however the decomposition was observed to be much faster. A possible explanation is the deposition method used to create this Ag layer. All Ag layers deposited for hybrid perovskites in literature that were found have been deposited using a thermal evaporator. However, the deposition method available for this research was that of a sputter cutter. With FIB-SEM it was already observed that sputtering a thin Pt layer on top of the $MAPbI_3$ film even under the slowest deposition rates would decompose this film. Even though an ETM layer is deposited on top of the hybrid perovskite before Ag layer deposition this does not seem to protect the $MAPbI_3$ layer. First of all, such organic HTM and ETM such as the here used $PC_{61}BM$ are

reported to be porous (pinholes) when deposited with a spin coater and could therefore easily facility Ag sputtered atoms to reach the $MAPbI_3$ film [8], [9], [19], [21]. Sputtering is known to cause deeper substrate penetration than for instance thermal evaporation due to a difference in the kinetic distribution of the released atoms as well as the substrate damaging by arcing during sputtering [88]. This could then explain why in the case of sputtering a Ag cathode layer the decomposition of the $MAPbI_3$ layer is accelerated and upon initial testing very low I-V characteristic values are obtained within the first cycles. A solution to this problem would be to deposit both the $PC_{61}BM$ ETM and the Ag cathode layer with a thermal evaporator. This way, the ETM layer is expected to be denser with less pinholes and the thermally evaporated Ag atoms not to penetrate the ETM layer and coming in direct contact with the $MAPbI_3$ layer.

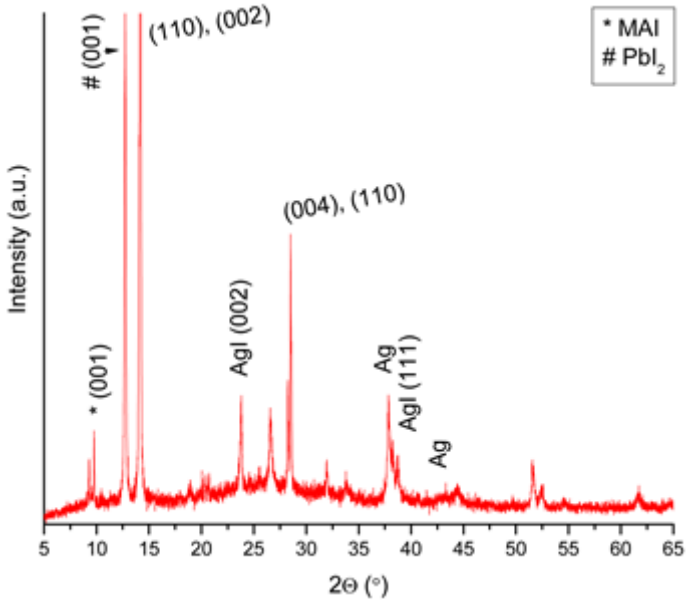

Figure 44 XRD data of a complete $MAPbI_3$ PV cell. The $MAPbI_3$ doublet reflections of (110), (002) and (004),(110) are shown for reference. The decomposition of the $MAPbI_3$ layer is noted by the presence of both the PbI_2 (001) reflection, MAI (001) reflection and the AgI (002), (111) reflections

Conclusion

NiO and Co_3O_4 thin films were deposited on both FTO and soda-lime glass substrates. With XRD and UV-Vis measurements it has been confirmed that crystalline NiO and Co_3O_4 were coated on both substrates. Uniform coating was observed on the FTO substrates for both metal oxides whereas the glass substrate was partially coated by NiO. A film thickness of 30 nm was observed for the NiO film on FTO coated in one cycle and 104 nm on the glass substrate coated in four cycles. The bad coating of the glass substrate is most likely due to both bad surface wetting with the precursor solution and the presence of many large particulates on the surface which originate from the substrate cutting and ultrasonication steps. Co^{2+} doped NiO films were prepared on the glass substrates. XRD shows no presence of Co_3O_4 or any other crystalline phase. Effects of Co^{2+} doping are observed with both XRD and UV-VIS. With XRD both a shift in the diffracting angle of the (012) reflection for NiO is observed as a change in broadness of the peaks. The FCC unit cell parameter as calculated from the (012) reflection position changes from 4.639 Å for undoped NiO up to a maximum of 4.668 Å for the Co^{2+} doped samples indication incorporation of Co^{2+} in the crystal structure. The crystallite size increases in a nearly identical trend as observed for the unit cell parameter going from 173 Å for undoped NiO to a maximum of 254 Å for 10% Co^{2+} doped NiO. An increase in crystallite size lowers the amount of crystallite boundaries in a thin film which acts beneficial for charge carrier separation. UV-VIS absorbance data shows evidence of a O^{2-} (2p) → Co^{2+} (3d) charge transfer transition for 1-10% Co^{2+} doped NiO.

Thin films of $MAPbI_3$ were successfully deposited on both the FTO and glass substrates using the two-step deposition method. With this two-step deposition method smooth and pinhole-free films were observed with FIB-SEM on the FTO substrate. Getting thickness values with a FIB proved unsuccessful due to destruction of the $MAPbI_3$ film upon ion bombardment and Pt sputtering. The XRD data show no clear signs of the presence of the $MAPbI_3$ precursors, PbI_2 and MAI, being present after deposition and thermal treatment which is further confirmed by the UV-VIS absorbance data. Furthermore, based on UV-VIS absorbance data these $MAPbI_3$ thin films were also coated successfully on the x% Co^{2+} doped NiO and Co_3O_4 substrates. However, the coating on the NiO substrate shows a much lower band gap absorbance transition which seems to indicate incomplete formation of the crystalline $MAPbI_3$ coating.

PL measurements were performed to check how well the HTM layers would quench the PL signal of $MAPbI_3$ due to hole injection from the $MAPbI_3$ layer into the HTM layer. Compared to a reference substrate of a $MAPbI_3$ film on glass, the quenching efficiencies increase from 14.7% for $MAPbI_3$ coated on the undoped NiO up to 90.8% for 10% Co and even 98.8% for Co_3O_4. For undoped NiO quenching efficiency values of 98% have been reported [46] and the extreme difference observed with the obtained value here is most likely due to the bad surface coating of glass with NiO as observed with FIB-SEM. Some caution has to be taken with the value obtained for Co_3O_4 as these measurements were performed by back side illumination and therefore Co_3O_4 will have partially attenuated the incoming beam before it could excite the $MAPbI_3$ film. Transient absorption spectroscopy showed only a ground-state bleach signal of the $MAPbI_3$ film on either glass or the HTM coated substrates at a ~80 $\mu J/cm^2$ pump fluence. Direct charge injection could not be observed due to the resolution limit of the TAS setup. Furthermore, the ground-state bleach kinetic data had to be fitted with a double exponential function. The first lifetime is on the same order as reported literature [18], [46], [76], [84] and increases from 1.6 ns for the glass substrate up to 2.4 ns for the doped nickel and cobalt oxide substrates. The increase of the ground-state bleach lifetime indicates an

increase of the charge carrier lifetime and could imply better $MAPbI_3$ film formation or crystallization on the latter substrates. The origin of the second lifetime is unclear as it could be either due to an artificial back ground signal observed which overlaps with the ground-state bleach region or due to a second recombination process which is longer lived into the tens of ns range which seems to be unreported in literature.

Attempts to fabricate complete hybrid perovskite cells were made in which an ETM layer of $PC_{61}BM$ was spin coated on top of the FTO-NiO-$MAPbI_3$ layers and subsequently covered by a thin layer of Ag deposited with a sputter coater. Unfortunately, it was found that the Ag layer as coated with the sputter coater reacted with the $MAPbI_3$ layer upon deposition to form AgI which was observed with XRD after the deposition. Most likely, the $PC_{61}BM$ layer contained pinholes so that the gas phase Ag species could penetrate through the ETM layer and come into direct contact with $MAPbI_3$. These complete cells showed very low PCE values around 0.24% under illumination due to a combination of low J_{sc}, V_{oc} and FF.

Finally, no definitive conclusion can be made on what the optimum Co^{2+} doping value for NiO is with regards to $MAPbI_3$ PV solar energy conversion characteristics or if Co_3O_4 outperforms the typically used HTM materials. However, the QE values obtained for Co_3O_4, which has not been used for $MAPbI_3$ PV so far, do show it functions as a suitable HTM layer.

Outlook

The coating of NiO and Co_3O_4 on FTO was uniform but the coating of NiO on the glass substrate proofed to be incomplete. The consequence was that the PL QE values were well below reported values in literature for NiO. Thus it is important completely coat the substrate surface. This can be done by either using more controlled deposition methods such as CVD, PVD, ALD and spray-pyrolysis [80], [89] or by using different inert substrates such as Al_2O_3 coated FTO and quartz.

To correlate the obtained results here to the effect of Co doping on NiO but also the completely different Co_3O_4 material more FIB-SEM studies should be performed to investigate the effect of substrate coating, surface morphology and film thickness for the different layers. For instance, the increase of photoluminescence quenching upon Co doping of NiO and using Co_3O_4 could be because of better surface coverage due to the presence of the cobalt precursor instead of different material properties.

Within this research the x% Co doped NiO samples were named after mol% Co^{2+} precursor in the coating solution and therefore 100% inclusion of the Co^{2+} dopants in the NiO crystal structure has been assumed. The theoretical values could differ significantly though from actual doping content and thus techniques such as ICP-AES and XPS should be used to confirm the level of doping. To complement this, grazing incidence XRD and XANES/EXAFS should be used to confirm the presence or absence of different phases and oxidation states (Co^{3+}).

In the case of $MAPbI_3$ the thickness of the spin coated layers could not be determined because the combination of the focused ion beam and the sputtering of Pt to get a cross-section image destroyed the $MAPbI_3$ layer. Both non-contact (optical) and contact surface profilometry techniques could be used to get information on the layer thickness.

PL measurements were performed by backside illumination of the $MAPbI_3$ layers on different substrates. The reason for backside illumination is given in appendix D. The disadvantage of backside illumination is that the incoming beam has to travel through the HTM layers first. This leads to attenuation of the beams intensity due to reflection and absorption processes. Using a dedicated PL setup for thin films should allow front side illumination and rule out any attenuation effects by the HTM layers.

The transient absorption spectroscopy data was difficult to analyse due to the necessity of using a double lifetime exponential decay fitting function. Especially the origin or meaning of the second and longer lifetime is unclear as different options are present. To rule out if the second lifetime is due to a real recombination process or an artificial back ground signal a few things could be done. First of all, by lowering the pump fluence to about 1-20 $\mu J/cm^2$ only a single radiative recombination process should be present for the ground-state bleach and thus a single lifetime fitting function should be sufficient. Alternatively, the artificial signal is only observed for the $MAPbI_3$ coated substrates and therefore perhaps these substrates have to be positioned differently with respect to the layout of the TAS apparatus to remove this artificial signal.

It would be very interesting to directly follow the charge injection rates and lifetimes of the $MAPbI_3$ photogenerated hole into the VB of the HTM with an ultrafast TAS setup because these lifetimes appear in the sub nanosecond regime.

Pl and TAS provide insightful hole dynamics between the $MAPbI_3$ and the HTM layers but gives no definite information as to how efficient PV cells based on the HTM layers would be. In the end it is about how efficiently a hybrid perovskite PV cell can convert photons into electricity without degrading significantly within the first ten thousand hours. Therefore, complete hybrid perovskite PV cells should be fabricated in a more gentle approach. The most feasible route is to deposit both the $PC_{61}BM$ ETM layer and the Ag cathode layer with a thermal evaporator. This technique is reported to be less destructive and have smaller penetration depths compared to sputtering. Furthermore, by depositing $PC_{61}BM$ with a thermal evaporator a pinhole free layer can be coated with slows down moisture diffusion towards the $MAPbI_3$ layer and therefore increases stability. Finally, such complete $MAPbI_3$ PV cells will provide insight into the effect of Co^{2+} doping NiO for the cells power output and the possible use of Co_3O_4 as a novel HTM layer for hybrid perovskite PV in general.

A final interesting aspect would be to investigate if the $ZnCo_2O_4$ normal spinel could be used instead of Co_3O_4 as HTM [90]. The reason is that Zn^{2+} is a d^{10} ion and thus will have completely filled t_2 and e energy states. This will therefore remove the d Co^{3+} → d Co^{2+} charge transfer transition which is observed as the 1.5 eV band gap in the bulk solid. Therefore, $ZnCo_2O_4$ would be a more transparent HTM like NiO which decreases the attenuation of incoming photons towards the $MAPbI_3$ layer and should increase the current density and thus the PCE. However, it should be investigated what the effects on the position of the -5.4 eV VB edge position is due to orbital mixing of O^{2-} and Zn^{2+} and if it can therefore still function as HTM.

Acknowledgement

During the last 12 months I have been working with thin film fabrication and characterization under the supervision of Iván Garcia Torregrosa, Dr. Monica Barroso Silva da Cruz and Dr. Celso de Mello-Donega. Due to the opportunity provided by them to do this research under their supervision, I have learned about and worked with many new techniques such as spin coating, FIB-SEM, PL, CV and TAS. Furthermore, the scope of this research, thin films and photovoltaics, was completely new to me and therefore I find the knowledge obtained in this field to be a great addition for my study.

Therefore I would like to explicitly express my gratitude towards my supervisors. My daily supervisor, Ivan, was of great help in learning to use the spin coating technique, getting to know cyclic voltammetry, performing FIB-SEM on my samples and for general discussions. My first supervisor, Monica, has been of crucial importance in the guidance of the project and many interesting discussions lead to new ideas for experimental work and the analysis of results. Thanks to my second supervisor, Celso, I was able to perform a series of photoluminescence measurements at CMI. Finally I would like to add that under their supervision, I have not only possessed valuable knowledge but also grown as a person in terms of responsibility and ambition.

There are a few other colleagues I would like to show my gratitude for their contribution to this project. First of all, Anne Berends from CMI provided great help with the photoluminescence measurements, which turned out to be more challenging than we had anticipated at first. Rogier Brand provided the AFM measurements on the glass slide substrates after different treatments. Marjan Versluijs-Helder provided valuable insight for the analysis of the XRD results. Helpful and interesting discussions were achieved with Jochem Wijten and Gang Wang, fellow graduate students Remco Dalebout and Laurens Mandemaker and of course all the members of the Solar Fuels group under the supervision of Dr. Monica Barroso Silva da Cruz.

Appendixes

Appendix A: Theoretical Thin Film Reflectance Spectra

Indications of the interference patterns for a single thin layered substrate and a multi-layered substrate. In figure 45 the theoretical reflectance spectra are shown using Filmetrics© calculator based on Fresnel equations for a 52 nm layer with a refractive index of 2.4 at 632.8 nm on SiO_2 bulk substrate with and without a 300 nm FTO layer inbetween [79]. The 52 nm layer used to simulate a NiO or Co_3O_4 layer on glass or the FTO/glass substrate. As soon as the FTO layer is introduced the reflectance spectra is greatly complicated, going from a single interference fringe to at least 4 in the 300 to 1000 nm window. However, not knowing the actual refractive index of the synthesized x% Co doped NiO and Co_3O_4 films these theoretical reflectance spectra should not directly be compared (and thus subtracted) from the obtained experimental UV-Vis absorbance spectra.

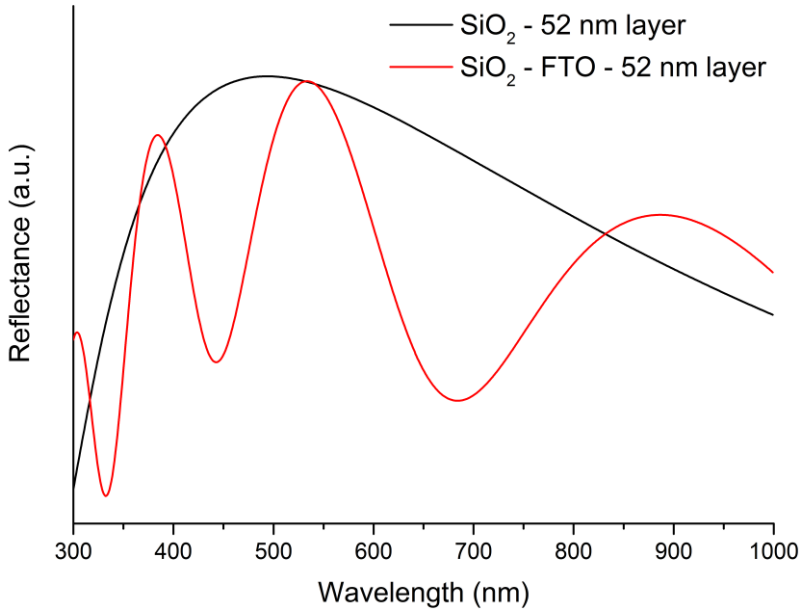

Figure 45 Theoretical reflectance spectra of a 52 nm thin layer with a refractive index of 2.4 at 632.8 nm on either a SiO_2 bulk substrate or SiO_2 – FTO(300 nm) substrate. Spectra are calculated using the Filmetrics© calculator [79].

Appendix B: Discussion on the Use of Tauc Plots

In general a Tauc plot gives a reasonable approximation of band gap values due to the relationship between the absorption coefficient, α, and the band gap energy, E_g. This relationship is shown in equation 12 where $h\nu$ is the photon energy, A is a constant and m is a factor depending on the type of transition. For direct allowed transitions m takes on the value of ½.

$$\alpha = \frac{A(h\nu - E_g)^m}{h\nu} \tag{12}$$

By plotting $(\alpha h\nu)^2$ versus $h\nu$ for a direct allowed band gap the band gap energy, Eg, can be found as the slope of a linear region extrapolated to the x-axis. This is shown in figure 46 for the NiO films on the FTO and glass substrates. It was explicitly mentioned that Tauc plots give a reasonable approximation of the band gap. First of all, the slopes can be drawn as it suits the author since no fundamental rules are given for this except a region of linearity. Cleary, multiple regions of linearity could be found in for these films. One could even manipulate this data further by playing with the axis ranges. For these two films, without playing with the axis range, band gap values based on the drawn slopes are in the range of 3.55-4.07 eV for NiO on FTO and 3.67-3.79 eV for NiO on glass. This empirical method for determining the band gap could definitely be one of the reasons why the reported band gap of undoped NiO in literature ranges from 3.5-4.0 eV. Because of the unreliability of this method, the Tauc plot band gap values for x% Co doped NiO samples will not be compared. To further add to the unreliability, in the present research the absorption coefficient used for the Tauc plot is based on the absorbance units from the UV-Vis spectra instead of absorption values. This means that the absorbance is the sum of the reflectance and absorption and as seen in the results section and appendix A the reflectance for thin films can be significantly high and non-linear. Therefore, there is already a significant non-linear error in α which in turn adds a significant error in the Tauc plot data.

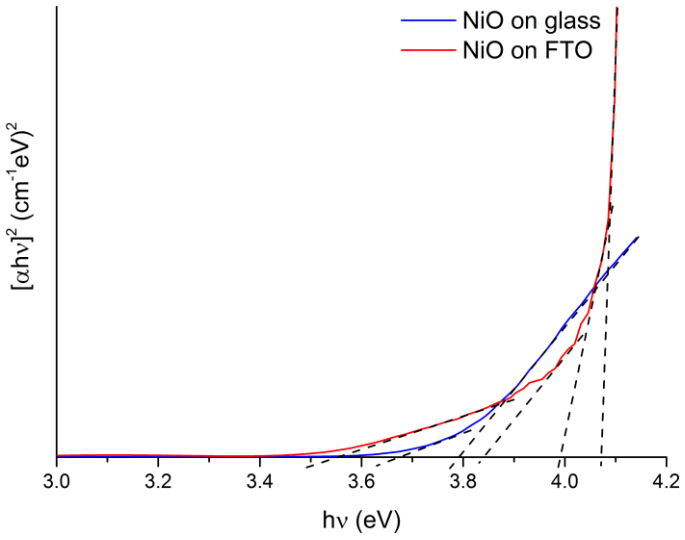

Figure 46 Tauc plots of the NiO films coated on the glass (blue) and FTO substrates (red). Tangents drawn at linear regions and extrapolated towards the x-axis are readily used in literature to define band gap values. The Tauc plot here shows only a few of the many present linear region to which a tangent line is drawn.

Appendix C: Comparison of $MAPbI_3$ Deposition Methods

For the deposition of hybrid perovskites using the spin coating technique three different methods have been developed as thoroughly described in the methodology. A short summary of the results produced by utilizing these three methods will be discussed here from which the two-step deposition method has been chosen as the most suitable method within this research.

In figure 47 the XRD results are shown for the one-step deposition, the two-step deposition and the sequential deposition of $MAPbI_3$ films on FTO. The XRD data of the two-step deposition has already been shown in the results section on both FTO and glass substrates. The first interesting observation is the complete absence of the FTO reflections for the one-step deposition sample and a gradual increase of the FTO intensity going from two-step to sequential deposition. Furthermore, both the one-step and two-step deposition do not show a clear presence of PbI_2 as the small peak before the (110),(002) doublet was already identified as the Kβ reflection. However, for the sequential deposition the intensity of at the Kβ reflection is significant and thus it is plausible that the PbI_2 layer has not been fully converted yet. This seems to be confirmed by the barely visible presence of the (001) reflection of MAI. The presence of both unreacted MAI and PbI_2 seems to hint towards incomplete conversion and that longer annealing times might be needed.

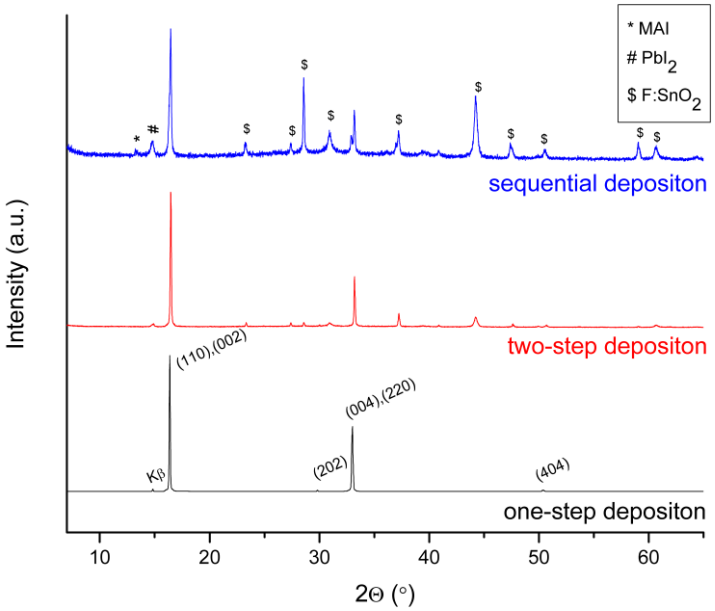

Figure 47 XRD data of $MAPbI_3$ films deposited on FTO with the three different described methods. The FTO substrate reflections are noted with the $ symbol and the (001) reflections of the precursors MAI and PbI_2 with respectively the * and # symbols.

Figure 48 shows the surface morphology of the three different hybrid perovskite films. Images (A) and (B) are of the one-step deposited sample. A similar partial coating has been observed already for the NiO layer on the glass substrate. Even though the same effect is observed, the substrates of choice are different, FTO and soda-lime glass. It has been reported in literature that the single deposition method is the worst of the three spin coating methods due to the uncontrolled deposition with the consequence of pinhole formation. However, the partial coating such as observed here on FTO has not been reported in literature for similar deposition conditions [8], [9]. A possible explanation could be that the precursor solution was stored for one week in the dark under low humidity conditions before spin coating. Strangely though, the XRD data seems to be unaffected since the pure crystalline $MAPbI_3$ phase is obtained. For the other two methods, the two-step deposition in images (C) and (D) and the sequential deposition in images (E) and (F) the solutions used were no older than one day which is needed to fully dissolve the precursor salts. In the case of two-step deposition a smooth surface is observed with sub-micron to micrometre grains. The surface seems to be absent of pinholes which is a necessity for the fabrication of highly efficient hybrid perovskite PV. Furthermore, the two-step deposition method fully covers the surface as no partially covered parts were observed. Finally, the sequential deposition method is shown in (E) and (F). In comparison to the smooth surfaces observed for the one- and two-step deposition methods, the sequential deposition gives a very rough surface of large cuboid-shaped crystals. The rough surface could have the advantage of a larger interface area with any layer deposited on top and therefore potentially better free charge carrier separation. Furthermore, a rough surface could enhance scattering at the layer interface and thereby "trap" a part of the non-absorbed light within the hybrid perovskite layer which could then be absorbed again and therefore increase the PCE. However, a rougher surface also means more grain boundaries and therefore more defects such as kink and step sites. These defects act as trap sites and recombination centres. The overall effect of a rough surface therefore depends both on the level of roughness as well as the size of the cuboids. The larger the cuboids result in a decrease of the grain boundaries. A decrease in the grain boundaries leads to a lower defect density at the layer surface, which is considered advantageous in photovoltaics. Unfortunately, the substrate coverage of this method was not complete. Certain areas were witnessed to be fully covered however other parts on the substrate such as shown in (F) clearly show voids between the hybrid perovskite large crystals. The reason for this might be that a supposedly first flat deposited layer of PbI_2 reacts with a solvent bath of MAI to form the large hybrid perovskite cuboids. The growth process of these cuboids could be similar to the sintering process observed for nanoparticles in which initially smaller hybrid perovskite particles or monomers travel over the surface or through the solution to large crystals which grow even larger. For all these films, unfortunately no successful FIB cross-section could be made. Instead, when attempts of the FIB cross-section were done on these films, the hybrid perovskite layer was observed to diminish during the deposition of the conductive Pt layer as seen in figure 49. Therefore other surface profiling techniques such as (non-)contact profilometry or ellipsometry.

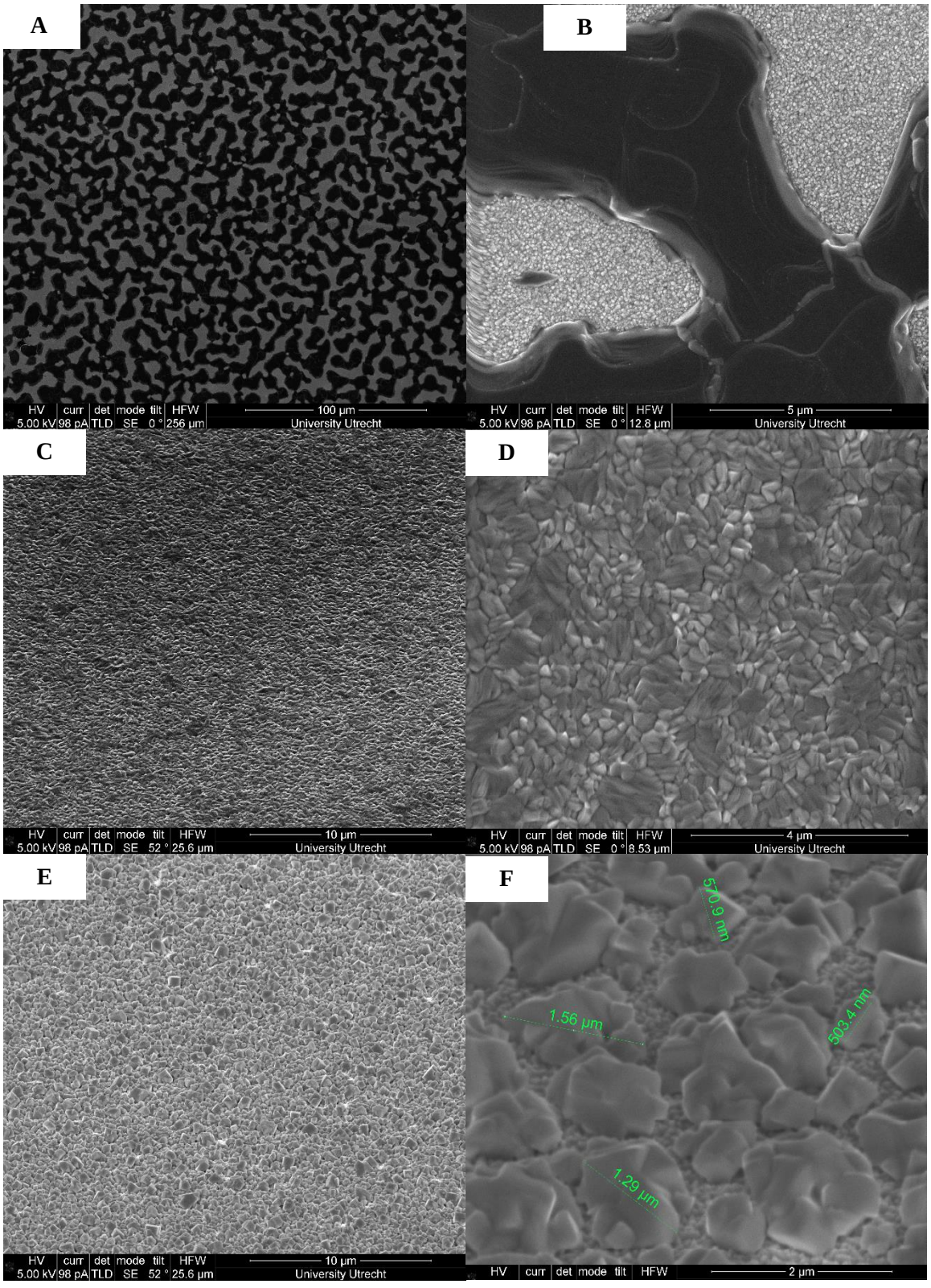

Figure 48 Top view FIB-SEM images of the one-step deposition in images A-B, the two-step deposition in C-D and the sequential deposition in E-F.

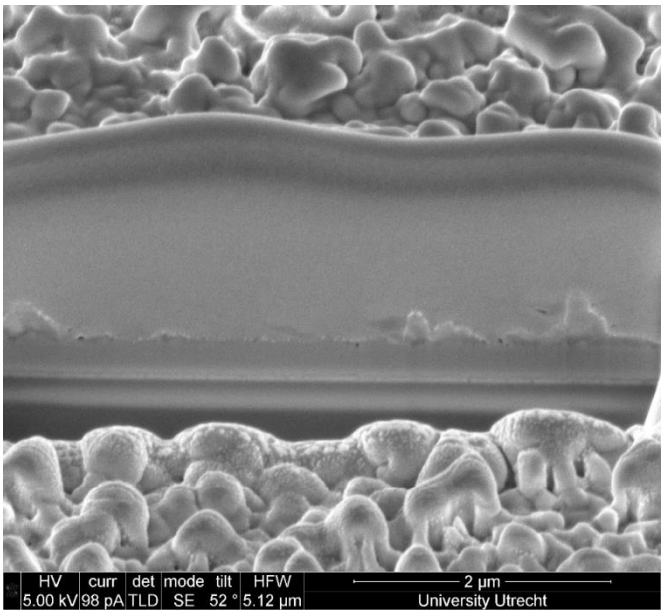

Figure 49 FIB-SEM cross-section image of a $MAPbI_3$ layer deposited with the sequential deposition method as shown in figure 48.

By measuring the UV-Vis spectra and visualizing it in absorbance units the band gap value of the hybrid perovskite can be probed as well as the presence of the precursor and decomposition product PbI_2. In figure 50 UV-Vis spectra are compared of the three different deposition methods and that of a thin film of PbI_2 deposited from a 1 M PbI_2 solution. The band gap of $MAPbI_3$ is reported to be around 1.57 eV or 780 nm. This corresponds well to the steep increase of absorbance observed at 780 nm for all three deposition methods. Furthermore, the one-step deposition method shows the largest increase in the absorbance for the non-normalized data presented here and the sequential method the lowest which corresponds to the thickness of the layer and was also observed with the FTO reflections being absent or present in the XRD data. The one-step and sequential deposition already show quite some absorbance before the band gap value of 780 nm which is probably due to scattering events at the hybrid perovskite – air interface and therefore rough or thick films are to be expected. Furthermore, at 520 nm the band gap of PbI_2, 2.4 eV, is positioned as shown in the black line with a steep increase in absorbance. For the 1-step deposition there is no increase of absorbance at 520 nm which confirms together with XRD that PbI_2 is absent in the film as expected. If the region around 520 nm is compared for the two-step and sequential deposition methods it is clear that for the sequential deposition a steeper gradient is observed than for the two-step method. For the sequential method this confirms together with XRD the presence of PbI_2 and therefore of a not fully converted film. For the two-step method however, the region from around 550 to 500 nm is linear and thus no non-linear increase of absorbance is observed at the band gap of PbI_2 at 520 nm which seems to show that no PbI_2 or significant amount of PbI_2 is present. It should be noted finally, that for the $MAPbI_3$ hybrid perovskite two band gaps are reported. The first one being at 780 nm or 1.57 eV and a deeper band gap at 480 nm. This second band gap seems to be present for the two-step and sequential deposition methods however not for the one-step deposition method. The one-step deposition method uses the $PbCl_2$ precursor and the final hybrid perovskite composition is often noted as $MAPbI_{3-x}Cl_x$ where x is a few percentages at most. Perhaps the presence of the chlorine dopant in the crystal structure effects the formation of this deeper band gap. The deeper band gap is assigned as having the same conduction band as the 1.57 eV band gap but a deeper

lying valence band. Therefore, the presence of the chlorine dopant might interfere with the formation of the deeper band.

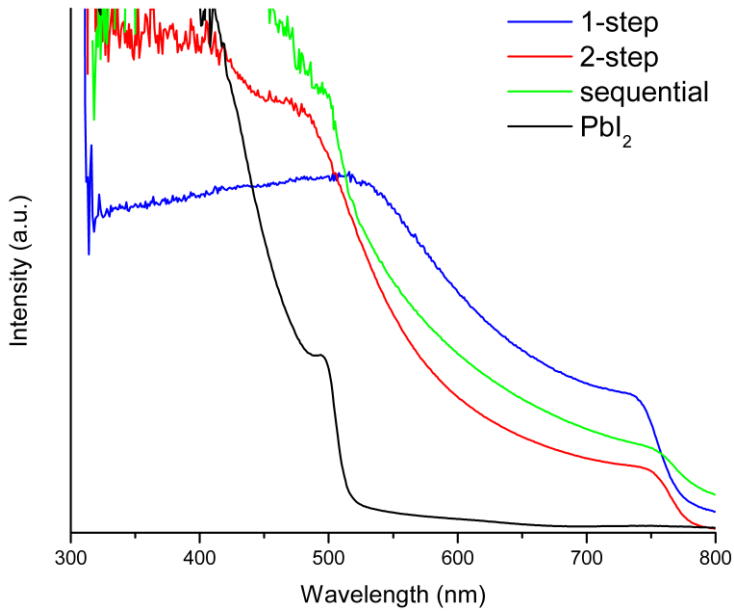

Figure 50 UV-Vis Absorbance spectra of the $MAPbI_3$ films coated on the FTO substrate from the different deposition methods and a PbI_2 reference thin film.

Combining the results of these three techniques the following is observed for each method. The one-step deposition method leads to fully converted $MAPbI_{3-x}Cl_x$ films however the coating of these films on the FTO surface is only partial with large voids and therefore making this method as utilized within this research unsuitable for hybrid perovskite PV which require full surface coverage. The two-step deposition method most likely has no PbI_2 present and therefore only the active $MAPbI_3$ phase. XRD shows a small diffraction peak at the location of (001) PbI_2 however this overlaps with the Kβ of the very intense $MAPbI_3$ doublet (110) (002). UV-Vis also shows no non-linear increase of absorbance at the band gap of PbI_2 at 520 nm. Furthermore, FIB-SEM images show a smooth film surface with complete substrate coverage and no pinholes. The last method used here, the sequential deposition, clearly shows the presence of PbI_2 in the precursor film in both XRD and UV-Vis where the non-linear absorbance increase is observed at 520 nm. A rough surface of large cuboid-shaped crystals is observed with the FIB-SEM however, just as for the 1-step deposition, the surface is not completely covered by the hybrid perovskite. Therefore, the two-step deposition method has shown to be the best method as utilized within this research for parts 3 and 4 because of full surface coverage and no clear indication that PbI_2 is still present.

Appendix D: Front side Cell Illumination Effects on PL Spectra

In the methodology it was mentioned that back side illumination was necessary to get a noticeable PL signal of $MAPbI_3$. In the results section however, it was shown that this back side illumination creates an uncertainty in the case of Co_3O_4as HTM due to possible attenuation effects. In figure 51, the front side illumination is shown for $MAPbI_3$ coated on the Co_3O_4 layer. The result is the presence of many peaks whose origin cannot be due to actual photoluminescence events. It is assumed that the polychromatic incoming beam, which is not generated by a laser, scatters both inelastically and elastically on the glass substrate and the sample holder. The incoming beam is redirected towards the detector in the front-side illumination. The result is that the scattered photons are also directed towards the detector.
By using back side illumination most of the scattering signal and the incoming beam is directed towards the opposite side (black box) and do not reach the detector.

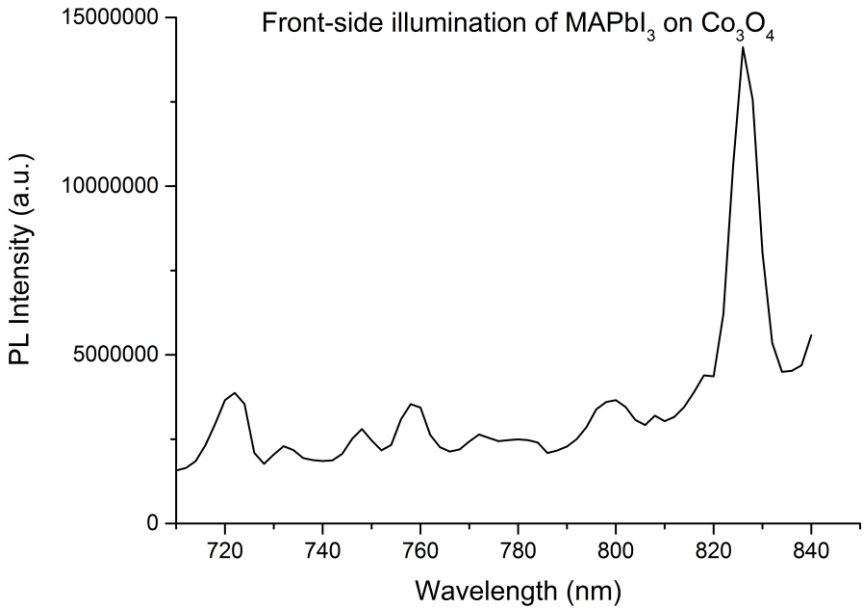

Figure 51 PL spectra of the $MAPbI_3$ layer coated on a Co_3O_4 film as measured by illuminating the sample from the front side with the excitation beam.

Appendix E: Different Fitting Functions for the TAS Data

In figure 52 the kinetic profile fitting is shown using the single and double exponential fitting equations 13a and 13b. The x- and y-offset is calculated with, respectively, x_0 and y_0. A_1 and A_2 are weighing factors, which show the contribution of each exponential part to the total fitting function and can be negative or positive in sign, depending on the value of the ΔA signal. The temporal position is given by x and the lifetime of the exponential function by τ. For the single exponential fitting a significant error is being made because of the bad fitting in the 10 ns to 100 ns region. The double exponential does seem to fit this region correctly. In terms of the lifetimes obtained, the single fitting gives a lifetime of 2.3 ns and for the double exponential the smallest lifetime is 1.8 ns with similar small errors of a few percentage.

$$y = y_0 + A_1 e^{\frac{-(x-x_0)}{\tau_1}} \tag{13a}$$

$$y = y_0 + A_1 e^{\frac{-(x-x_0)}{\tau_1}} + A_2 e^{\frac{-(x-x_0)}{\tau_2}} \tag{13b}$$

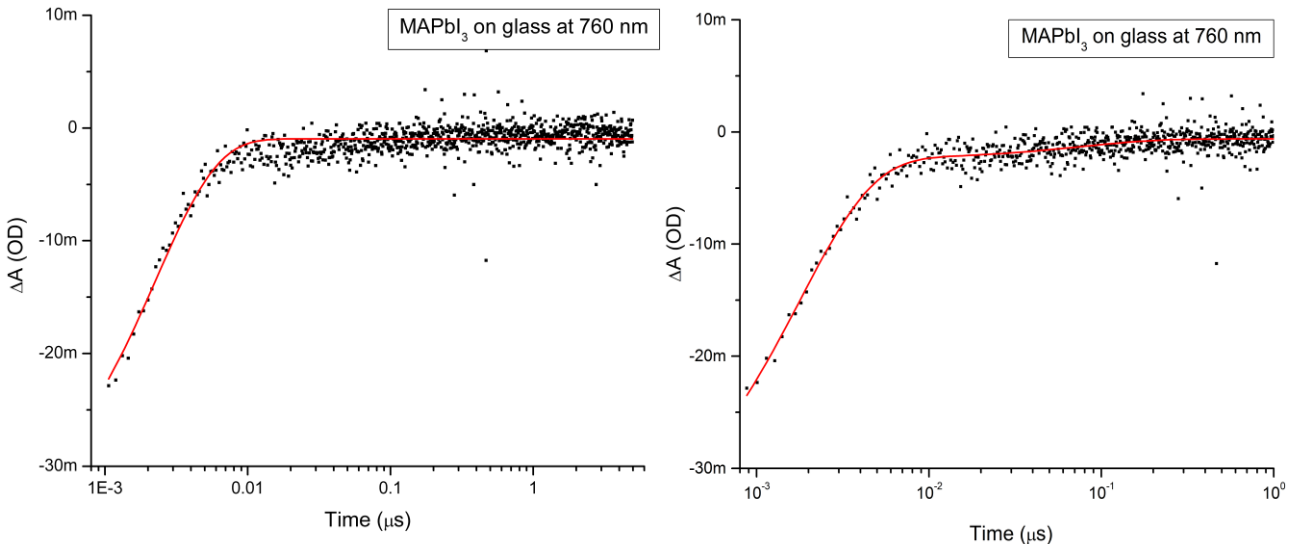

Figure 52 The kinetic profiles of the TAS data from $MAPbI_3$ coated on glass. Left) Single exponential fitting of the data. Right) Double exponential fitting of the data.

Appendix F: Collection of TAS Spectra and Kinetic Plots

Throughout figures 53-59 both the TAS spectra and kinetic plots are shown for the $MAPbI_3$ film the different substrates. The kinetic fitting results are summarized in table 9 in section 3.3.2. The 710 and 532 harmonic artifact signals have been left out if they were present.

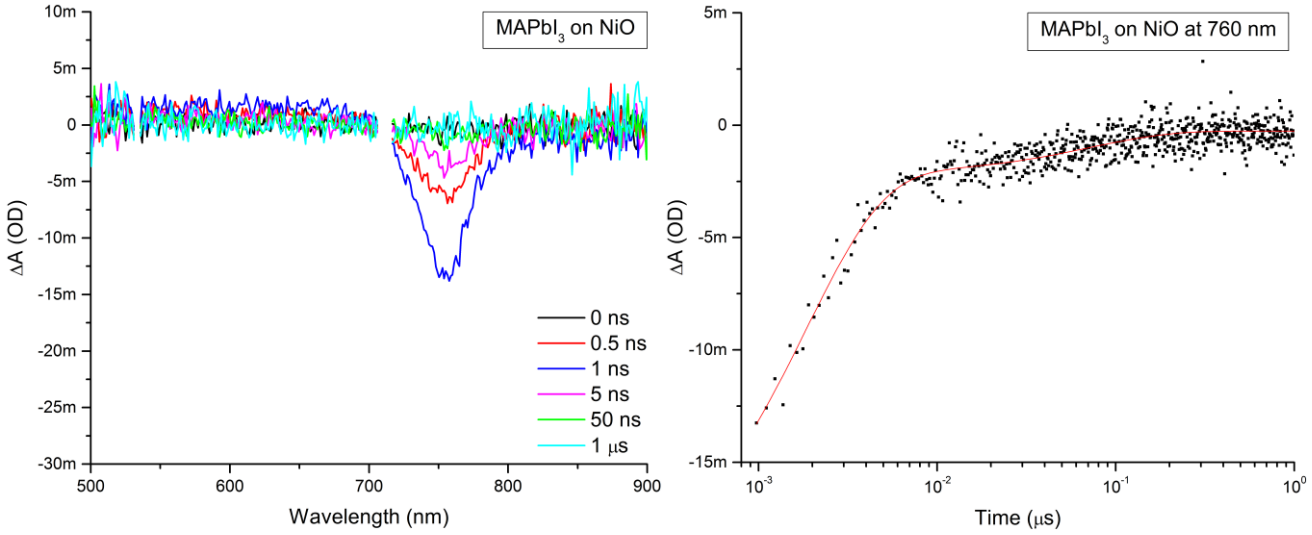

Figure 53 TAS spectral and kinetic data of $MAPbI_3$ on NiO at a pump fluence of ~80 µJ/cm². Left) TAS spectra at different probe delay times. Right) Kinetic profile fitted with a double exponential function (red line) of the TAS spectra on the left at 760 nm

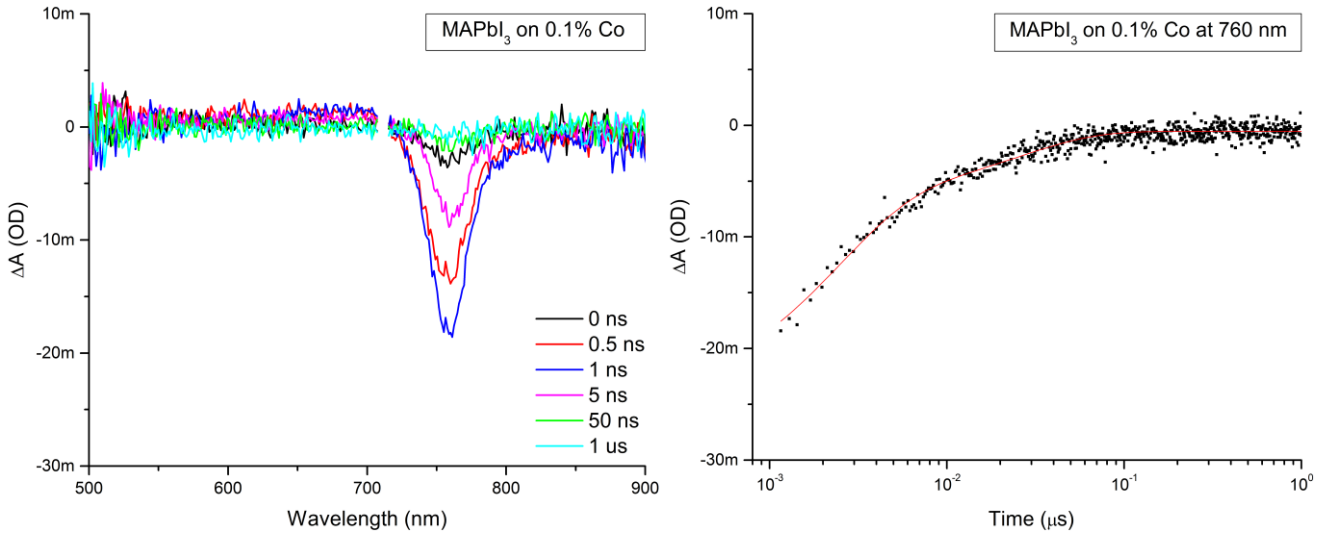

Figure 54 TAS spectral and kinetic data of $MAPbI_3$ on 0.1% Co at a pump fluence of ~80 µJ/cm². Left) TAS spectra at different probe delay times. Right) Kinetic profile fitted with a double exponential function (red line) of the TAS spectra on the left at 760 nm

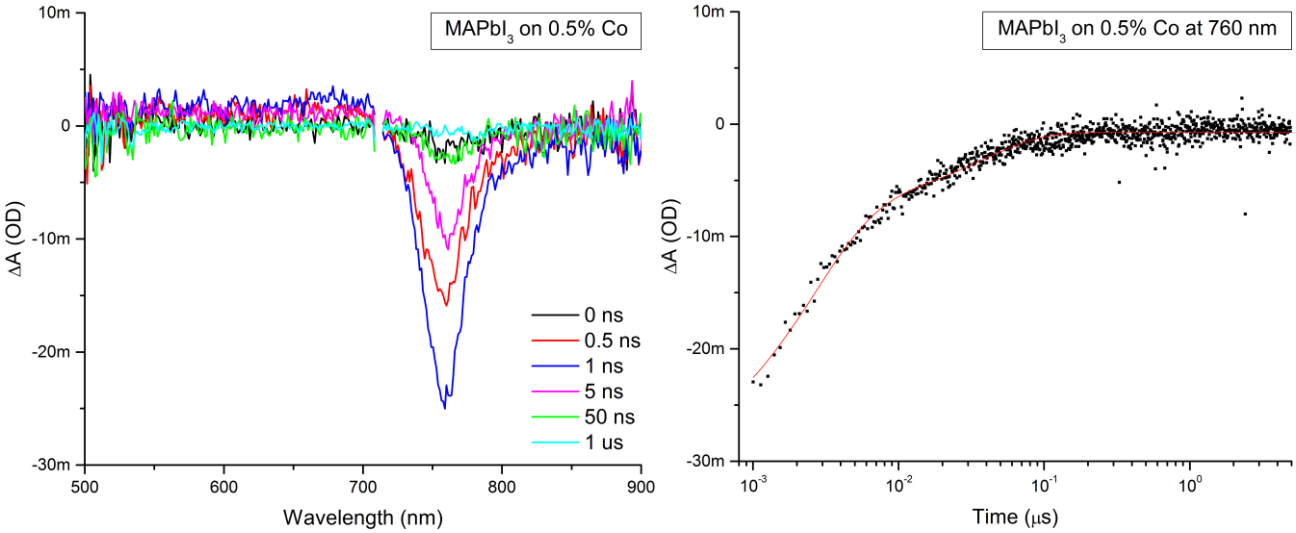

Figure 55 TAS spectral and kinetic data of $MAPbI_3$ on 0.5% Co at a pump fluence of ~80 µJ/cm². Left) TAS spectra at different probe delay times. Right) Kinetic profile fitted with a double exponential function (red line) of the TAS spectra on the left at 760 nm

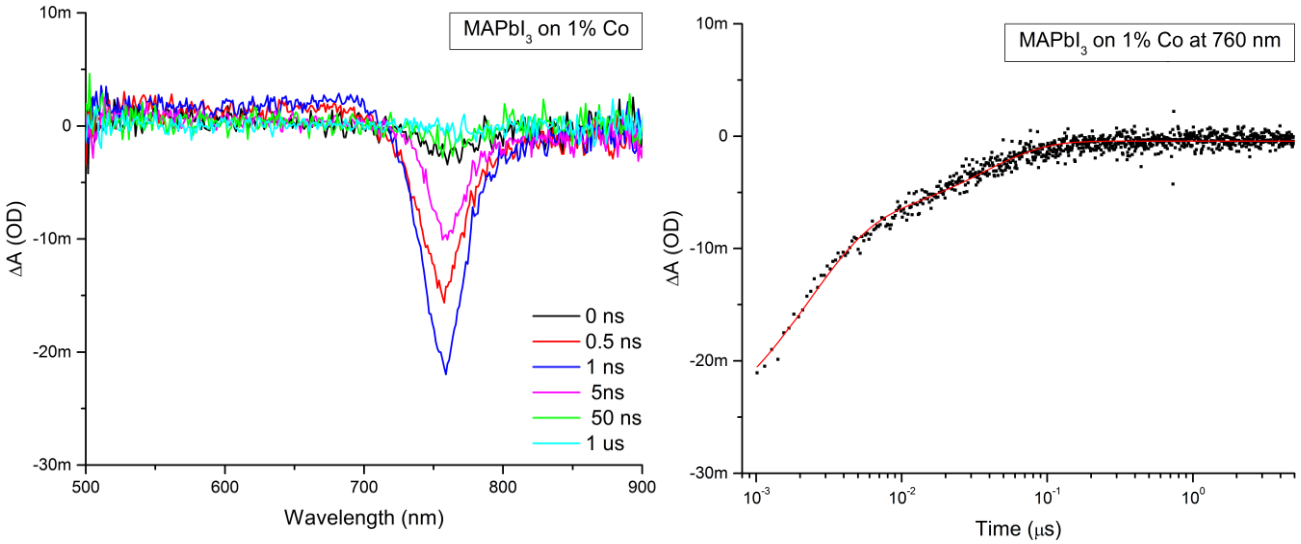

Figure 56 TAS spectral and kinetic data of $MAPbI_3$ on 1% Co at a pump fluence of ~80 µJ/cm². Left) TAS spectra at different probe delay times. Right) Kinetic profile fitted with a double exponential function (red line) of the TAS spectra on the left at 760 nm

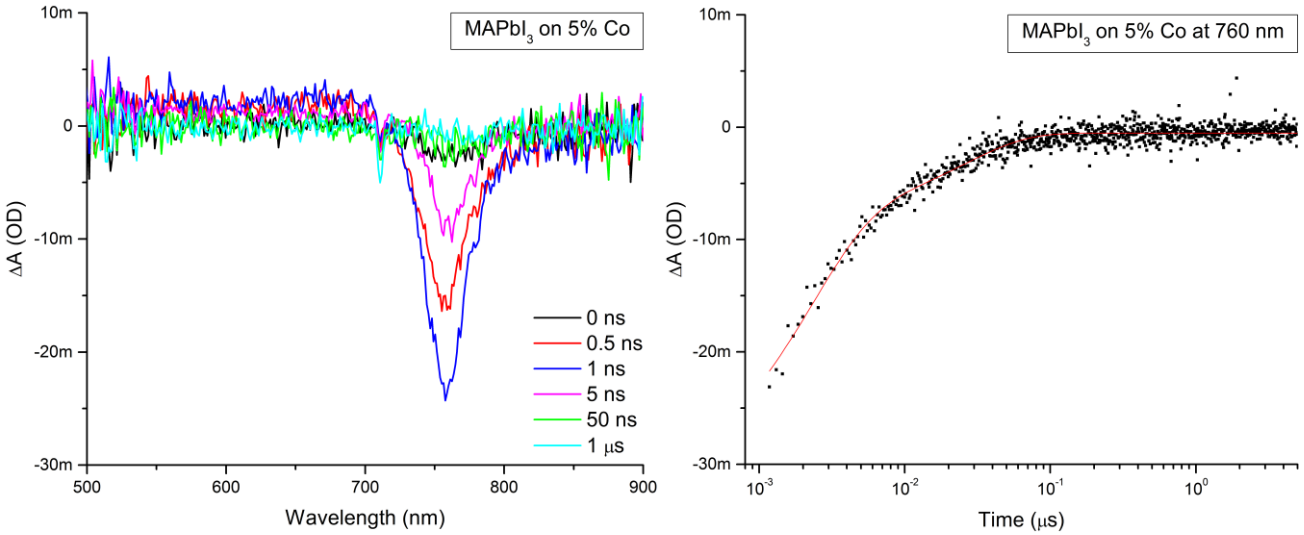

Figure 57 TAS spectral and kinetic data of $MAPbI_3$ on 5% Co at a pump fluence of ~80 µJ/cm². Left) TAS spectra at different probe delay times. Right) Kinetic profile fitted with a double exponential function (red line) of the TAS spectra on the left at 760 nm

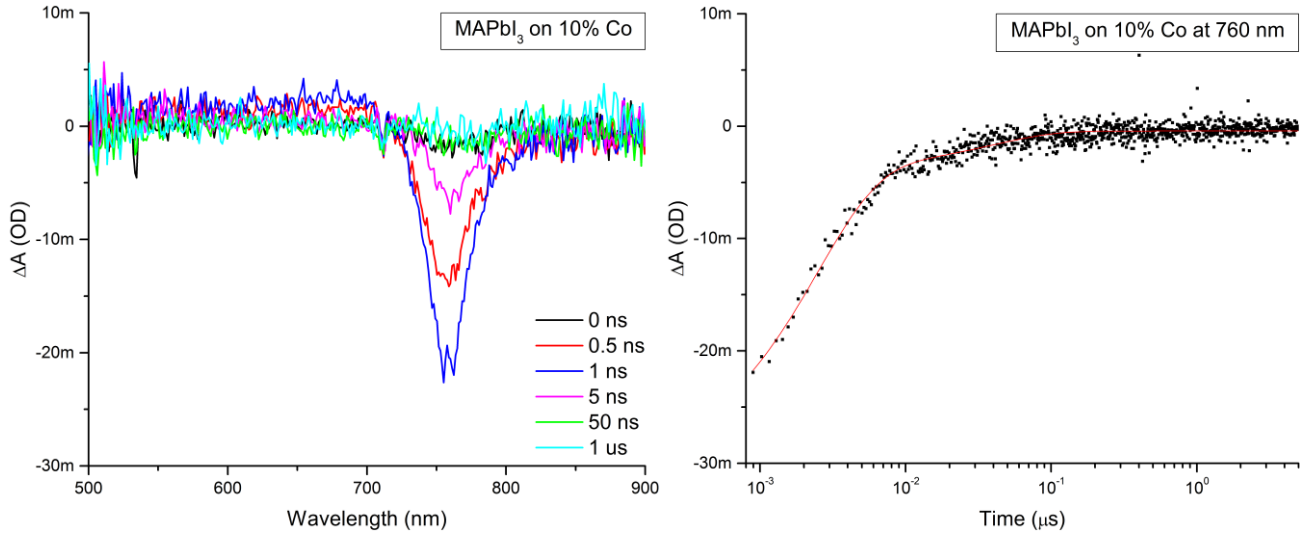

Figure 58 TAS spectral and kinetic data of $MAPbI_3$ on 10% Co at a pump fluence of ~80 µJ/cm². Left) TAS spectra at different probe delay times. Right) Kinetic profile fitted with a double exponential function (red line) of the TAS spectra on the left at 760 nm

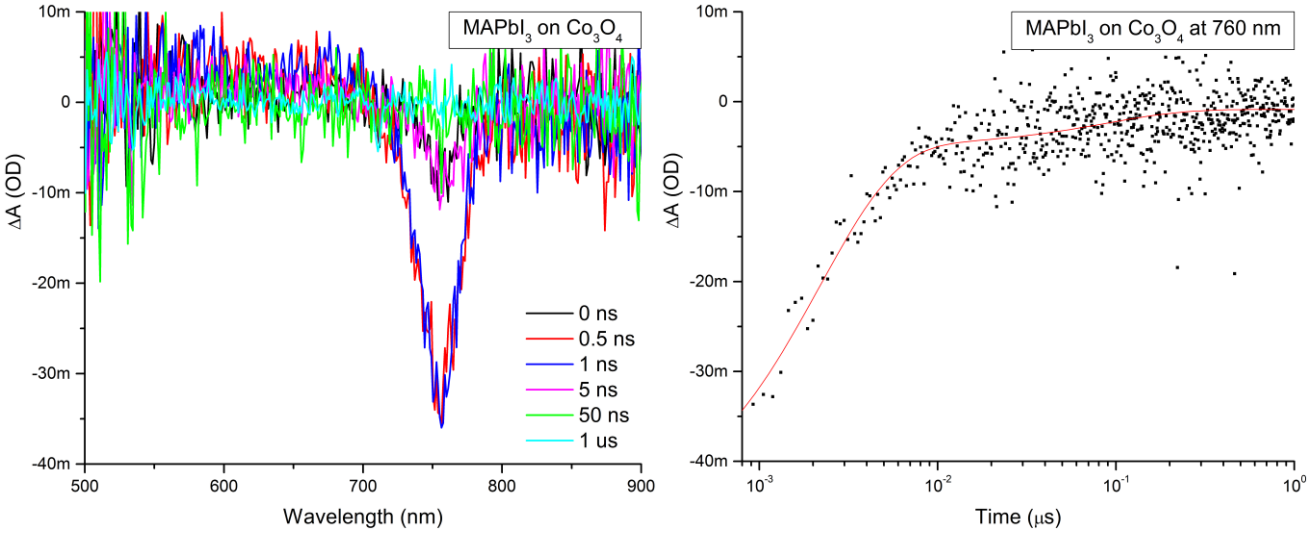

Figure 59 TAS spectral and kinetic data of $MAPbI_3$ on Co_3O_4 at a pump fluence of ~80 µJ/cm^2. Left) TAS spectra at different probe delay times. Right) Kinetic profile fitted with a double exponential function (red line) of the TAS spectra on the left at 760 nm

References

[1] H. N. Dinh, *Photoelectrochemical Water Splitting Standards , Experimental Methods , and Protocols*. .

[2] R. van de Krol and M. Grätzel, *Photoelectro - chemical Hydrogen Production*. 2012.

[3] L. Vayssieres, *On Solar Hydrogen & Nanotechnology*. Chichester, UK: John Wiley & Sons, Ltd, 2010.

[4] J. R. S. Brownson, *Solar Energy Conversion Systems*. Elsevier Inc., 2013.

[5] J. Nelson, *The Physics of Solar Cells*. Imperial College Press, 2003.

[6] X. Wang, *High-Efficiency Solar Cells*, vol. 190. Cham: Springer International Publishing, 2014.

[7] V. Fthenakis, "Sustainability of photovoltaics: The case for thin-film solar cells," *Renew. Sustain. Energy Rev.*, vol. 13, no. 9, pp. 2746–2750, Dec. 2009.

[8] H.-S. Kim, S. H. Im, and N.-G. Park, "Organolead Halide Perovskite: New Horizons in Solar Cell Research," *J. Phys. Chem. C*, vol. 118, no. 11, pp. 5615–5625, Mar. 2014.

[9] P. Gao, M. Grätzel, and M. K. Nazeeruddin, "Organohalide lead perovskites for photovoltaic applications," *Energy Environ. Sci.*, vol. 7, no. 8, pp. 2448–2463, 2014.

[10] W. S. Yang, J. H. Noh, N. J. Jeon, Y. C. Kim, S. Ryu, J. Seo, and S. I. Seok, "High-performance photovoltaic perovskite layers fabricated through intramolecular exchange," *Science (80-.).*, vol. 348, no. 6240, pp. 1234–1237, Jun. 2015.

[11] W. E. I. Sha, X. Ren, L. Chen, and W. C. H. Choy, "The efficiency limit of CH3NH3PbI3 perovskite solar cells," *Appl. Phys. Lett.*, vol. 106, no. 22, p. 221104, Jun. 2015.

[12] J. T.-W. Wang, J. M. Ball, E. M. Barea, A. Abate, J. A. Alexander-Webber, J. Huang, M. Saliba, I. Mora-Sero, J. Bisquert, H. J. Snaith, and R. J. Nicholas, "Low-temperature processed electron collection layers of graphene/TiO2 nanocomposites in thin film perovskite solar cells.," *Nano Lett.*, vol. 14, no. 2, pp. 724–30, Feb. 2014.

[13] J. M. Ball, M. M. Lee, A. Hey, and H. J. Snaith, "Low-temperature processed meso-superstructured to thin-film perovskite solar cells," *Energy Environ. Sci.*, vol. 6, no. 6, p. 1739, 2013.

[14] P. Docampo, J. M. Ball, M. Darwich, G. E. Eperon, and H. J. Snaith, "Efficient organometal trihalide perovskite planar-heterojunction solar cells on flexible polymer substrates.," *Nat. Commun.*, vol. 4, p. 2761, 2013.

[15] P. T. Landsberg, *Practical Handbook of Photovoltaics*. Elsevier, 2012.

[16] A. M. Bagher, "Comparison of organic solar cells and inorganic solar cells 2 . How Do Organic Solar Cells Work," *Int. J. Renew. Sustain. Energy*, vol. 3, no. 3, pp. 53–58, 2014.

[17] B. Michl, J. Benick, A. Richter, M. Bivour, J. Yong, R. Steeman, M. C. Schubert, and S. W. Glunz, "Excellent Average Diffusion Lengths of 600 µm of N-Type Multicrystalline Silicon Wafers After the Full Solar Cell Process Including Boron Diffusion," *Energy Procedia*, vol. 33, pp. 41–49, 2013.

[18] S. D. Stranks, G. E. Eperon, G. Grancini, C. Menelaou, M. J. P. Alcocer, T. Leijtens, L. M. Herz, A. Petrozza, and H. J. Snaith, "Electron-hole diffusion lengths exceeding 1 micrometer in an organometal trihalide perovskite absorber.," *Science*, vol. 342, no. 6156, pp. 341–4, Oct. 2013.

[19] S. Kazim, M. K. Nazeeruddin, M. Grätzel, and S. Ahmad, "Perovskite as light harvester: a game changer in photovoltaics.," *Angew. Chem. Int. Ed. Engl.*, vol. 53, no. 11, pp. 2812–24, Mar.

2014.

[20] T. Zdanowicz, T. Rodziewicz, and M. Zabkowska-Waclawek, “Theoretical analysis of the optimum energy band gap of semiconductors for fabrication of solar cells for applications in higher latitudes locations,” *Sol. Energy Mater. Sol. Cells*, vol. 87, no. 1–4, pp. 757–769, May 2005.

[21] Y. Kato, L. K. Ono, M. V. Lee, S. Wang, S. R. Raga, and Y. Qi, “Silver Iodide Formation in Methyl Ammonium Lead Iodide Perovskite Solar Cells with Silver Top Electrodes,” *Adv. Mater. Interfaces*, vol. 2, no. 13, p. n/a–n/a, Sep. 2015.

[22] J. Luo, J.-H. Im, M. T. Mayer, M. Schreier, M. K. Nazeeruddin, N.-G. Park, S. D. Tilley, H. J. Fan, and M. Gratzel, “Water photolysis at 12.3% efficiency via perovskite photovoltaics and Earth-abundant catalysts,” *Science (80-.).*, vol. 345, no. 6204, pp. 1593–1596, Sep. 2014.

[23] J. M. Frost, K. T. Butler, F. Brivio, C. H. Hendon, M. van Schilfgaarde, and A. Walsh, “Atomistic origins of high-performance in hybrid halide perovskite solar cells.,” *Nano Lett.*, vol. 14, no. 5, pp. 2584–90, May 2014.

[24] Y. Ogomi, A. Morita, S. Tsukamoto, T. Saitho, N. Fujikawa, Q. Shen, T. Toyoda, K. Yoshino, S. S. Pandey, T. Ma, and S. Hayase, “CH 3 NH 3 Sn x Pb (1– x) I 3 Perovskite Solar Cells Covering up to 1060 nm,” *J. Phys. Chem. Lett.*, vol. 5, no. 6, pp. 1004–1011, Mar. 2014.

[25] A. Kojima, K. Teshima, Y. Shirai, and T. Miyasaka, “Organometal halide perovskites as visible-light sensitizers for photovoltaic cells.,” *J. Am. Chem. Soc.*, vol. 131, no. 17, pp. 6050–1, May 2009.

[26] W. Li, J. Li, L. Wang, G. Niu, R. Gao, and Y. Qiu, “Post modification of perovskite sensitized solar cells by aluminum oxide for enhanced performance,” *J. Mater. Chem. A*, vol. 1, no. 38, p. 11735, 2013.

[27] H.-S. Kim, C.-R. Lee, J.-H. Im, K.-B. Lee, T. Moehl, A. Marchioro, S.-J. Moon, R. Humphry-Baker, J.-H. Yum, J. E. Moser, M. Grätzel, and N.-G. Park, “Lead iodide perovskite sensitized all-solid-state submicron thin film mesoscopic solar cell with efficiency exceeding 9%.,” *Sci. Rep.*, vol. 2, p. 591, Jan. 2012.

[28] J. M. Ball, M. M. Lee, A. Hey, and H. J. Snaith, “Low-temperature processed meso-superstructured to thin-film perovskite solar cells,” *Energy Environ. Sci.*, vol. 6, no. 6, p. 1739, 2013.

[29] H. Zhou, Q. Chen, G. Li, S. Luo, T. -b. Song, H.-S. Duan, Z. Hong, J. You, Y. Liu, and Y. Yang, “Interface engineering of highly efficient perovskite solar cells,” *Science (80-.).*, vol. 345, no. 6196, pp. 542–546, Jul. 2014.

[30] K. Mahmood, B. S. Swain, and A. Amassian, “16.1% Efficient Hysteresis-Free Mesostructured Perovskite Solar Cells Based on Synergistically Improved ZnO Nanorod Arrays,” *Adv. Energy Mater.*, p. n/a–n/a, 2015.

[31] H.-S. Ko, J.-W. Lee, and N.-G. Park, “15.76% efficiency perovskite solar cells prepared under high relative humidity: importance of PbI 2 morphology in two-step deposition of CH 3 NH 3 PbI 3,” *J. Mater. Chem. A*, vol. 3, no. 16, pp. 8808–8815, 2015.

[32] M. M. Lee, J. Teuscher, T. Miyasaka, T. N. Murakami, and H. J. Snaith, “Efficient hybrid solar cells based on meso-superstructured organometal halide perovskites.,” *Science*, vol. 338, no. 6107, pp. 643–7, Nov. 2012.

[33] D. Liu, M. K. Gangishetty, and T. L. Kelly, “Effect of CH 3 NH 3 PbI 3 thickness on device efficiency in planar heterojunction perovskite solar cells,” *J. Mater. Chem. A*, vol. 2, no. 46, pp. 19873–19881, Oct. 2014.

[34] J. H. Kim, P.-W. Liang, S. T. Williams, N. Cho, C.-C. Chueh, M. S. Glaz, D. S. Ginger, and A. K.-Y.

Jen, “High-Performance and Environmentally Stable Planar Heterojunction Perovskite Solar Cells Based on a Solution-Processed Copper-Doped Nickel Oxide Hole-Transporting Layer,” *Adv. Mater.*, vol. 27, no. 4, p. n/a–n/a, Nov. 2014.

[35] S. Bai, M. Cao, Y. Jin, X. Dai, X. Liang, Z. Ye, M. Li, J. Cheng, X. Xiao, Z. Wu, Z. Xia, B. Sun, E. Wang, Y. Mo, F. Gao, and F. Zhang, “Low-Temperature Combustion-Synthesized Nickel Oxide Thin Films as Hole-Transport Interlayers for Solution-Processed Optoelectronic Devices,” *Adv. Energy Mater.*, vol. 4, no. 6, p. n/a–n/a, Apr. 2014.

[36] H. Tian, B. Xu, H. Chen, E. M. J. Johansson, and G. Boschloo, “Solid-state perovskite-sensitized p-type mesoporous nickel oxide solar cells.,” *ChemSusChem*, vol. 7, no. 8, pp. 2150–3, Aug. 2014.

[37] F. Iacomi, G. Calin, C. Scarlat, M. Irimia, C. Doroftei, M. Dobromir, G. G. Rusu, N. Iftimie, and A. V. Sandu, “Functional properties of nickel cobalt oxide thin films,” *Thin Solid Films*, vol. 520, no. 1, pp. 651–655, Oct. 2011.

[38] B. Han, K. H. Choi, K. Park, W. S. Han, and W.-J. Lee, “Low-Temperature Atomic Layer Deposition of Cobalt Oxide Thin Films Using Dicobalt Hexacarbonyl tert-Butylacetylene and Ozone,” *Electrochem. Solid-State Lett.*, vol. 15, no. 2, pp. D14–D17, Jan. 2011.

[39] S. Wang, B. Zhang, C. Zhao, S. Li, M. Zhang, and L. Yan, “Valence control of cobalt oxide thin films by annealing atmosphere,” *Appl. Surf. Sci.*, vol. 257, no. 8, pp. 3358–3362, Feb. 2011.

[40] A. Gulino, P. Dapporto, P. Rossi, and I. Fragalà, “A Novel Self-generating Liquid MOCVD Precursor for Co 3 O 4 Thin Films,” *Chem. Mater.*, vol. 15, no. 20, pp. 3748–3752, Oct. 2003.

[41] R. Sharma, A. D. Acharya, S. Moghe, S. B. Shrivastava, M. Gangrade, T. Shripathi, and V. Ganesan, “Effect of cobalt doping on microstructural and optical properties of nickel oxide thin films,” *Mater. Sci. Semicond. Process.*, vol. 23, pp. 42–49, Jul. 2014.

[42] S. Liu, R. Liu, Y. Chen, S. Ho, J. H. Kim, and F. So, “Nickel Oxide Hole Injection/Transport Layers for Efficient Solution-Processed Organic Light-Emitting Diodes,” *Chem. Mater.*, vol. 26, no. 15, pp. 4528–4534, Aug. 2014.

[43] B. T. Raut, S. G. Pawar, M. A. Chougule, S. Sen, and V. B. Patil, “New process for synthesis of nickel oxide thin films and their characterization,” *J. Alloys Compd.*, vol. 509, no. 37, pp. 9065–9070, Sep. 2011.

[44] M. Jlassi, I. Sta, M. Hajji, and H. Ezzaouia, “Optical and electrical properties of nickel oxide thin films synthesized by sol–gel spin coating,” *Mater. Sci. Semicond. Process.*, vol. 21, pp. 7–13, May 2014.

[45] J. . Garcia-Miquel, Q. Zhang, S. . Allen, A. Rougier, A. Blyr, H. . Davies, A. . Jones, T. . Leedham, P. . Williams, and S. . Impey, “Nickel oxide sol–gel films from nickel diacetate for electrochromic applications,” *Thin Solid Films*, vol. 424, no. 2, pp. 165–170, Jan. 2003.

[46] K.-C. Wang, J.-Y. Jeng, P.-S. Shen, Y.-C. Chang, E. W.-G. Diau, C.-H. Tsai, T.-Y. Chao, H.-C. Hsu, P.-Y. Lin, P. Chen, T.-F. Guo, and T.-C. Wen, “p-type Mesoscopic nickel oxide/organometallic perovskite heterojunction solar cells.,” *Sci. Rep.*, vol. 4, p. 4756, Jan. 2014.

[47] X. Wang, Q. Peng, W. Zhu, and G. Lei, “High performance of inverted polymer solar cells with cobalt oxide as hole-transporting layer,” *Semicond. Sci. Technol.*, vol. 30, no. 5, p. 55001, 2015.

[48] K. J. Kim and Y. R. Park, “Optical investigation of charge-transfer transitions in spinel Co3O4,” *Solid State Commun.*, vol. 127, no. 1, pp. 25–28, Jun. 2003.

[49] A. Walsh, K.-S. Ahn, S. Shet, M. N. Huda, T. G. Deutsch, H. Wang, J. A. Turner, S.-H. Wei, Y. Yan, and M. M. Al-Jassim, “Ternary cobalt spinel oxides for solar driven hydrogen production: Theory and experiment,” *Energy Environ. Sci.*, vol. 2, p. 774, 2009.

[50] J. Burschka, N. Pellet, S.-J. Moon, R. Humphry-Baker, P. Gao, M. K. Nazeeruddin, and M. Grätzel, “Sequential deposition as a route to high-performance perovskite-sensitized solar cells,” *Nature*, vol. 499, no. 7458, pp. 316–319, Jul. 2013.

[51] Q. Chen, H. Zhou, Z. Hong, S. Luo, H.-S. Duan, H.-H. Wang, Y. Liu, G. Li, and Y. Yang, “Planar heterojunction perovskite solar cells via vapor-assisted solution process.,” *J. Am. Chem. Soc.*, vol. 136, no. 2, pp. 622–5, Jan. 2014.

[52] W. S. Yang, J. H. Noh, N. J. Jeon, Y. C. Kim, S. Ryu, J. Seo, and S. I. Seok, “High-performance photovoltaic perovskite layers fabricated through intramolecular exchange,” *Science (80-.).*, 2015.

[53] A. Mei, X. Li, L. Liu, Z. Ku, T. Liu, Y. Rong, M. Xu, M. Hu, J. Chen, Y. Yang, M. Gratzel, and H. Han, “A hole-conductor-free, fully printable mesoscopic perovskite solar cell with high stability,” *Science (80-.).*, vol. 345, no. 6194, pp. 295–298, Jul. 2014.

[54] S. Roland, S. Neubert, S. Albrecht, B. Stannowski, M. Seger, A. Facchetti, R. Schlatmann, B. Rech, and D. Neher, “Hybrid Organic/Inorganic Thin-Film Multijunction Solar Cells Exceeding 11% Power Conversion Efficiency,” *Adv. Mater.*, vol. 27, no. 7, pp. 1262–1267, Feb. 2015.

[55] J. P. Mailoa, C. D. Bailie, E. C. Johlin, E. T. Hoke, A. J. Akey, W. H. Nguyen, M. D. McGehee, and T. Buonassisi, “A 2-terminal perovskite/silicon multijunction solar cell enabled by a silicon tunnel junction,” *Appl. Phys. Lett.*, vol. 106, no. 12, p. 121105, Mar. 2015.

[56] M. M. May, H.-J. Lewerenz, D. Lackner, F. Dimroth, and T. Hannappel, “Efficient direct solar-to-hydrogen conversion by in situ interface transformation of a tandem structure,” *Nat. Commun.*, vol. 6, p. 8286, Sep. 2015.

[57] P. Luo, Z. Liu, W. Xia, C. Yuan, J. Cheng, and Y. Lu, “Uniform, Stable and Efficient Planar-Heterojunction Perovskite Solar Cells by a Facile Low-Pressure Chemical Vapor Deposition under Fully Open-Air Condition.,” *ACS Appl. Mater. Interfaces*, vol. 7, no. 4, pp. 2708–2714, Jan. 2015.

[58] P. J. Cousins, D. D. Smith, H.-C. Luan, J. Manning, T. D. Dennis, A. Waldhauer, K. E. Wilson, G. Harley, and W. P. Mulligan, “Generation 3: Improved performance at lower cost,” in *2010 35th IEEE Photovoltaic Specialists Conference*, 2010, pp. 000275–000278.

[59] Y.-C. Chern, H.-R. Wu, Y.-C. Chen, H.-W. Zan, H.-F. Meng, and S.-F. Horng, “Reliable solution processed planar perovskite hybrid solar cells with large-area uniformity by chloroform soaking and spin rinsing induced surface precipitation,” *AIP Adv.*, vol. 5, no. 8, p. 087125, Aug. 2015.

[60] D. P. Birnie, “Spin Coating: Art and Science,” in *Chemical Solution Deposition of Functional Oxide Thin Films*, Vienna: Springer Vienna, 2013, pp. 263–274.

[61] S. Lv, S. Pang, Y. Zhou, N. P. Padture, H. Hu, L. Wang, X. Zhou, H. Zhu, L. Zhang, C. Huang, and G. Cui, “One-step, solution-processed formamidinium lead trihalide (FAPbI(3-x)Cl(x)) for mesoscopic perovskite-polymer solar cells.,” *Phys. Chem. Chem. Phys.*, vol. 16, no. 36, pp. 19206–11, Sep. 2014.

[62] Y. Yamada, M. Endo, A. Wakamiya, and Y. Kanemitsu, “Spontaneous Defect Annihilation in CH 3 NH 3 PbI 3 Thin Films at Room Temperature Revealed by Time-Resolved Photoluminescence Spectroscopy,” *J. Phys. Chem. Lett.*, vol. 6, no. 3, pp. 482–486, Jan. 2015.

[63] L. Zheng, Y. Ma, S. Chu, S. Wang, B. Qu, L. Xiao, Z. Chen, Q. Gong, Z. Wu, and X. Hou, “Improved light absorption and charge transport for perovskite solar cells with rough interfaces by sequential deposition.,” *Nanoscale*, vol. 6, no. 14, pp. 8171–6, Jul. 2014.

[64] Y. Zhao and K. Zhu, “CH 3 NH 3 Cl-Assisted One-Step Solution Growth of CH 3 NH 3 PbI 3 : Structure, Charge-Carrier Dynamics, and Photovoltaic Properties of Perovskite Solar Cells,” *J.*

Phys. Chem. C, vol. 118, no. 18, pp. 9412–9418, May 2014.

[65] Z. Xiao, Q. Dong, C. Bi, Y. Shao, Y. Yuan, and J. Huang, "Solvent Annealing of Perovskite-Induced Crystal Growth for Photovoltaic-Device Efficiency Enhancement," *Adv. Mater.*, p. n/a–n/a, 2014.

[66] J.-H. Im, I.-H. Jang, N. Pellet, M. Grätzel, and N.-G. Park, "Growth of CH3NH3PbI3 cuboids with controlled size for high-efficiency perovskite solar cells.," *Nat. Nanotechnol.*, Aug. 2014.

[67] Y. Zhou, M. Yang, A. L. Vasiliev, H. F. Garces, Y. Zhao, D. Wang, S. Pang, K. Zhu, and N. P. Padture, "Growth Control of Compact CH 3 NH 3 PbI 3 Thin Films via Enhanced Solid- State Precursor Reaction for Efficient Planar Perovskite Solar Cells," *J. Mater. Chem. A*, 2015.

[68] Z. Xiao, C. Bi, Y. Shao, Q. Dong, Q. Wang, Y. Yuan, C. Wang, Y. Gao, and J. Huang, "Efficient{,} high yield perovskite photovoltaic devices grown by interdiffusion of solution-processed precursor stacking layers," *Energy Environ. Sci.*, vol. 7, no. 8, pp. 2619–2623, 2014.

[69] B. Fultz and J. Howe, *Transmission Electron Microscopy and Diffractometry of Materials*. Berlin, Heidelberg: Springer Berlin Heidelberg, 2013.

[70] FEI company, "Nova 600 Nanolab," 2003. [Online]. Available: http://www.nanolab.ucla.edu/pdf/Nova600spec.pdf. [Accessed: 11-Jan-2016].

[71] K. Shimizu and T. Mitani, *New Horizons of Applied Scanning Electron Microscopy*, vol. 45. Berlin, Heidelberg: Springer Berlin Heidelberg, 2010.

[72] C. Kumar, *UV-VIS and Photoluminescence Spectroscopy for Nanomaterials Characterization*. Berlin, Heidelberg: Springer Berlin Heidelberg, 2013.

[73] A. D. Sheikh, A. Bera, M. A. Haque, R. B. Rakhi, S. Del Gobbo, H. N. Alshareef, and T. Wu, "Atmospheric effects on the photovoltaic performance of hybrid perovskite solar cells," *Sol. Energy Mater. Sol. Cells*, vol. 137, pp. 6–14, Jun. 2015.

[74] O. F. Mohammed, "Transient Absorption Spectroscopy." [Online]. Available: https://sperc.kaust.edu.sa/Pages/Femtosecond-Transient-Absorption-Spectroscopy.aspx.

[75] R. Berera, R. van Grondelle, and J. T. M. Kennis, "Ultrafast transient absorption spectroscopy: principles and application to photosynthetic systems," *Photosynth. Res.*, vol. 101, no. 2–3, pp. 105–118, Sep. 2009.

[76] J. A. Christians, P. A. Miranda Herrera, and P. V Kamat, "Transformation of the Excited State and Photovoltaic Efficiency of CH3NH3PbI3 Perovskite upon Controlled Exposure to Humidified Air.," *J. Am. Chem. Soc.*, vol. 137, no. 4, pp. 1530–1538, Jan. 2015.

[77] K. Ocakoglu, F. Yakuphanoglu, J. R. Durrant, and S. Icli, "The effect of temperature on the charge transport and transient absorption properties of K27 sensitized DSSC," *Sol. Energy Mater. Sol. Cells*, vol. 92, no. 9, pp. 1047–1053, 2008.

[78] R. S. Sanchez, V. Gonzalez-Pedro, J.-W. Lee, N.-G. Park, Y. S. Kang, I. Mora-Sero, and J. Bisquert, "Slow Dynamic Processes in Lead Halide Perovskite Solar Cells. Characteristic Times and Hysteresis," *J. Phys. Chem. Lett.*, vol. 5, no. 13, pp. 2357–2363, Jul. 2014.

[79] Filmetrics, "Reflectance Calculator." [Online]. Available: http://www.filmetrics.com/reflectance-calculator. [Accessed: 28-Oct-2015].

[80] J. D. Desai, S.-K. Min, K.-D. Jung, and O.-S. Joo, "Spray pyrolytic synthesis of large area NiOx thin films from aqueous nickel acetate solutions," *Appl. Surf. Sci.*, vol. 253, no. 4, pp. 1781–1786, Dec. 2006.

[81] G. Boschloo and A. Hagfeldt, "Spectroelectrochemistry of Nanostructured NiO," *J. Phys. Chem. B*, vol. 105, no. 15, pp. 3039–3044, Apr. 2001.

[82] A. D. Acharya, S. Moghe, R. Panda, S. B. Shrivastava, M. Gangrade, T. Shripathi, D. M. Phase,

and V. Ganesan, “Growth and characterization of nano-structured Sn doped ZnO,” *J. Mol. Struct.*, vol. 1022, pp. 8–15, Aug. 2012.

[83] X. Zhu, J. Wang, D. Nguyen, J. Thomas, R. A. Norwood, and N. Peyghambarian, “Linear and nonlinear optical properties of Co_3O_4 nanoparticle-doped polyvinyl-alcohol thin films,” *Opt. Mater. Express*, vol. 2, no. 1, p. 103, Jan. 2012.

[84] J. S. Manser and P. V. Kamat, “Band filling with free charge carriers in organometal halide perovskites,” *Nat. Photonics*, vol. 8, no. 9, pp. 737–743, Aug. 2014.

[85] Y. P. Rakovich, J. F. Donegan, M. I. Vasilevskiy, and A. L. Rogach, “Anti-Stokes cooling in semiconductor nanocrystal quantum dots: A feasibility study,” *Phys. status solidi*, vol. 206, no. 11, pp. 2497–2509, Nov. 2009.

[86] S. Ryu, J. H. Noh, N. J. Jeon, Y. Chan Kim, W. S. Yang, J. Seo, and S. Il Seok, “Voltage output of efficient perovskite solar cells with high open-circuit voltage and fill factor,” *Energy Environ. Sci.*, vol. 7, no. 8, pp. 2614–2618, 2014.

[87] K. Yan, Z. Wei, J. Li, H. Chen, Y. Yi, X. Zheng, X. Long, Z. Wang, J. Wang, J. Xu, and S. Yang, “High-Performance Graphene-Based Hole Conductor-Free Perovskite Solar Cells: Schottky Junction Enhanced Hole Extraction and Electron Blocking,” *Small*, p. n/a–n/a, Jan. 2015.

[88] C. Mitterer, O. Heuzè, and V.-H. Derflinger, “Substrate and coating damage by arcing during sputtering,” *Surf. Coatings Technol.*, vol. 89, no. 3, pp. 233–238, Mar. 1997.

[89] M. Diskus, O. Nilsen, and H. Fjellvåg, “Thin Films of Cobalt Oxide Deposited on High Aspect Ratio Supports by Atomic Layer Deposition,” *Chem. Vap. Depos.*, vol. 17, no. 4–6, pp. 135–140, Jun. 2011.

[90] C. C. Mercado, A. Zakutayev, K. Zhu, C. J. Flynn, J. F. Cahoon, and A. J. Nozik, “Sensitized Zinc–Cobalt–Oxide Spinel p-Type Photoelectrode,” *J. Phys. Chem. C*, vol. 118, no. 44, pp. 25340–25349, Nov. 2014.